

HIGH  $p_T$   $\pi^0$  AND  $\eta$  PRODUCTION BY 300  
GEV/C  $\pi^\pm$  AND  $p$  BEAMS ON A  ${}^7\text{Li}$   
TARGET

by  
Qifeng Shen

Duke University  
Physics Department  
1992



Copyright © by  
Qifeng Shen  
1992



**ABSTRACT**

(Physics-Particle)

**HIGH  $p_T$   $\pi^0$  AND  $\eta$  PRODUCTION BY  
300 GEV/C  $\pi^\pm$  AND  $p$  BEAMS ON A  ${}^7\text{Li}$   
TARGET**

by

Qifeng Shen

Department of Physics  
Duke University

Date: June 11, 1992

Approved:

Lloyd R. Fortney  
Lloyd R. Fortney, Supervisor

Laurence

John E. Thomas

John E. Thomas

John E. Thomas

An abstract of a dissertation submitted in partial  
fulfillment of the requirements for the degree  
of doctor of philosophy in the Department of  
Physics in the Graduate School of  
Duke University



# Abstract

The inclusive cross sections of high  $p_T$   $\pi^0$  and  $\eta$  production were measured in 300 GeV  $\pi^\pm Li$  and  $p Li$  interactions, by Fermilab experiment 705. The data covered the  $p_T$  range from 3.5 GeV/c to 7.0 GeV/c, and the  $x_F$  range from -0.25 to 0.35.

The inclusive  $\pi^0$  production cross section falls off with increasing  $p_T$ , following a power law that is in good agreement with the scaling violation behavior observed by earlier experiments. The  $\pi^0$  cross sections in  $\pi^+ Li$  and  $\pi^- Li$  are equal within statistical errors, and in agreement with theoretical prediction based on the isospin invariance. The  $\pi^0$  cross section ratio of  $\sigma(\pi^+ + Li \rightarrow \pi^0 + X)/\sigma(p + Li \rightarrow \pi^0 + X)$  increases with increasing  $p_T$  as expected from the parton model.

The  $\eta$  to  $\pi^0$  production ratios,  $\sigma(\pi^\pm, p + Li \rightarrow \eta + X)/\sigma(\pi^\pm, p + Li \rightarrow \pi^0 + X)$ , were also measured for the three different types of beams. Those ratios are  $0.471 \pm 0.031$ ,  $0.457 \pm 0.057$ , and  $0.562 \pm 0.074$  for  $\pi^-$ ,  $\pi^+$ , and proton beams, respectively.



# Acknowledgements

It has been a pleasant experience to work with my thesis adviser, Lloyd R. Fortney. He was always there to answer questions, and was ready for discussions (sometimes heated). He cared very much about his students. It was a great learning process working under his guidance.

I would like to thank the collaborators of Fermilab E705. Chengrui Wang put a great deal of effort in sending me to Fermilab to work there. Thorton Murphy and Wilox Yang provided much needed help when I first arrived at the Lab. Steve Delchamps, Alberto Marchionni, Marzia Rosati, and George Zioulas deserve special mentioning for their help and friendship.

It has been fun to be around my fellow graduate students at Duke. My gratitude goes to Tom Carter, Jay Cook, Yutao Feng, Mark Godwin, Susi Hauger, Xiaoyu Li, Cal Loomis, Xi Qin, Rick Tesarek, Tim Turkington, Ying Wu, and Hongzhi Zhao. The staff and faculty members of the HEP group, in particular, Pat Hoyt, made my stay at Duke a memorable one.

I would like take this opportunity to thank my parents and grandmother for their education, love, and encouragement. Special thanks go to my wife, Xiaohong Shi, for her understanding, support, and patience.



# Contents

<b>Abstract</b>	<b>iii</b>
<b>Acknowledgements</b>	<b>iv</b>
<b>Contents</b>	<b>v</b>
<b>List of Figures</b>	<b>viii</b>
<b>List of Tables</b>	<b>x</b>
<b>1 Introduction</b>	<b>1</b>
1.1 Quark Model . . . . .	2
1.2 Parton Distribution Function and QCD . . . . .	5
1.3 Direct Photon . . . . .	9
1.4 $\pi^0$ and $\eta$ Production . . . . .	12
<b>2 Experiment Setup</b>	<b>14</b>
2.1 Beam . . . . .	17
2.1.1 The Secondary Beam to the Experiment . . . . .	17
2.1.2 Beam Stations . . . . .	18
2.1.3 Cerenkov Counters . . . . .	20
2.1.4 T1 Counter . . . . .	21
2.1.5 Veto Walls . . . . .	21
2.1.6 Beam Logic . . . . .	22
2.2 Target . . . . .	22
2.3 Interaction Trigger . . . . .	23
2.3.1 Charged Particle Hodoscope . . . . .	23
2.3.2 The Interaction Trigger . . . . .	24
2.4 Analysis Magnet . . . . .	24
2.5 Wire Chamber System . . . . .	25
2.6 Electromagnetic Detector . . . . .	27
2.7 Muon Counters . . . . .	27

<b>3</b>	<b>The Electromagnetic Detector</b>	<b>29</b>
3.1	Scintillation Glass and Lead Glass . . . . .	32
3.2	Active Converter . . . . .	33
3.3	Gas Tube Hodoscope . . . . .	35
3.4	Lead Gas Calorimeter . . . . .	37
3.5	Main Array . . . . .	38
3.6	Instrumentation . . . . .	39
	3.6.1 LGC and GTH . . . . .	40
	3.6.2 The Charge Amplifier and ADC Card . . . . .	40
3.7	The Cluster Finder . . . . .	43
<b>4</b>	<b>Calibration of the Calorimeter</b>	<b>47</b>
4.1	Electron Beams . . . . .	47
4.2	Setting the Gains . . . . .	48
4.3	On-line Calibration Sequence . . . . .	49
4.4	The Off-line Procedure . . . . .	50
	4.4.1 Data Reduction . . . . .	51
	4.4.2 GTH and LGC Gains . . . . .	52
	4.4.3 Glass Gains . . . . .	56
4.5	Energy Dependence . . . . .	62
4.6	Energy Resolutions . . . . .	64
4.7	Glass Gain Monitoring and Correction . . . . .	66
<b>5</b>	<b>The Shower Position Measurement</b>	<b>69</b>
5.1	The Deconvolution Method . . . . .	71
5.2	Shower Widths . . . . .	73
5.3	The Position and Energy Determination Using Deconvolution	74
5.4	Comparison between the Deconvolution and the Sum-over-	
	tubes Methods . . . . .	79
5.5	Position Resolution . . . . .	81
5.6	Separation of Showers . . . . .	85
<b>6</b>	<b>Electromagnetic Shower Reconstruction</b>	<b>87</b>
6.1	Decoding . . . . .	88
	6.1.1 Main Array and Active Converter . . . . .	88
	6.1.2 The LGC and the GTH . . . . .	89
6.2	Shower Reconstruction in the Main Array . . . . .	92
	6.2.1 Pattern Recognition and Initial Sharing . . . . .	92
	6.2.2 Shower Tables . . . . .	93
	6.2.3 Position and Energy Determination in Main Array . . . . .	97
6.3	Shower Reconstruction in Hodoscopes . . . . .	100
	6.3.1 The Initial Search . . . . .	100
	6.3.2 Adding New Showers . . . . .	103
6.4	Further Iterations . . . . .	105

<b>7</b>	<b>Data Analysis</b>	<b>108</b>
7.1	Data Reduction . . . . .	108
7.2	Event Selection . . . . .	110
7.3	$\gamma$ - $\gamma$ Invariant Mass . . . . .	116
<b>8</b>	<b>Normalization</b>	<b>122</b>
8.1	Beam Counting . . . . .	122
8.2	Trigger Efficiency . . . . .	126
8.2.1	Physics Triggers . . . . .	126
8.2.2	Cluster Finder Trigger Efficiency . . . . .	127
8.2.3	$\pi^0$ and $\eta$ Trigger Efficiency . . . . .	131
8.3	Timing Cut . . . . .	134
8.4	Monte Carlo Simulation . . . . .	136
8.4.1	Geometric Acceptance . . . . .	136
8.4.2	Reconstruction Efficiency . . . . .	138
<b>9</b>	<b>Results and Conclusions</b>	<b>144</b>
9.1	formulation . . . . .	144
9.2	$\pi^0$ Cross Section . . . . .	145
9.2.1	$\pi^+$ and $\pi^-$ Beams . . . . .	148
9.2.2	Proton Beam . . . . .	155
9.2.3	Systematic Errors . . . . .	159
9.3	$\eta$ Cross Sections . . . . .	160
9.4	Comparison with Other Experiments . . . . .	163
9.5	Conclusions . . . . .	170
	<b>References</b>	<b>171</b>
	<b>Biography</b>	<b>175</b>



# List of Figures

1.1	Pseudoscalar meson octet and singlet. . . . .	4
1.2	Feynman diagrams . . . . .	8
2.1	Proton-west secondary beam line. . . . .	15
2.2	E705 Spectrometer . . . . .	16
2.3	Beam definition logic. . . . .	20
3.1	The electromagnetic detector. . . . .	30
3.2	Front view of the calorimeter. . . . .	31
3.3	Active converter light attenuation. . . . .	34
3.4	Top view of a portion of the hodoscopes. . . . .	36
3.5	Schematic of the charge card. . . . .	41
3.6	The Cluster Finder trigger logic. . . . .	44
3.7	Cluster energy to $p_T$ conversion. . . . .	45
4.1	GTH $x$ -east ADC Profile . . . . .	53
4.2	ADC distribution of the GTH $x$ -east view . . . . .	55
4.3	A typical $x$ -position dependence of the LGC $y$ -view energy . . . . .	56
4.4	Longitudinal light attenuation . . . . .	58
4.5	Reconstructed calibration electron energies . . . . .	63
4.6	Energy resolutions . . . . .	65
4.7	Main array block gain changes . . . . .	67
5.1	Hodoscope shower shapes . . . . .	75
5.2	Hodoscope shower width as function of energy . . . . .	76
5.3	Correlation between deconvolution and sum-over-tubes . . . . .	80
5.4	$x - y$ energy match-up in hodoscopes . . . . .	81
5.5	Position residuals . . . . .	83
5.6	Position resolutions . . . . .	84
5.7	Hodoscope shower separation efficiency . . . . .	86
6.1	Numbering convention for the nine-block cluster pattern. . . . .	94
6.2	Examples of the three-block set combinations. . . . .	95
6.3	Correlation between the GTH ADC counts and the active converter energy . . . . .	105

7.1	Interaction vertex distributions . . . . .	111
7.2	Active plane energy for 60 GeV charged pion and electron. . . . .	115
7.3	$\gamma$ - $\gamma$ Invariant Mass. . . . .	117
7.4	Two-photon Energy Asymmetry. . . . .	121
8.1	Pion scaler sagging . . . . .	124
8.2	Photon trigger efficiency. . . . .	129
8.3	Correlation between $p_T$ of $\pi^0$ and $p_T$ of cluster . . . . .	131
8.4	Time distributions . . . . .	135
8.5	Comparison of real data and Monte Carlo events. . . . .	142
9.1	Invariant cross section $\sigma(\pi^- + Li \rightarrow \pi^0 + X)$ vs $p_T$ . . . . .	149
9.2	Invariant cross section $\sigma(\pi^+ + Li \rightarrow \pi^0 + X)$ vs $p_T$ . . . . .	150
9.3	Invariant cross section $\sigma(\pi^\pm + Li \rightarrow \pi^0 + X)$ vs $p_T$ . . . . .	151
9.4	Ratio of $\pi^0$ invariant cross sections by $\pi^+$ and $\pi^-$ beams. . . . .	152
9.5	Invariant cross section $\sigma(\pi^- + Li \rightarrow \pi^0 + X)$ vs $x_F$ . . . . .	153
9.6	Invariant cross section $\sigma(\pi^+ + Li \rightarrow \pi^0 + X)$ vs $x_F$ . . . . .	154
9.7	Invariant cross section $\sigma(p + Li \rightarrow \pi^0 + X)$ vs $p_T$ . . . . .	156
9.8	Ratio of $\pi^0$ invariant cross sections by $\pi^+$ and $p$ beams. . . . .	157
9.9	Invariant cross section $\sigma(p + Li \rightarrow \pi^0 + X)$ vs $x_F$ . . . . .	158
9.10	Ratio of $\eta$ and $\pi^0$ invariant cross sections by $\pi^+$ and $\pi^-$ beams. . . . .	161
9.11	Invariant cross section $\sigma(\pi^- + Li \rightarrow \pi^0 + X)$ vs $p_T$ . . . . .	164
9.12	Invariant cross section $\sigma(\pi^+ + Li \rightarrow \pi^0 + X)$ vs $p_T$ . . . . .	165
9.13	Invariant cross section $\sigma(p + Li \rightarrow \pi^0 + X)$ vs $p_T$ . . . . .	166
9.14	Invariant cross section $\sigma(\pi^- + Li \rightarrow \pi^0 + X)$ vs $x_T$ . . . . .	167
9.15	Invariant cross section $\sigma(\pi^+ + Li \rightarrow \pi^0 + X)$ vs $x_T$ . . . . .	168
9.16	Invariant cross section $\sigma(p + Li \rightarrow \pi^0 + X)$ vs $x_T$ . . . . .	169

# List of Tables

1.1	Quantum Numbers of the Original Quarks . . . . .	3
1.2	Parameters of Three Recent Fixed Target Experiments . . .	13
2.1	Chamber Specifications, Resolutions, and Their Z-locations .	26
3.1	The Characteristics of SCG1-C Glass and SF5 Glass . . . . .	32
4.1	Software Thresholds of the Four Hodoscope Planes . . . . .	52
4.2	Energy Resolutions in Various Regions . . . . .	64
4.3	The $a, b$ Parameters of Various Regions . . . . .	66
5.1	Widths of Symmetric Showers (cm) . . . . .	73
5.2	Parameters of the Position Resolutions . . . . .	82
6.1	Percentages of Calibration Events with LGC ADC Overflows	91
7.1	Hadron Rejection Rate and Electron Loss (%) . . . . .	116
7.2	$\pi^0$ and $\eta$ Mass and Width (in MeV). . . . .	118
8.1	Number of Beam Particles . . . . .	125
8.2	Percentage of Various Triggers . . . . .	127
8.3	Sub-eras of Different Photon Trigger Conditions. . . . .	128
8.4	Thresholds and Pre-scale Factors for the $P_T$ Triggers. . . . .	130
8.5	$\pi^0$ Trigger Efficiency. . . . .	133
8.6	$\eta$ Trigger Efficiency. . . . .	133
8.7	Event Loss Resulted from the Timing Cut (%). . . . .	134
8.8	$\pi^0$ Geometric Acceptance (%) . . . . .	137
8.9	$\eta$ Geometric Acceptance (%) . . . . .	138
8.10	$\pi^0$ Reconstruction Efficiency (%) . . . . .	141
8.11	$\eta$ Reconstruction Efficiency (%) . . . . .	141
9.1	Inclusive Cross Section of $\pi^- + Li \rightarrow \pi^0 + X$ . . . . .	146
9.2	Inclusive Cross Section of $\pi^+ + Li \rightarrow \pi^0 + X$ . . . . .	146
9.3	Inclusive Cross Section of $p + Li \rightarrow \pi^0 + X$ . . . . .	147
9.4	Parameters of the Phenomenological Fit. . . . .	147

LIST OF TABLES

xi

9.5  $\eta$  Cross Section. . . . . 162

# Chapter 1

## Introduction

Early this century (up to 1930), it seemed that all the elements needed to build the universe were found. Those particles were positively charged protons and electrically neutral neutrons in the nucleus, negatively charged electrons orbiting the nucleus, and photons mediating the interactions between the positively charged nucleus and the electron. In addition, there were electrically neutral massless neutrinos found in neutron decays. The various combinations of those particles could form different materials found up to that time. But there were still some unanswered questions. For example, since protons are positively charged, there must be another strong nuclear force to overcome the repulsive Coulomb interaction among the protons to keep them inside the small volume of the nucleus. Another example is the anomalous magnetic moments of proton and neutron being  $2.6\mu_N$  and  $-1.9\mu_N$ , instead of  $1.0\mu_N$  and  $0.0\mu_N$  as expected from their electric charges.

In 1935, Yukawa postulated the existence of an integral-spin quantum (meson) which mediated interactions among nucleons (protons and neutrons)

in a distance on the order of  $10^{-13}$  cm, and held them together. The Yukawa particle was at first misidentified as the muon (found in 1937), but was later found in cosmic-ray experiments in 1947 and identified as pion. From then on, more and more particles have been found from both cosmic-ray and accelerator experiments. Those particles, except the photon, were divided into two groups — leptons and hadrons — based on whether they experience strong nuclear force. Electrons, and muons, and their associated neutrinos do not experience any strong interaction, thus, they are leptons. Hadrons were further classified as integral-spin mesons and half-integral-spin baryons. As the number of elementary particles increased, it became more likely that those particles could also be composite ones.

## 1.1 Quark Model

Based on the quantum numbers and symmetries of the hadrons found, Gell-Mann and Zweig postulated a quark model independently in 1964 [1]. In this model, there are three flavors of quarks, namely, up (u), down (d), and strange (s) quarks, forming a quark triplet which is a fundamental representation of an SU(3) group. Quarks are spin one-half fermions with fractional charges, and their quantum numbers ( baryon number  $B$ , spin  $J$ , isospin  $I$  and its third component  $I_3$ , strangeness  $S$ , and electric charge  $Q$ ) are listed in Table 1.1 [2]. Antiquarks have their signs of  $B$ ,  $I_3$ ,  $S$ , and  $Q$  reversed. The estimated masses of the quarks were [3, page 64]

$$m_u \approx m_d \approx 0.39\text{GeV}, \quad m_s \approx 0.51\text{GeV}.$$

Table 1.1: Quantum Numbers of the Original Quarks

Flavor	$B$	$J$	$I$	$I_3$	$S$	$Q$
$u$	1/3	1/2	1/2	+1/2	0	+2/3
$d$	1/3	1/2	1/2	-1/2	0	-1/3
$s$	1/3	1/2	0	0	-1	-1/3

Hadrons are composite particles made up of quarks. Baryons consist of three quarks ( $qqq$ ), and mesons are made of a quark-antiquark pair ( $q\bar{q}$ ). These hadrons are elements of multiplet representations of  $SU(3)$ . For example, when a quark triplet is combined (direct product) with an antiquark triplet with their spins pointing in opposite directions, they form a pseudoscalar meson octet and a meson singlet as depicted in Figure 1.1. The wavefunctions of the quark-antiquark pairs in the central row are

$$\pi^- = d\bar{u}; \quad \pi^0 = \frac{1}{\sqrt{2}}(d\bar{d} - u\bar{u}); \quad \pi^+ = u\bar{d}; \quad (1.1)$$

and

$$\eta_8 = \frac{1}{\sqrt{6}}(d\bar{d} + u\bar{u} - 2s\bar{s}); \quad \eta_0 = \frac{1}{\sqrt{3}}(d\bar{d} + u\bar{u} + s\bar{s}). \quad (1.2)$$

The pions are identified with the physical particles. And the observed particles  $\eta$  and  $\eta'$  are linear combinations of  $\eta_8$  and  $\eta_0$ . The mass of  $\pi^0$  is 135 MeV, and that of  $\eta$  is 549 MeV. The branching ratio of  $\pi^0$  decaying into two photons is 0.988, while that of  $\eta$  decaying into two photons is 0.389.

The initial quark model enjoyed its success in explaining hadron spectroscopy and in predicting hadron's static electromagnetic properties. For example, it predicts the ratio of proton ( $uud$ ) and neutron ( $udd$ ) magnetic

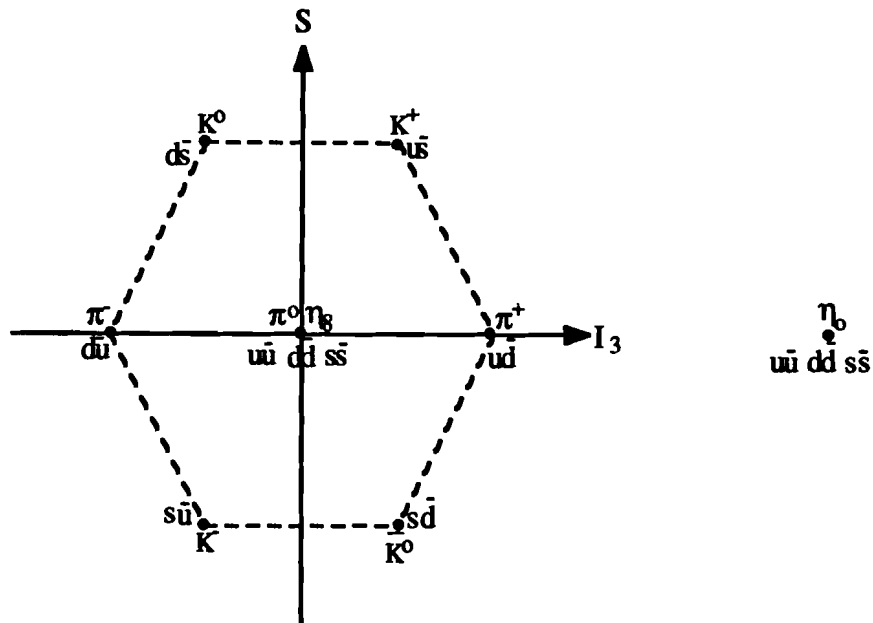


Figure 1.1: Pseudoscalar meson octet and singlet.

moments to be  $-2/3$ , agreeing with experimental result of  $-0.685$ . But it had difficulty explaining the  $\Delta^{++}$  particle which is a resonant state belonging to the spin  $3/2$  baryon decuplet. This particle is a ground state, consisting of three  $u$  quarks with their spins aligned in up direction, leading to a totally symmetric three quark wavefunction. This total symmetry of the three quark wavefunction is clearly in violation of the Pauli principle for fermions.

Another quantum number, called color, was introduced in 1965 [4] to solve the problem. The hypothesis was that quarks could have three different colors, red (R), green (G), and blue (B), and that hadrons made of quarks were colorless, meaning that they were color singlets. For a baryon, each of

the three quarks inside carries a different color to make a color-neutral state, its antisymmetric color singlet wavefunction is

$$qqq_{color} = \frac{1}{\sqrt{6}}(RGB - RBG + BRG - BGR + GBR - GRB), \quad (1.3)$$

making the overall baryon wavefunction antisymmetric. For a meson, one quark carries a color and the antiquark carries the anticolor to make a color-neutral particle.

The color hypothesis is supported by experiment results. In  $e^+e^-$  collisions of center-of-mass energy above 10 GeV, the cross section ratio of  $\sigma(e^+e^- \rightarrow hadrons)/\sigma(e^+e^- \rightarrow \mu^+\mu^-)$  is independent of the energy, and is proportional to the number of colors. Without the color quantum number, this ratio from the theoretical prediction is three times lower than that from the experimental measurement.

## 1.2 Parton Distribution Function and QCD

When first postulated to explain the symmetries among hadrons, quarks were merely mathematical entities. The first experimental evidence of hadrons having pointlike constituents came from deep inelastic lepton-nucleon scatterings in late 1960s [5][6]. It was found that the total cross section for neutrino-nucleon interactions was nearly linear with the neutrino energy up to 200 GeV. This result could be explained by Feynman's parton model [7], in which hadrons are made of loosely-bound pointlike particles called partons. Neutrinos interact with quasifree partons, instead of interacting

with the nucleon as a whole, and scatter off them elastically. At energies much larger than the mass of the parton, the neutrino elastic cross section is proportional to its energy. This behaviour is expected from the elastic scattering between two weak-interacting point particles. So the neutrino-nucleon inelastic scattering can be interpreted as the consequence of neutrino-parton elastic scattering.

It turned out that quarks are only one of two kinds of partons. They carry about one half of the hadron momentum, the other half is carried by another kind of parton, called gluons. Gluons are electrically neutral and massless vector bosons, they are colored and belong to an octet representation of a color SU(3) group. They only interact by the strong interaction and play a similar role in strong interactions as photons do in electromagnetic interactions. The strong interaction between quarks is believed to be mediated by gluons through color exchange. The difference between gluons and photons is that gluons carry color and can have self-interactions, while photons are electrically neutral and have no self-interactions. The theoretical framework which describes the strong interaction is called Quantum Chromodynamics (QCD).

Quarks and gluons share their parent hadron's momentum. The probability of a quark (gluon)  $a$  having a fraction  $x$  of hadron  $A$ 's momentum is called hadron  $A$ 's quark (gluon) structure function  $G_{a/A}(x_a)$ . The initial parton model predicts that the structure function depends on  $x$  only. This behavior is called Bjorken scaling [8]. The exact forms of the structure

functions, however, cannot be constructed by the model, they have to be measured experimentally.

One way to determine the nucleon structure is, once again, the deep inelastic lepton-nucleon scattering processes. Early results agreed with Bjorken scaling [9]. But at large lepton energy, there are signs of scaling violation believed to be caused by quarks emitting gluons at high energy. This changes the quark structure function so that it has a logarithmic dependence on the four-momentum transfer,  $Q$ , in the interaction.

Another source of  $Q$  dependence of cross sections is the coupling constant,  $\alpha_s$ , in strong interactions [3]. This constant can be written as

$$\alpha_s(Q^2) = \frac{12\pi}{(33 - 2n_f)\log(Q^2/\Lambda^2)}, \quad (1.4)$$

where  $n_f$  is the number of quark flavors, and  $\Lambda$  is a free parameter, ranging from 100 to 500 MeV and to be determined experimentally. This formula clearly indicates the  $Q$  dependence of the coupling constant. In the energy range of our study,  $\alpha_s$  is on the order of  $10^{-1}$ , so perturbative calculations can be carried out to predict parton interaction cross sections [10]. At  $Q^2 \gg \Lambda^2$ ,  $\alpha_s$  approaches zero, meaning that the partons can move freely inside the hadrons. This is so-called "asymptotic freedom".

Gluons do not interact with leptons, so their structure functions cannot be directly measured by deep inelastic lepton-nucleon interactions. Consequently, hadron-hadron hard scattering processes have to be used to determine the gluon structure functions. In principle, hadron-hadron collisions can provide detailed information about partonic interactions as indicated by

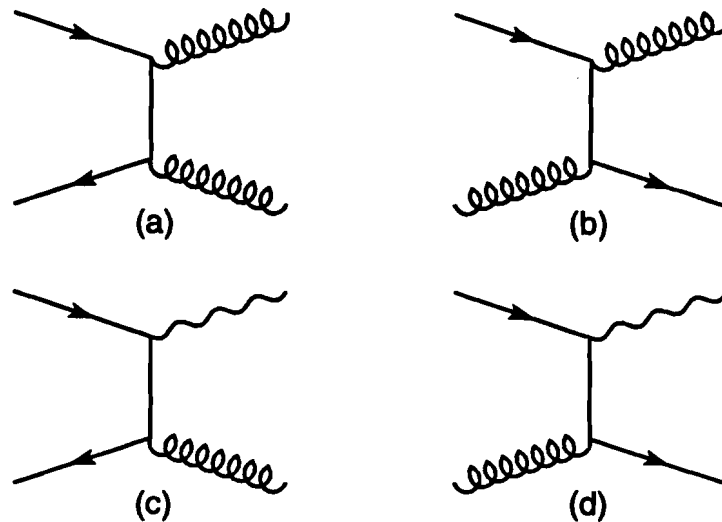


*Figure 1.2: Partonic Feynman diagrams. a): Quark-antiquark annihilation, producing two gluons; b): Gluon Compton scattering; c) and d): Corresponding direct photon production via annihilation and Compton processes.*

the two first order Feynman diagrams illustrated in Figure 1.2(a) and (b). Those processes can also be used to test the description of short-distance interactions used in studying deep inelastic scattering processes. However, there are experimental difficulties in disentangling the many partonic subprocesses involved in the collisions. Furthermore, partons do not appear as free particles and cannot be detected directly in experiment. A parton has to combine with one or more other partons to form a hadron after interaction. The parton hadronization process is called fragmentation. A fragmentation function,  $D_{C/c}(z_C)$ , describes the probability of obtaining a hadron  $C$  with a momentum fraction  $z_C$  from a parton  $c$ . The invariant cross section for the

inclusive production of hadron  $C$  is

$$E_C \frac{d^3\sigma}{dp_C^3}(AB \rightarrow C + X) = \sum_{abcd} \int dx_a dx_b dz_c G_{a/A}(x_a, Q^2) G_{b/B}(x_b, Q^2) \\ \times D_{C/c}(z_c, Q^2) \frac{\hat{s}}{\pi z_c^2} \frac{d\sigma}{d\hat{t}}(ab \rightarrow cd) \delta(\hat{s} + \hat{t} + \hat{u}), \quad (1.5)$$

where  $\hat{s}$ ,  $\hat{t}$ , and  $\hat{u}$  are parton Mandelstam variables, and the  $\delta$ -function ensures four-momentum conservation in the two-body scattering of massless partons. The incoherent summation is over all possible partonic subprocesses.

### 1.3 Direct Photon

If the out-going gluon in Figure 1.2(b), and one of the two gluons in Figure 1.2(a) are replaced by photons, we obtain the two first order direct photon production Feynman diagrams as illustrated in Figure 1.2(c) and (d). The term “direct photon” is applied to photons originating from an interaction directly related to the parton-parton scattering, rather than photons coming from decays of other particles produced in the interaction.

The direct photon production is expected in the framework of QCD, and its cross section can be calculated based on the theory. But to quantitatively compare theoretical calculations with experimental results, one has to include second order diagrams and the intrinsic transverse momentum of partons inside hadrons. Two reviews on experimental and theoretical aspects of direct photon production can be found in references [11] and [12], respectively.

One of the vertices in the two first order Feynman diagrams is electromagnetic, and the pointlike coupling between a photon and a quark is well understood. In the two first order processes, direct photons are either initiated by a gluon (in Compton scattering) or accompanied by a final gluon jet (in annihilation process). If those two processes can be isolated, the direct photon production can be used to study the gluon structure function in nucleons and the gluon fragmentation function.

Equation 1.5 can be simplified to calculate the inclusive direct photon cross section

$$E \frac{d^3\sigma}{dp^3}(AB \rightarrow \gamma + X) = \sum_{abd} \int dx_a dx_b G_{a/A}(x_a, Q^2) G_{b/B}(x_b, Q^2) \times \frac{\hat{s}}{\pi} \frac{d\sigma}{dt}(ab \rightarrow \gamma d) \delta(\hat{s} + \hat{t} + \hat{u}). \quad (1.6)$$

From QCD calculations [13], the cross section of the Compton subprocess can be written as

$$\frac{d\sigma}{dt}(qg \rightarrow q\gamma) = \frac{-\pi\alpha\alpha_s}{3\hat{s}^2} e_q^2 \frac{\hat{u}^2 + \hat{s}^2}{\hat{s}\hat{u}} \quad (1.7)$$

and annihilation as

$$\frac{d\sigma}{dt}(\bar{q}q \rightarrow g\gamma) = \frac{8\pi\alpha\alpha_s}{9\hat{s}^2} e_q^2 \frac{\hat{u}^2 + \hat{t}^2}{\hat{u}\hat{t}} \quad (1.8)$$

where  $\hat{s}$  is the square of energy in the center of mass of the interacting constituents,  $\hat{t}$  the square of four-momentum transfer in the processes,  $\hat{u}$  the third Mandelstam variable of the processes,  $\alpha$  is the fine-structure constant.  $e_q$  is the charge of the interacting quark.

From the quark contents of  $\pi^+$ ,  $\pi^-$ , and proton, and the quark charges involved, it is clear that the contribution from the annihilation process in the  $\pi^-p$  interaction is eight times of that in the  $\pi^+p$  interaction, while the Compton process contributions are the same for both interactions. So the annihilation process can be isolated by subtracting the cross section of  $\sigma(\pi^+p \rightarrow \gamma X)$  from  $\sigma(\pi^-p \rightarrow \gamma X)$ . In principle, quark structure functions and gluon fragmentation functions can be extracted from this procedure. In  $pp$  collisions, the Compton process dominates, while the annihilation can come only from sea quarks. So  $pp$  interactions can be used to study the Compton process and thus extract the gluon structure function for nucleons.

After the first experimental result on the direct photon signal was published in 1976 [14], several more experiments were carried out at both CERN and Fermilab. Their results indicate that the cross section ratio of the direct photon to the inclusive  $\pi^0$  increases with  $p_T$ . This trend is in agreement with QCD, since there is one less  $\alpha_s$  in direct photon cross section, in addition to no fragmentation function involved. The  $Q^2$  dependences (scaling violations) in both the strong running coupling constant and the fragmentation function speed up the fall-off of the single hadron cross section with  $p_T$ .

It seems that the direct photon is a powerful probe in verifying QCD and determining structure functions. But there are two major problems associated with studying direct photon production. First, its yield is low, so a large number of events must be accumulated to be able to extract the signal. Second, there is a substantial background coming from  $\pi^0$  and  $\eta$

decays. In order to remove the background, an experiment has to be able to reconstruct the neutral mesons with high efficiency.

So it is very important to understand the  $\pi^0$  and  $\eta$  production and to measure their production cross sections, before the direct photon signal can be extracted. In addition, the  $\pi^0$  and  $\eta$  production can itself serve as a test of QCD.

## 1.4 $\pi^0$ and $\eta$ Production

In 1973, three CERN ISR experiments [15][16][17] published their result on high  $p_T$  ( $> 2.0$  GeV) hadron production and found the yield was much larger than predicted from extrapolating low  $p_T$  ( $< 1.5$  GeV) results

$$\frac{d\sigma}{dp_T} \sim e^{-6p_T}. \quad (1.9)$$

Rather, the high  $p_T$  cross section seemed to follow the power law

$$\frac{d\sigma}{dp_T} \sim p_T^{-n}. \quad (1.10)$$

Transverse momentum is related to impact parameter in a collision. Large  $p_T$  is the result of a small distance interaction, and the excessive large  $p_T$  hadron production is an evidence of the pointlike nature of hadron constituents. From a naive parton model, it is expected that  $n = 4$  [18][19]. Instead, the experiments measured  $n = 8.24 \pm 0.05$ . This result was the first evidence of scaling violation, and it led to many theoretical studies and further experimental investigations. A detailed review on this subject can be found in reference [20].

*Table 1.2: Parameters of Three Recent Fixed Target Experiments*

Experiment	Beam	Beam Momenta	Target	$p_T$ (GeV/c)	Rapidity
NA3	$\pi^\pm, p$	200 GeV/c	C	3 – 6	-0.4 – 1.2
WA70	$\pi^\pm, p$	280 GeV/c	H <sub>2</sub>	4 – 7	-1.0 – 1.0
NA24	$\pi^\pm, p$	300 GeV/c	H <sub>2</sub>	2.75 – 7	-0.8 – 0.8

A  $\pi^0$  or  $\eta$  produced at large  $p_T$  in the energy range of our study ( $\sqrt{s} \approx 24$  GeV) in  $\pi p$  or  $pp$  interaction is most likely the leading fragment of the scattered valence quark. It carries more than half of the momentum of the scattered parton. Thus the measurement of those leading particles can provide some insight into the parton interactions. The differential cross section of  $\pi^0$  and/or  $\eta$  production in certain  $p_T$  ranges can provide information on the magnitude of the scaling violation and serve as a test of theoretically proposed structure and fragmentation functions.

There have been many experiments, since the pioneering IRS experiments, studying high  $p_T$  single hadron and/or direct photon production. Three of the recent experiments, NA3[21], WA70[22], and NA24[23], used same types of beams as E705 did. Their beam energies, experimental targets and kinematic ranges are listed in Table 1.2. Their measurements will be compared with our experiment results in Chapter 9.



## Chapter 2

# Experiment Setup

The Experiment 705 [24] was designed to study the high  $p_T$  direct photon processes described in the previous chapter, as well as to study the charmonium states. It took data at the High Intensity Laboratory on the Proton-west beamline of Fermilab, during the 1987-1988 fixed-target run. The experimental setup included the Proton-west secondary beamline and the E705 spectrometer. The PW beamline, as shown in Figure 2.1, using a set of dipole and quadrupole magnets, was capable of delivering 300 GeV/c secondary proton (anti-proton) and charged pion beams to the experiment area.

The E705 spectrometer, as shown in Figure 2.2, consisted of a  ${}^7\text{Li}$  target, an analysis magnet, a charged particle tracking system, an electromagnetic calorimeter, and a set of muon counters.

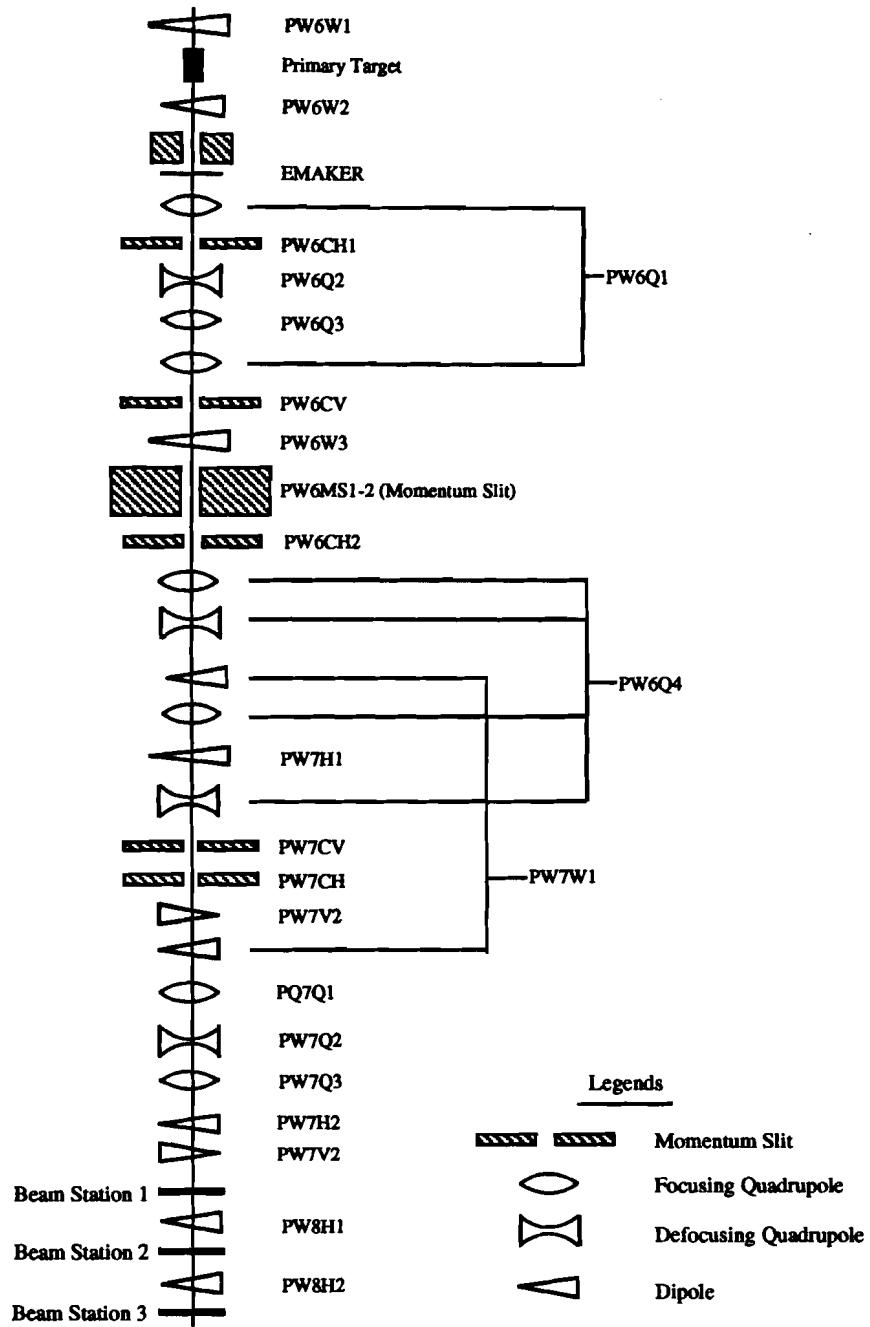


Figure 2.1: Top view of the Proton-west secondary beam line.

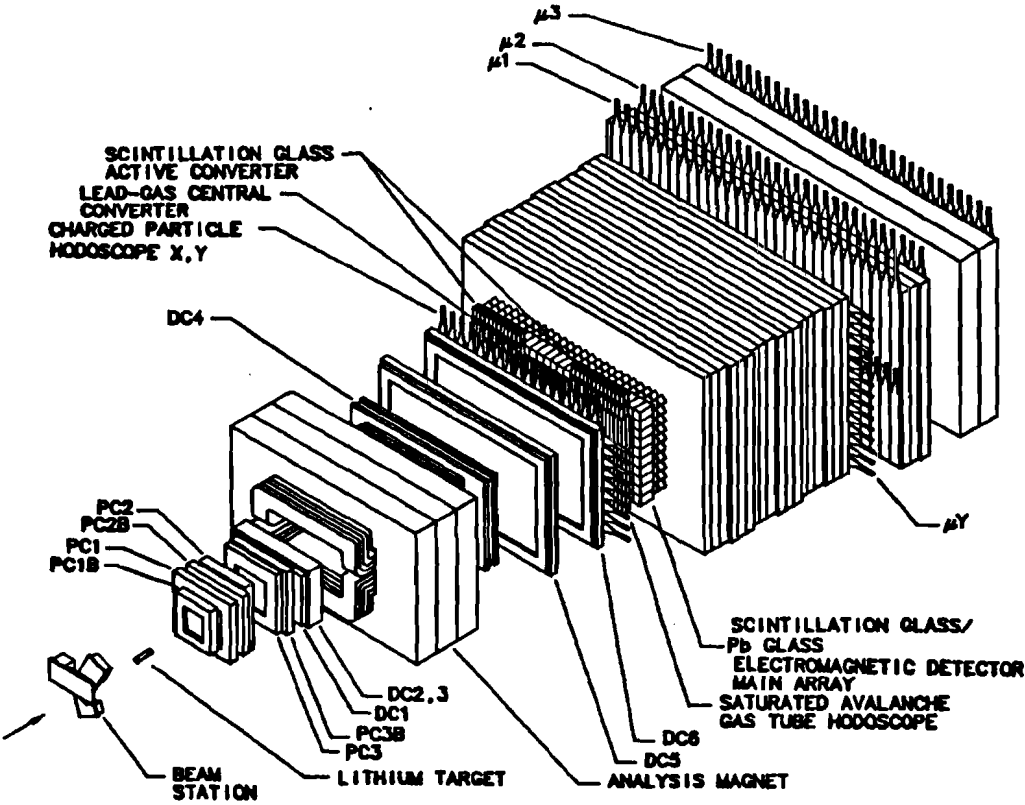


Figure 2.2: E705 Spectrometer.

## 2.1 Beam

The 800 GeV/c proton beams delivered to various experimental areas were extracted from the Fermilab Tevatron. There were typically  $10^{13}$  protons in each 23-second beam spill. The frequency of the RF cavity in the beam line was 53.1 MHz, resulting in a substructure of beam bunches (buckets) spaced 19 ns apart.

The beams used in E705 were primarily 300 GeV/c protons, anti-protons and charged pions whose trajectories were measured by three proportional wire beam chambers. And the particle identifications were achieved by two threshold Cerenkov counters.

### 2.1.1 The Secondary Beam to the Experiment

Primary protons of 800 GeV/c extracted from the Tevatron were sent through a series of magnets onto a beryllium target producing mainly pions and protons. The typical number of primary protons delivered to the target was on the order of  $10^{12}$ . The beamline optics downstream of the Be target could be adjusted to deliver different types of beam particles with different intensities to the experiment hall.

The experiment could run at *charged* mode, or *neutral* mode, or the combination of the two (*hybrid* mode). In the charged mode, the primary protons were directed to hit the target at an angle with respect to the beam line direction. The dipole PW6W2 could sweep either the positively or negatively charged particles away to the beam dump to select either the negative beam

(mostly  $\pi^-$ ) or the positive beam (mainly  $\pi^+$  and  $p$ ). The momentum of these charged particles was selected by the dipole PW6W3 and momentum slits PW6MS1/2 and it was set to 300 GeV/c. The typical secondary beam particle rate delivered to the experiment was about 5 MHz.

In the neutral mode, the primary particles hit the target straight on. The PW6W2 magnet was run at its full power to kick away almost all the charged particles, leaving only the neutral particles. The decay products,  $\pi^-$  and  $\bar{p}$  from the neutral particles  $\bar{K}^0$  and  $\bar{\Lambda}^0$ , formed the negative beam. The anti-proton component was about 8% in this condition, as compare to almost none in the negatively charged mode. But the overall beam rate was much lower in neutral mode. The experiment ran for some times in the hybrid mode to balance the rate and  $\bar{p}$  component. The typical beam content was about 98.5% of  $\pi^-$  and 1.5% of  $\bar{p}$  in this mode.

The electron (positron) beam used in the calibration of the electromagnetic detector was produced by inserting a lead plate, *EMAKER*, into the beamline in the neutral mode. Photons in the beamline were effectively converted into  $e^+e^-$  pairs. Again, the dipole PW6W3 and momentum slits PW6MS1/2 were used to select electron beams at 2, 6, 10, 30, 60, and 100 GeV/c.

### 2.1.2 Beam Stations

The beam trajectory was measured by three beam stations along the beam line. These beam stations, each of which had a beam chamber and a beam

hodoscope, were also used in the beam definition logic.

The beam chamber was a proportional wire chamber with three planes of  $Y$ ,  $U$ , and  $V$ . The wires in  $Y$  plane were along the  $x$ -axis, and those in  $U$  plane and  $V$  plane were tilted  $-60^\circ$  and  $+60^\circ$  with respect to the  $Y$  wires, respectively. Wire spacings in all three planes were 1 mm.

The distance between the first and the last beam chambers were 56.85 m. This long leverage gave a very good beam angular resolution.

Each beam hodoscope was a set of eight scintillation counters, stacked horizontally on top of each other. All the counters had the same length of 13 cm, while their widths increased with the distances to the center of the beam. Signals from the counters were latched, and their outputs were *OR*ed and summed together to form two logic outputs,  $BY_i$  and  $\sum BY_i$ , with  $i$  running from 1 to 3 to represent three different hodoscopes. The threshold of the summation logic could be adjusted so that if the number of hit counters exceeded  $N$ , the output from the logic would be high.  $N$  was set to one at the early part of the run, and was changed to two later to enhance the interaction rate. The *OR* of the sums after discriminating,  $BG$ , was used in the beam definition to veto the multiparticle buckets,

$$BG = (\sum BY_1 > N) + (\sum BY_2 > N) + (\sum BY_3 > N), \quad (2.1)$$

where  $N$  was 1 for the early part of the run and was 2 for the later part of the run. The schematic of the beam definition logic is illustrated in Figure 2.3. The early beam definition required a hit in one, and only one counter in each beam hodoscope, while the later definition would allow two particles in

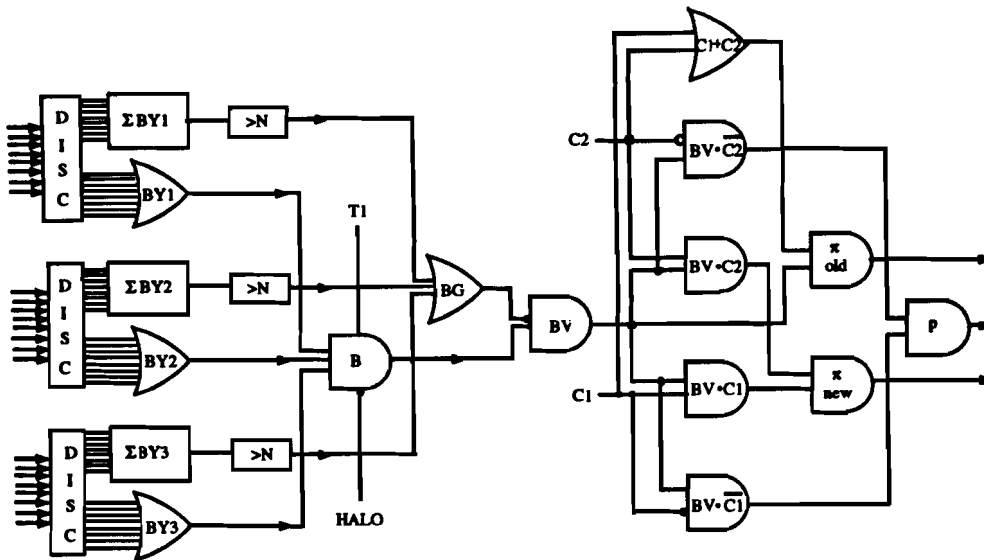


Figure 2.3: Beam definition logic.

a single beam bucket. The double occupancy of beam particles introduced by the latter beam definition was corrected in off-line analysis.

The signal of each counter of beam station 2 was also latched.

### 2.1.3 Cerenkov Counters

Two threshold Cerenkov counters, filled with helium gas, were used to tag pions, protons and antiprotons. The thresholds of the counters were set to just below the 300 GeV/c proton mass by changing the gas pressures during the normal running condition. Kaon contaminations in the pion samples were about 10% in the positive beam, and were negligible in the negative beam. The thresholds could also be adjusted to tag electrons from 2 to

100 GeV/c for calibrating the electromagnetic calorimeter.

At the early stage of the experiment, the pion beam definition required that both counters produce light, but the efficiencies of the counters were only about 92%. This resulted in about 15% loss of the pion sample. To enhance the pion rate, the pion definition was changed to require light from one or both of the Counters. The proton beam definition always required that no counter be lit. Particle production cross sections by pion and proton beams were corrected according the beam definition and the Cerenkov counters' efficiencies. The estimated kaon contamination in the pion sample was also taken into account.

#### 2.1.4 T1 Counter

The T1 was a plastic scintillation counter mounted in front of the target used as the experiment timing reference. Its signal was also one of the elements marking the presence of beam particles.

#### 2.1.5 Veto Walls

The veto wall was a set of scintillation counters, forming  $x$  and  $y$  planes. The 22 counters in the  $x$ -plane covered an area of  $408 \times 147 \text{ cm}^2$ , while the 16 counters in the  $y$ -plane covered an area of  $306 \times 153 \text{ cm}^2$ . Both planes had a rectangular beam hole of  $8.8 \times 25.4 \text{ cm}^2$  hole in the center.

The wall was used to detect halo muons accompanying beam particles.

The halo signal was defined as:

$$HALO = \sum VX_i + \sum VY_i$$

### 2.1.6 Beam Logic

A hit in the beam hodoscopes BY1, BY2, and BY3 and the T1 counter was required for a good beam particle. The coincidence of the four elements was vetoed by the *HALO* to exclude beam particles with halo muons in the same bucket.

$$B = BY1 \cdot BY2 \cdot BY3 \cdot T1 \cdot \overline{HALO}$$

The output was further set in anti-coincident with *BG* to eliminate interactions caused by multiparticle buckets.

The pion and proton were defined as

$$\pi : (\overline{BV} \cdot C1) \cdot (\overline{BV} \cdot C2) \quad \text{for first 1/4 of the data}$$

$$\overline{BV} \cdot (C1 + C2) \quad \text{for last 3/4 of the data}$$

$$p(\bar{p}) : (\overline{BV} \cdot C1) \cdot (\overline{BV} \cdot C2)$$

The beam was then defined as

$$BEAM = \pi + p$$

## 2.2 Target

A 33 cm long  ${}^7\text{Li}$  cylinder of 5 cm radius was used as the experiment target. Its density was 0.529 g/cm<sup>3</sup>. Its length was equivalent to 0.175, 0.174, 0.238,

and 0.253 interaction lengths for 300 GeV/c  $\pi^+$ ,  $\pi^-$ ,  $p$ , and  $\bar{p}$ , respectively. The target was nearly an isoscalar. This feature is particularly useful for studying the direct photon production. Since the production of  $\pi^0$  should be equal from  $\pi^+$  and  $\pi^-$  by the isospin argument, and its contribution to the background of direct photon production cancels out in the cross section difference:  $\sigma(\pi^- Li \rightarrow \gamma + X) - \sigma(\pi^+ Li \rightarrow \gamma + X)$ .

## 2.3 Interaction Trigger

Only about 20% of the beam particles reaching the target would produce secondary particles; the rest would pass through the target without any interaction. To detect the occurrence of an interaction, the experiment relied on a set of scintillation counters known as the charged particle hodoscopes.

### 2.3.1 Charged Particle Hodoscope

The charged particle hodoscope, located about 9.5 m downstream of the target, consisted of an  $x$ -plane(CPX), with total of 184 scintillation counters covering an area of  $384 \times 200$  cm<sup>2</sup>, and a  $y$ -plane(CPY) with 48 counters forming a  $400 \times 188$  cm<sup>2</sup> wall. Both the  $x$  and  $y$  planes had a hole of  $30 \times 15$  cm<sup>2</sup> in the center, allowing the non-interacting beam particles to pass through.

The 184 CPX counters were stacked on their ends to form two rows with an equal number of counters in each row. Signals produced by charged particles in the counters in the bottom and top rows with the same  $x$  position

were wired together to form a total of 92 signals. Those signals were latched individually for use in the off-line charged track reconstruction program. For the on-line trigger, the 92 signals were sent to a summation logic whose threshold was set at two hits in counters, in the similar way as mentioned in Section 2.1.2.

The 48 CPY counters were divided into two columns, and they formed 24 individual signals in a similar fashion to the CPX counters. The output from the summation logic was *AND*ed together with that from CPX to form a  $CPH \geq 2$  logic

$$CPH \geq 2 = \sum CPX_i \geq 2 \cdot \sum CPY_j \geq 2.$$

### 2.3.2 The Interaction Trigger

An interaction occurred if a beam particle met the requirements of the beam definition, hit the target, and produced at least two charged particles:

$$INTERACTION = BEAM \cdot \sum CPX_i \geq 2$$

## 2.4 Analysis Magnet

A large aperture dipole analysis magnet (Rosie) was employed in the experiment to bend charged particles and to measure the momenta of those particles. It operated at 2100 A, producing a field of 5 kG. The dimensions of the magnet were  $91.4 \times 185.5 \times 152.4$  cm<sup>3</sup>. This gave a momentum kick of 0.776 GeV/c in the  $x$ - $z$  plane.

A 22 cm thick iron plate was mounted at the downstream end of Rosie to reduce the fringe field effect on the downstream detectors, particularly the phototubes of the electromagnetic detector.

The center of the magnet served as the origin of the experiment coordinate system. The  $x$  was pointing west,  $y$  upwards, and  $z$  in beam direction.

## 2.5 Wire Chamber System

The charged particle tracking system consisted of six proportional wire chambers (PC1, PC2, PC3, PC1B, PC2B, and PC3B), three drift chambers (DC1, DC2, DC3) upstream of the analysis magnet, and three drift chambers (DC4, DC5, DC6) downstream of the magnet. The specifications, resolutions, and the  $Z$ -locations of the chambers are listed in Table 2.1

The particle intensity around the beam was very high with wires running across the center having a high hit rate. Those wires would not be efficient for detecting the hits in the outer region. To reduce the inefficiency due to the high hit rate in the center, PC1,2,3 all had been desensitized in the central region by electroplating to thicken the wire. The radii of the deadened regions were 5.08 cm, 5.08 cm, and 6.35 cm for PC1, PC2, and PC3, respectively.

The central region was covered by three other chambers (PC1B, PC2B, and PC3B), with finer wire spacing [25].

The upstream drift chambers had three planes ( $X$ ,  $U$ , and  $V$ ), while the downstream ones had four planes ( $X$ ,  $X'$ ,  $U$ , and  $V$ ). The wires in the  $U$ ,

Table 2.1: Chamber Specifications, Resolutions, and Their Z-locations

Chamber	Plane	Dimension (cm <sup>2</sup> )	Spacing (cm)	Resolution ( $\mu$ m)	Z-position (cm)	Angle( $\theta_{zy}$ ) (degree)
PC1	X'	52 × 29	0.151	579	-406.4	0.0
	V		0.158	666	-405.2	-16.7
	X		0.151	691	-403.9	0.0
	U		0.158	579	-402.6	+16.7
PC2	U	76 × 40	0.159	662	-335.0	+16.7
	X		0.151	721	-333.7	0.0
	V		0.159	616	-332.4	-16.7
PC3	V	106 × 50	0.209	727	-266.8	-16.7
	X		0.200	794	-265.6	0.0
	U		0.209	704	-264.4	+16.7
PC1B	V	60 × 30	0.085		-427.8	-28.1
	X		0.075		-427.2	0.0
	U		0.085		-426.6	+28.1
PC2B	V	75 × 40	0.085		-380.5	-28.1
	X		0.075		-379.9	0.0
	U		0.085		-379.3	+28.1
PC3B	V	90 × 50	0.113		-244.9	-28.1
	X		0.100		-244.3	0.0
	U		0.113		-243.7	+28.1
DC1	U	50 × 50	0.600	404	-216.4	+16.7
	X		0.600	374	-215.7	0.0
	V		0.600	476	-215.1	-16.7
DC2	V	50 × 50	1.270	383	-194.8	-16.7
	X		1.270	376	-193.6	0.0
	U		1.270	407	-192.3	+16.7
DC3	U	50 × 50	1.270	384	-180.9	+16.7
	X		1.270	377	-179.6	0.0
	V		1.270	333	-178.3	-16.7
DC4	V	200 × 100	1.905	598	172.0	-16.7
	X		1.905	675	173.9	0.0
	U		1.905	669	175.8	+16.7
	X'		1.905	718	177.7	0.0
DC5	X'	335 × 167	1.905	554	273.9	0.0
	V		1.905	483	275.6	-16.7
	X		1.905	373	277.7	0.0
	U		1.905	513	279.6	+16.7
DC6	X'	335 × 167	1.905	737	378.6	0.0
	V		1.905	524	380.5	-16.7
	X		1.905	665	382.4	0.0
	U		1.905	698	384.3	+16.7

$V$  planes were rotated  $\pm 16.7^\circ$  with respect to the  $Y$ -axis. The  $X'$  wires were offset one half wire spacing to the  $X$  wire. In addition to tracking the charged particles, DC4, DC5, and DC6 were used in a trigger processor to determine the di-muon mass.

## 2.6 Electromagnetic Detector

The electromagnetic detector consisted of two scintillation glass active converter planes, a gas tube hodoscope, a lead gas calorimeter, and a scintillation glass-lead glass main array. It was the main component used to study the topics in this thesis, and will be discussed in more detail in the following chapters.

## 2.7 Muon Counters

The muon detector, located behind the electromagnetic detector, completes the the E705 spectrometer. It consisted of four planes of scintillation counters to detect muons and three shielding walls to absorb hadrons.

The 96 counters in the first plane (MUY) were stacked horizontally in four columns, forming a wall of  $620 \times 285 \text{ cm}^2$ . They were behind a shield of 0.41 m of copper and 3.10 m of steel. The MU1 counters were erected immediately after the MUY counters. Those 60 counters were hang vertically to form top and bottom rows. A wall of 0.61 m of steel sat between the MU1 counters and the plane of 62 MU2 counters. Another shield of 0.91 m of concrete followed the MU2 plane. The 62 MU3 counters right after the

concrete completes the muon detector. The dimensions of the three vertically arranged planes were  $618 \times 290 \text{ cm}^2$ ,  $671 \times 315 \text{ cm}^2$ , and  $723 \times 352 \text{ cm}^2$  for MU1, MU2, and MU3, respectively.

The total nuclear absorption length of the shields is about  $22 l_I$ . This was sufficiently thick to absorb all of the hadrons coming from the interaction. The minimum energy carried by a muon to go through the shields was about 6 GeV.



## Chapter 3

# The Electromagnetic Detector

One of the main subjects of the E705 was to study the high  $p_T$  direct photon production. The major background to the direct photon production is from  $\pi^0$  and  $\eta$  decaying into two photons. The three main contributions are:

- One of the photons from a  $\pi^0$  ( $\eta$ ) decay misses the detector;
- Photons from the same  $\pi^0$  or different  $\pi^0$  overlap;
- Very asymmetric  $\pi^0$  ( $\eta$ ) decay leading to a very low energy photon which might be lost due to reconstruction efficiency.

To minimize the background, the electromagnetic detector needed a large aperture, good position resolution, and a large dynamic range. It is also important to have a detector with high radiation resistance, so that the detector can be exposed to high intensity particle beams which are necessary for accumulating substantial statistics for the subject of this study.

Based mainly on the above considerations, an electromagnetic detector, shown in Figure 3.1, was built by the E705 collaboration. It consisted of a

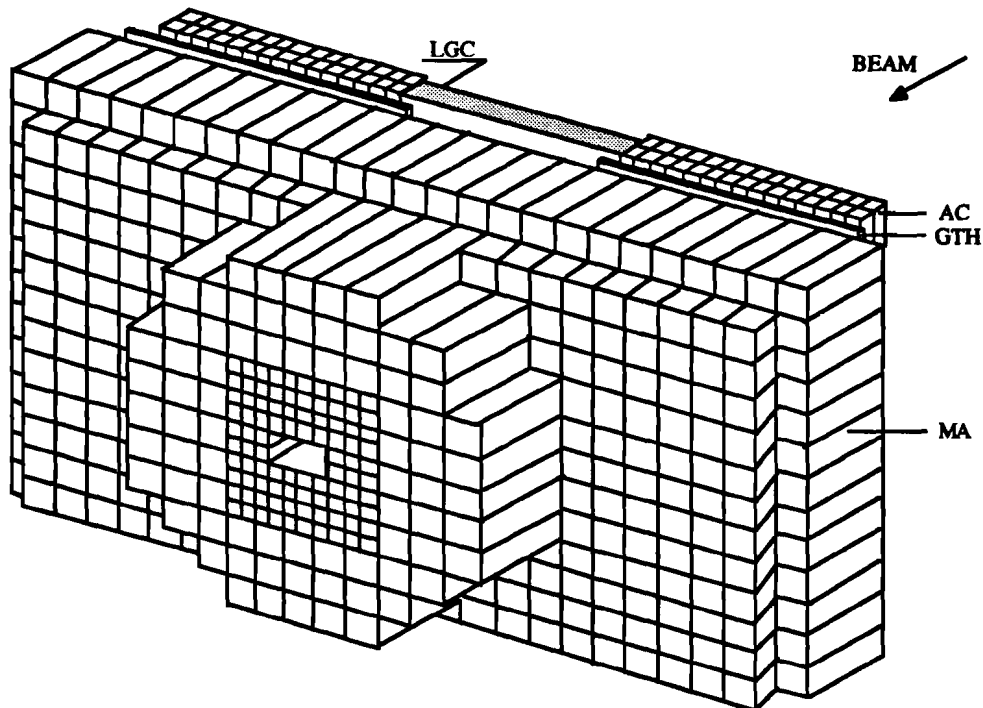
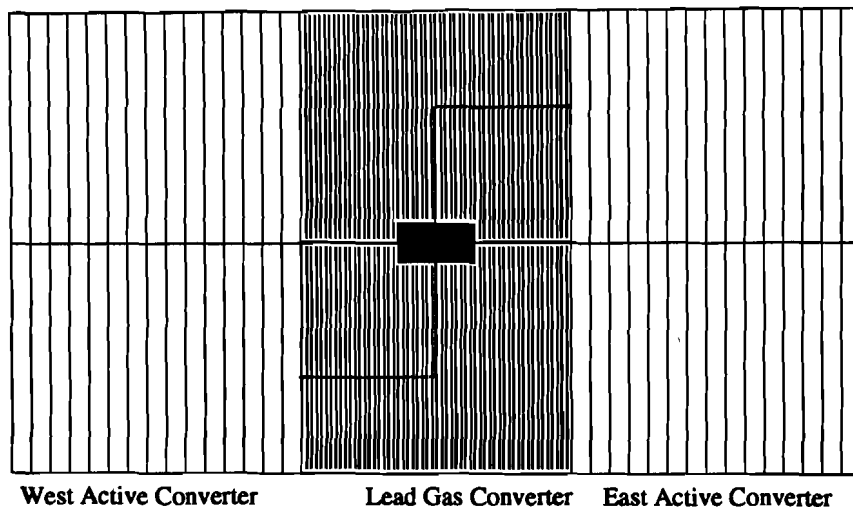
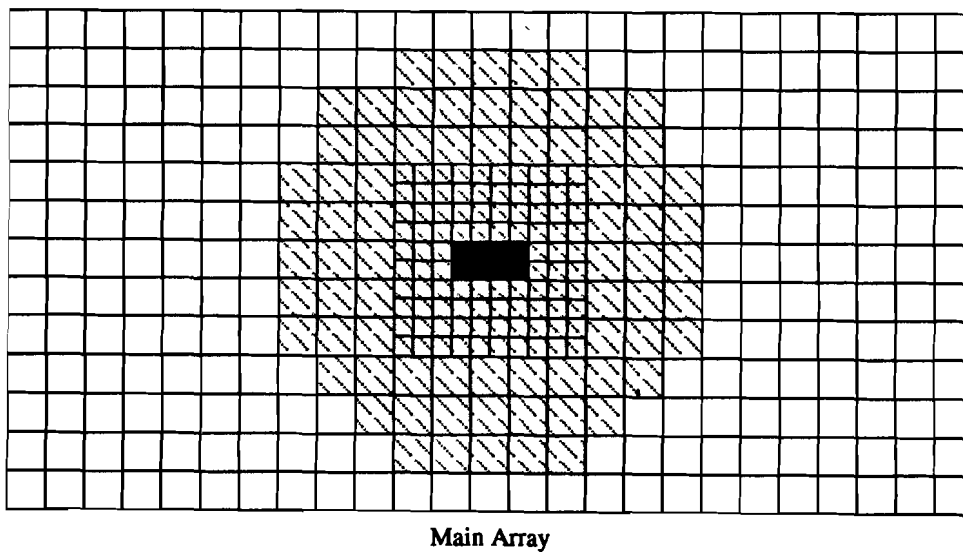


*Figure 3.1: The electromagnetic detector.*

front part which started a shower and measured its energy and position, and a back part which absorbed the rest of its energy. The front part included two layers of active converters (AC), a lead gas calorimeter (LGC), and a gas tube hodoscope (GTH). The AC and the LGC were collectively called the active planes. Their front view is shown in Figure 3.2(a). The back part had a main array (MA) of scintillation and lead glass blocks. Its front view is shown in Figure 3.2(b)



(a)



(b)

*Figure 3.2: Front view of the calorimeter. a): Front portion; b): Back portion. Scintillation glass blocks are located in the central hatched area, and lead glass blocks are located in the outer region.*

Table 3.1: The Characteristics of SCG1-C Glass and SF5 Glass

	SF5 Glass	SCG1-C Glass
Composition(by weight)	PbO 55%	BaO 43.4%
	SiO <sub>2</sub> 38%	SiO <sub>2</sub> 42.5%
	K <sub>2</sub> O 5%	Li <sub>2</sub> O 4.0%
	Na <sub>2</sub> O 1%	MgO 3.3%
		K <sub>2</sub> O 3.3%
		Al <sub>2</sub> O <sub>3</sub> 2.0%
		Ce <sub>2</sub> O <sub>3</sub> 1.5%
Radiation Length	2.54cm	4.35cm
Index of Refraction	1.673	1.603
Speed	<20nsec*	≈ 70nsec**
Density	4.08 g/cm <sup>3</sup>	3.41 g/cm <sup>3</sup>

\*Limited by phototube signal widths

\*\*Flourecent lifetime

### 3.1 Scintillation Glass and Lead Glass

The scintillation glass used in the calorimeter was the SCG1-C type manufactured by Ohara Optical Co.. Its characteristics, along with that of the SF5 lead glass are listed in Table 3.1. Both kinds of glasses contain large percentages of large  $Z$  materials. This ensures a rapid development of the electromagnetic showers in the glasses.

The difference between the lead glass and the scintillation glass lies mainly in the photon statistics. In the lead glass, the total amount of the Cerenkov light produced by the showering particles above threshold is proportional to the total path lengths of the particles, which in turn is proportional to the energy of the showering particle entering the glass. So

the Cerenkov light is a good measure of the energy of the incident particle. But the Cerenkov radiation is the only source of light seen by the photo-multiplier mounted on the end of each glass block. In addition to the amount of Cerenkov light radiated out being small, the photon statistics is further worsened by the absorption of the Cerenkov light in the glass,

In the scintillation glass, both scintillation light and Cerenkov light are emitted. The scintillator,  $Ce_2O$ , acts as a wavelength shifter for the blue-to-near-ultraviolet Cerenkov light. It absorbs the light and re-emits it with a longer wavelength which can survive the absorption of the glass. The results of E705 test run [26] at SLAC showed that the Cerenkov light accounts for only about 15% of the light produced in the SCG1-C for an electromagnetic shower. For a 4 GeV shower, the light output from the scintillation glass is about five times of that from the lead glass.

Thus, the energy resolution of the scintillation glass is better than that of the lead glass. The test result also showed that the scintillation glass has an excellent resistance to radiation damage.

## 3.2 Active Converter

The active converters were small scintillation blocks with dimension of  $7.5 \times 97.5 \times 7.5$  cm<sup>3</sup>. There were total of 128 AC blocks. Those blocks formed two layers along the beam direction. Each layer had two rows which were positioned vertically on their ends. The 64 blocks at east wing covered an area of  $120 \times 195$  cm<sup>2</sup> with its inner edge at  $x = 52.5$  cm, flush with the

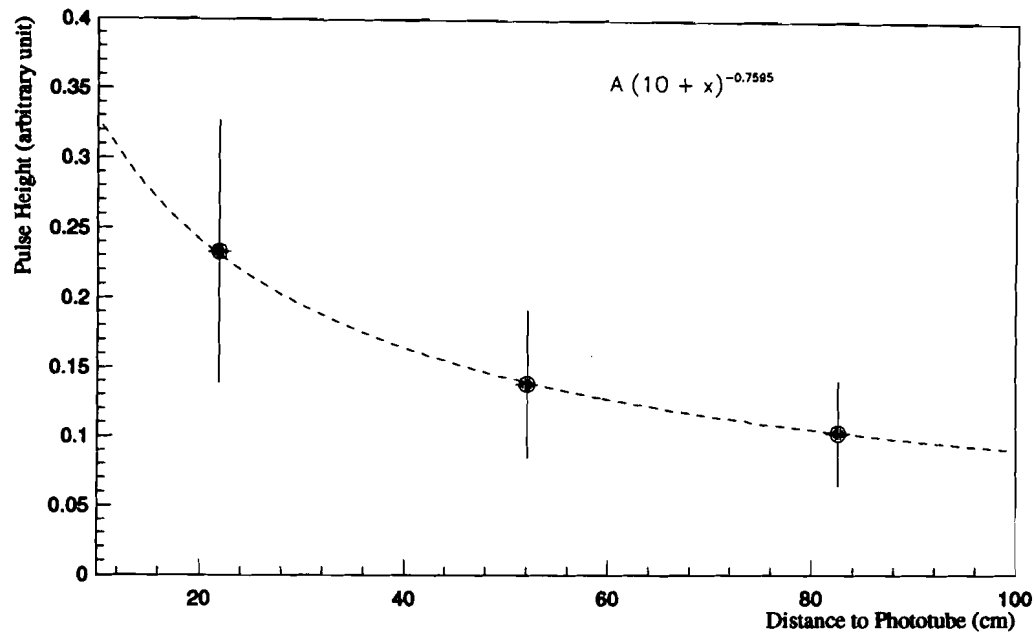


*Figure 3.3: A typical active converter light attenuation curve.*

inner edge of the 9th column of the main array blocks. Every two AC blocks covered one MA block in  $x$ . The west wing mirrored the east wing. The gap between the rear edge of the converter and the front face of the main array was 14 cm.

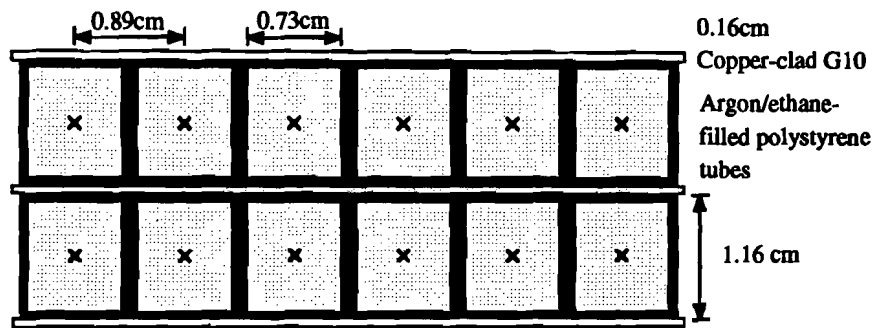
A RCA 6342A photomultiplier tube was mounted on each free end of the converter. The light produced by high energy showers had to travel along the  $y$  direction to reach the phototube, therefore the number of photons collected by the phototube will be different for the same energy electrons hitting at different  $y$  positions of the converter. A typical attenuation curve is shown in Figure 3.3.

The total radiation length of the active converters along the beam direction was  $3.45X_0$ . This length was sufficiently long to initiate a shower for most photons and electrons and to have a good portion of the shower energy deposited in it. In contrast, hadrons have much smaller probability (28% for  $\pi$ 's of 30-300GeV) to interact and deposit large amount of energy in the converter. The energy measured in the active converter was a major quantity used in analysis to reject hadrons.

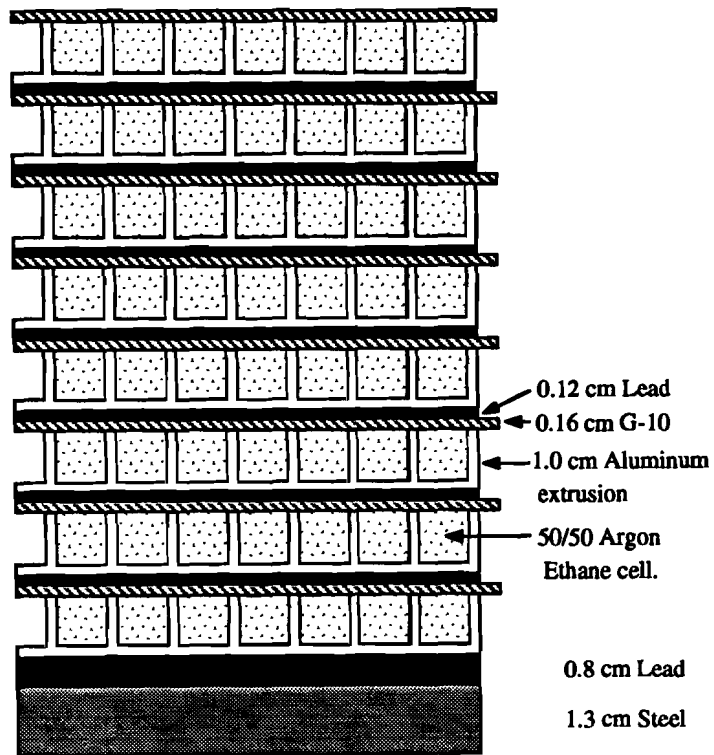
### 3.3 Gas Tube Hodoscope

The GTH [27] was divided into two halves, and placed behind the AC to determine the shower position. Two planes of conducting plastic tubes of effective width of 0.88 cm, with wires in their centers on a high voltage of 2100 V, were used to measure the  $x$  position. The planes were sandwiched between three planes of double sided copper-clad G-10 boards. The central G-10 board was grounded, while the inner copper surfaces of the two outer G-10 boards were cut into 0.88 cm wide horizontal strips, and the induced charges on these strips from the near-by tubes measured the  $y$  position of a shower.

A top view of a portion of the GTH is shown in Figure 3.4(a). Signals from the tubes (strips) with the same  $x$  ( $y$ ) in the two planes were wired together. There were 158 tubes in  $x$  and 216 strips in  $y$  in each half of the GTH. They cover an active area of  $139 \times 190$  cm<sup>2</sup>. Every adjacent two tubes of the outer 110 tubes were ganged together to give one signal. So there are



(a)



(b)

Figure 3.4: Top view of a portion of the hodoscopes. a): GTH; b): LGC.

total of 103  $x$  channels and 216  $y$  channels in each half of the GTH.

### 3.4 Lead Gas Calorimeter

The LGC [28] was an eight-layer sampling device used to measure energies, as well as positions of showers in the central region of the calorimeter. Each layer consisted of a 1.2 mm lead sheet, vertically mounted proportional tubes, and a copper clad G-10 sheet of 1.6 mm thick. The voltage on the gold-plated tungsten wire suspended in the center of each tube was about 1850 V. The copper sheet on the G-10 board was etched into 1.25 cm horizontal strips. Figure 3.4(b) shows a part of the LGC assembly .

The energy that a shower lost in the lead radiator was measured by the amount of ionization in the 50/50 argon-ethane gas mixture filled in the tubes immediately following the lead. Signals from the eight tubes (strips) with the same  $x$  ( $y$ ) position were summed together, and amplified before being sent to the read-out electronics. They provided a profile of the shower, and were used to measure the shower position as well.

Each  $x$  tube was electrically divided in the middle ( $y = 0$ ), giving two signals at top and bottom ends of the wire. Effectively, there were 104 tubes in both top and bottom  $x$ -planes, extending  $\pm 90.5$  cm in  $y$  direction. There were total of 144  $y$  strips. But the 80 strips in the middle were read out at each end, with a cut-off at  $x = 0$ , making a total of 224  $y$  channels. This was to make fewer false crossings in the  $x$ - $y$  match-ups in the busy central region.

The LGC covered the central area of  $103 \times 181 \text{ cm}^2$  with a hole of  $30 \times 15 \text{ cm}^2$  in the middle to let non-interacting beam particles through. It overlapped 10 cm with the GTH at each edge. The entire LGC was fronted by a 13 mm thick steel sheet and an 8 mm thick lead, leading to an overall thickness of 4.2 radiation lengths.

### 3.5 Main Array

To absorb the energy of a shower, the main array was positioned at the end of the calorimeter. It consisted of both lead glass (SF5) and scintillation glass (SCG1-C) blocks of different sizes, stacked with their longest dimension along the beam direction.

Ninety-two  $7.5 \times 7.5 \times 89.2 \text{ cm}^3$  small SCG1-C blocks were placed at the busiest central region. The smaller block size was to better distinguish overlapping showers. These blocks were surrounded by 72 large SCG1-C blocks of  $15 \times 15 \times 89.2 \text{ cm}^3$ , with 228 blocks of  $15 \times 15 \times 45 \text{ cm}^3$  lead glass blocks forming the outer-most region. The entire main array covered a cross section of  $325 \times 195 \text{ cm}^2$  with a  $30 \times 15 \text{ cm}^2$  beam hole in the center.

The light was collected by the 9-stage EMI-9791KB phototubes, and 10-stage RCA-6364A tubes for the large and small blocks, respectively. The phototubes were mounted at the downstream end of the blocks.

An optical fiber, supported by a Bakelite block, was glued to one of the perpendicular sides of a prism which was glued with Epotek 305 epoxy onto the upstream end of each glass block [29, Chapter 3]. Light coming from

a flashing LED system through the fiber was used to monitor, as well as to correct, gain changes in the glass-phototube system from time to time. The LED light intensity could be adjusted by inserting 12 different optical filters mounted on a wheel between the LED and the fibers. The filter wheel position 1 corresponded to an opaque filter, and position 12 corresponded to a transparent filter. The performance of the LED system will be discussed later.

The entire main array was enclosed in an air conditioned house to reduce the temperature effect on the phototube gains and the LED system. The temperature change during the run was within 1°F. The house, along with the front devices, sat on a table whose motion in 0.5 mm increments could be controlled locally or remotely by a VME/10 computer via CAMAC interface. The vertical and horizontal positions of the table were measured by two encoders. This enabled us to position the calorimeter and expose each block to electron beams for calibration as will be described in the next chapter.

### **3.6 Instrumentation**

The signals from the hodoscopes and the glass arrays were sent to electronic systems for processing. In the normal running condition, all the glass channels were recorded for each event, but only some of the hodoscope channels whose signals met certain requirements were read out. The main array signals were also used in a fast trigger processor called the Cluster Finder.

### 3.6.1 LGC and GTH

The signals from the hodoscope channels were amplified before they were sent to the ADC modules via 50-meter long RG8 cables. The amplification factors were 5 for LGC- $x$ , 25 for LGC- $y$ , 20 for GTH- $x$ , and 75 for GTH- $y$  channels.

The ADC cards were 12-bit LeCroy 2280 modules, each with 24 channels. They were distributed into four CAMAC crates. Each crate was controlled by a single processor. The charges in the hodoscope channels were read out after digitization through the processors.

In the normal data taking mode, the 2280's were running in *sparcified* mode to minimize the event record size. In this mode, the ADC's were pedestal-subtracted, and only the channels with ADC's counts above certain thresholds and their neighboring channels were read out. The threshold and the number of the neighbours, called the edge size, could be adjusted. The pedestals were obtained by running in unsparcified mode with test pulser triggers. They were recorded and loaded back into the 2280's for subtraction.

### 3.6.2 The Charge Amplifier and ADC Card

The output signal from the phototubes attached to glass blocks were cabled to the back panel of a custom made front-end/ADC card. The signal cable lengths were adjusted to match the timing. Figure 3.5 is a schematic of the charge card.

The input signal went through a current amplifier and integrated by a

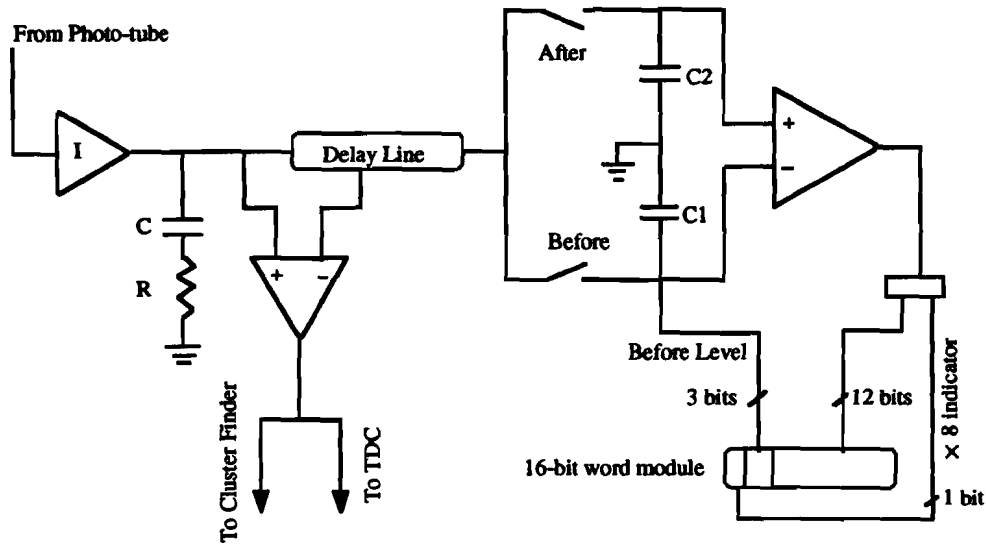


Figure 3.5: Schematic of the charge card.

resistor (R) in serial with a capacitor (C). The voltage across the RC circuit was

$$V(t) = a\tau(1 - \tau e^{-t/\tau} + RC e^{-t/\tau})/C \quad (3.1)$$

where  $a$  and  $\tau$  are the amplitude and the decay time constant of the input signal, respectively. The capacitance was chosen to produce output signals of the appropriate voltage into the ADC, and the resistance was determined by matching the RC value to the time constant  $\tau$  [30]. If there was no noise and fluctuation, the voltage would reach  $a\tau/C$  as soon as the input

became a decaying exponential. So the integrated signal was an almost-step function. But a resistor of effective resistance of 50K (not drawn on the schematic) was put in parallel with the integrating RC path to provide a slow charge leakage path for the capacitor, and to avoid charge saturation on the capacitor during high intensity running. This resistor resulted in a slow decay of the integrated signal after it reached its maximum height, and caused an interaction rate dependent dynamic pedestal to the signal [29, chapter 6].

This integrated signal was sent to a packaged delay line. The signal from a 160 ns tap point was subtracted from the undelayed signal. The output from the differential amplifier was a square wave whose height was proportional to the total charge of the input signal. It was split into two lines, one to the Cluster Finder for a fast trigger decision, the other to the glass TDC system which measured the difference between the time an interaction occurred and the time energy was deposited in a main array block.

At the end of the 400 ns delay line, the delayed signal was sent to the sample-and-hold portion. A signal from the experiment "trigger *OR*" caused the otherwise closed "before" switch to open. The same signal, but delayed by 250 ns, caused the "after" switch to open. As long as all input signals decay with the same time constant  $\tau$ , the voltage difference on the C1 and C2 capacitors should ideally represent the charge in the input pulse caused by the event of interest. But to compensate the slow decay of the integrated signal on capacitor C due to the leakage resistor, a gain slightly greater than

unity multiplied the voltage on C1 before differentiation.

The voltages went through a differential amplifier with its output being sent to the ADC. The ADC module output a 16-bit word for each channel. Its lowest 12 bits were for the differentiated signal, the next three were reserved for the "before" level which represented the charge left from previous events, the highest bit was an indicator of a  $\times 8$  multiplier. The signal was multiplied by 8 before digitization if its value was less than  $1/8$  of the full scale. This effectively raised the sensitivity of the 12-bit ADC to 15-bit for small signals.

Actually, there was only one digitizer in each 16-channel card. The signal had to be held, and the digitization was done sequentially from channel 1 to channel 16.

There were 26 cards for the main array and 8 cards for the active converter. The MA channels occupied 2 CAMAC crates, while the AC channels took up another crate. A charge card controller in each crate read out all the first channels of the cards first, then the second channels, and so on. This enabled the system to read out and digitize at the same time.

The signal from AC blocks were sent to neither the Cluster Finder, nor the TDC.

### 3.7 The Cluster Finder

The square wave from the charge card was input to the Cluster Finder [31] as a central signal to one channel and exported to other channels as one of the neighbor signals of the interconnective (ICON) module, as shown in

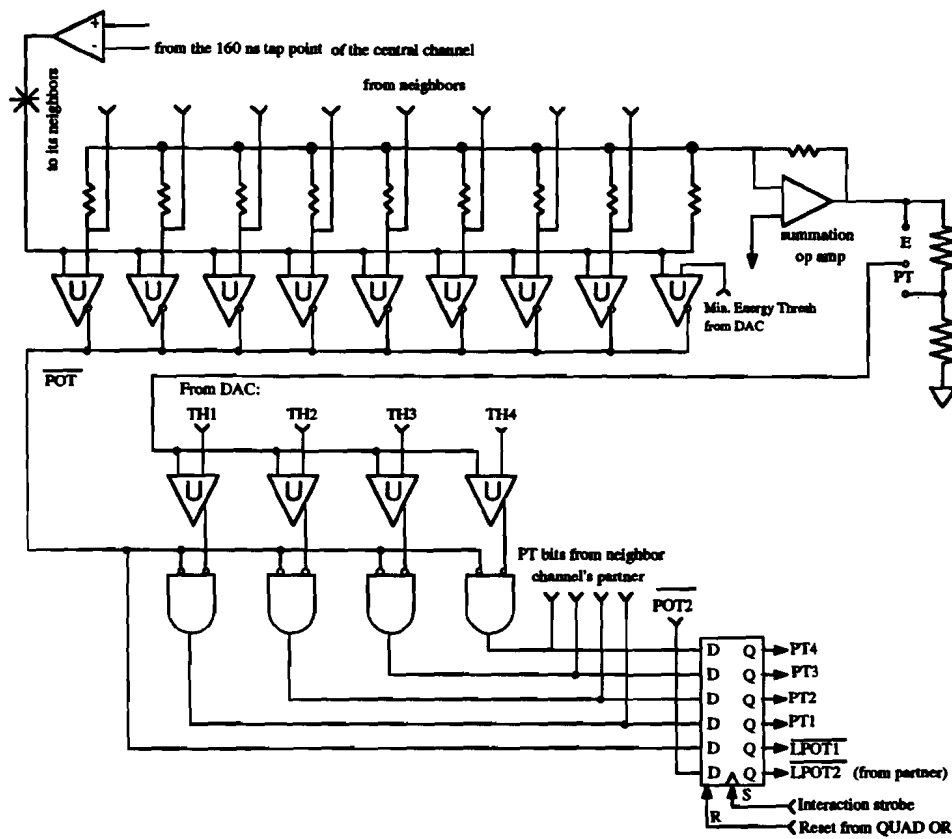


Figure 3.6: The Cluster Finder trigger logic.

Figure 3.6. A block's neighbors were defined as those that shared a common plane ( $x-z$  or  $y-z$ ) or a common line (along  $z$ ) with it in the detector. If the central signal was larger than all of its neighbors and a common minimum energy threshold, the block was then called peak-over-threshold(POT), and a cluster was formed with its energy being the sum of the central block energy and its neighbors' energies. The numbers of blocks in the cluster was usually nine, but could vary from 7 to 10, depending on the geometric boundary

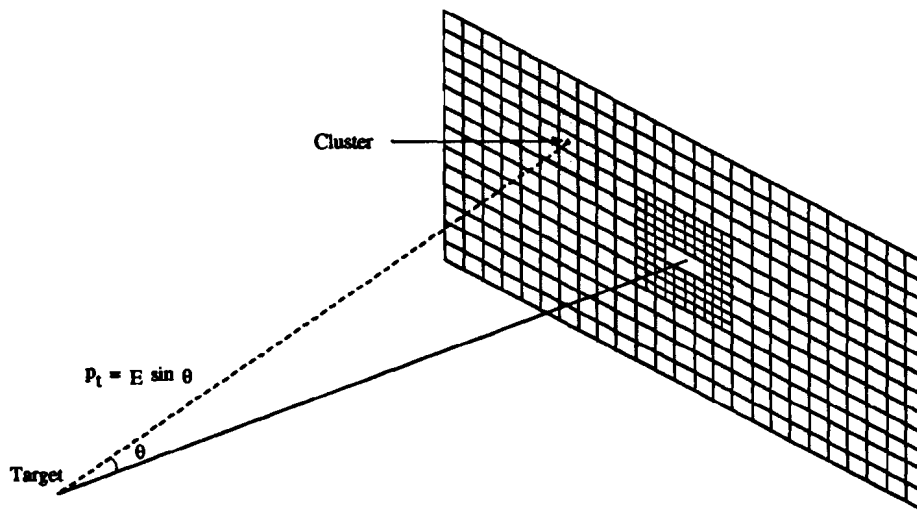


Figure 3.7: Cluster energy to  $p_T$  conversion.

condition. The edge blocks were not used as POT's, but they could serve as neighbors.

The energy sum,  $E$ , was converted to the transverse energy,  $E_T$ , by a voltage divider whose output to input ratio was equal to the  $\sin \theta$  of peak block:

$$E_T = E \sin \theta$$

where  $\theta$  is the angle between the beam direction and the line from center of the target to the center of the POT block as illustrated in Figure 3.7. The ratio of the voltage divider was set to be proportional to  $\sin \theta$ . It was different from channel to channel and depended on the corresponding block position in the detector.

The summed  $p_T$  (the term transverse momentum will be used hereafter

since the particle of interest is a photon for which  $p_T = E_T$ ) signal was compared with four thresholds,  $P_{T1}$ ,  $P_{T2}$ ,  $P_{T3}$ , and  $P_{T4}$ , in a comparator. The four bits resulting from the comparison were set inclusively, *i.e.*, if a high bit was set, all the lower bits would also be set. The result of a logic *OR* of the latched  $p_T$  bits from all of the channels was made available to the experiment trigger selection electronics.

The  $p_T$  thresholds and the minimum energy threshold was set through a digital to analog converter(DAC) by a VME/10 microcomputer. They were adjusted during the run. The most commonly used thresholds were 1.7, 2.5, 3.5, and 4.5 GeV/c for  $P_{T1}$ ,  $P_{T2}$ ,  $P_{T3}$ , and  $P_{T4}$ , respectively, and 1.0 GeV for the energy threshold.

The single  $P_{T1}$  trigger event was not recorded. But if there were two  $P_{T1}$ (or higher) clusters in two opposite quadrants, the event was recorded as a di-photon trigger. The  $P_{T2}$ ,  $P_{T3}$ , and the di-photon triggers were prescaled during the run.

## Chapter 4

# Calibration of the Calorimeter

The electromagnetic calorimeter was calibrated by positioning the table and directing electron beams to each individual block. The gain constants, defined as energy per ADC count, were determined in an off-line procedure to high precision. The on-online calibration took about four hours for each beam energy setting, and was done periodically during the run. The LED pulser was used to track the gains between the calibrations.

### 4.1 Electron Beams

As mentioned in chapter 2, electron beams were produced by inserting a lead plate into the beam line in neutral running mode. The nominal momenta selected for the calibration were 2, 6, 10, 30, 60, and 100 GeV/c. The typical intensity of the electron beam used in the calibration was about 2 kHz, but it could be tuned between 1 kHz and 100 kHz by adjusting the vertical collimators PW7V1/2.

The beam logic used to identify electrons was the same logic as used to

tag the 300 GeV/c pions. Gas pressures in the Cerenkov counters had to be lowered for electrons above 30 GeV to exclude pions.

The momenta of the electron beams could be determined using the beam line magnet parameters, with uncertainty of about 1%. They could also be obtained by turning on PW8 magnets and Rosie to deflect the electrons and using the wire chambers to track them. The deflected electron data were taken before and after each calibration run.

## 4.2 Setting the Gains

The 30 GeV straight-ahead electron beam was used to set the gains on the glass blocks. High voltages on the phototubes were adjusted so that the pulse heights were 100 mV for large blocks, and 85 mV for small blocks, to account for the difference in block size which in turn amounts to the difference in energy deposition. This was to ensure that the analog signals going into the Cluster Finder from similar blocks were the same.

The gain was set when Rosie was off. In the normal data taking mode, the Cluster Finder was operated when Rosie was on. The fringe field of Rosie could change the gain up to 20%. So the gain was also adjusted to account for the difference between Rosie-on and Rosie-off.

The LED was used to make the adjustment. First, the LED pulse heights were recorded for all the blocks with Rosie off. Then turning Rosie on, the high voltage was adjusted so that the LED signals reached the same heights as with Rosie off.

To reduce the effect of any noise coming from the electronic system after the phototube base, to enhance the digitization resolution, the gains on the phototubes should be set high, but not too high to saturate the ADC of 32k counts. The nominal gains for three different Main Array regions were set as:

Block Type	Highest Possible Energy	MeV/ ADC count
Small SCG1-C	250 GeV	8.3
Large SCG1-C	150 GeV	5.0
SF5	100 GeV	3.3

The gains on the active converters were set in a similar way to those on the main array blocks.

### 4.3 On-line Calibration Sequence

The on-line calibration procedure was controlled by a VME/10 computer. In a normal sequence, the table was moved to position the large blocks to the beam first, then the small blocks, one at a time. In the active converter region, the beam was positioned to the  $x$ -center of alternating AC blocks, *i.e.*, odd number (counting from left to right) active converter columns were used when the beam was centered on the odd number (counting from bottom to top) main array rows, and even number AC columns were used when the beam was on the even number MA rows. So each active converter would get hit at three different  $y$  positions, excluding the hit at  $y = 0$ . The light attenuation in AC blocks could be determined from those points. In other

regions, the beam was centered on the target main array blocks. In all cases, the  $y$  position of the beam was always at the center of the MA blocks.

During the calibration, the table would not move until the number of electrons hitting the target main array block reached 1000. The data acquisition system could record that many events in three seconds. It was possible to calibrate more than one block per 23-second spill, since the motion from one large block to another took 15 seconds. Most calibrations were done in the multi-block per spill mode. It normally took a little less than four hours to perform a complete calibration of the calorimeter at one energy.

The calibration was done in an interval of about a month. The 30 GeV beam was used each time, and other energies were used less frequently. There were only two complete calibration sequences that used all six beam momenta.

#### 4.4 The Off-line Procedure

The purpose of calibrating the calorimeter was to determine the precise conversion factor from ADC counts to energy deposited in each block. If the calorimeter had been a single giant glass block, then the conversion factor would simply be the known beam energy divided by the mean ADC counts. But because of the finite glass block size and the way the electron beam was positioned, the electron energy was not deposited in a single block. It was necessary to have a more complicated program to handle the task.

#### 4.4.1 Data Reduction

Not all the words recorded on the calibration data tape were useful for the off-line calibration. Some words, like those for the glass blocks far away from the target block, could be discarded. Other words, like the beam station information, could be compressed. A program, *REDUCE*, was written to compress the calibration data by a factor of eight.

The reduced file contained the information about beam, the glass blocks near the target block, and the LGC and/or GTH channels above some thresholds.

Beam tracking subroutines were used to find the beam track(s) in the three beam stations. The number of tracks were written to the file. If there was one, and only one track, the  $(x, y)$  position of the track pointing to the front face of the main array was also recorded.

The raw ADC counts of the target block and the next two surrounding layers of blocks were copied to the file. This area of 5-blocks by 5-blocks was always sufficiently large to contain the shower, despite the possible beam spread in  $x$ - $y$  plane.

The LeCroy 2280 output for the GTH and LGC was further sparcified in the reduction program. Only those channels with ADC counts above certain software cut-off parameters and the edge tubes were put into the reduced file. The edge size (ref. Section 3.6.1) was set to three for all hodoscope planes. The thresholds varied for different hodoscope regions at different calibration energies, and they are listed in table 4.1.

*Table 4.1: Software Thresholds of the Four Hodoscope Planes*

Energy (GeV/c)	LGC- $x$	LGC- $y$	GTH- $x$	GTH- $y$
2	50	50	100	200
6	50	50	200	400
10	100	100	200	400
30	100	100	400	800
60	150	150	600	1200
100	200	200	800	1600

#### 4.4.2 GTH and LGC Gains

Since the LGC  $x$  planes were divided into four quadrants, and each quadrant was driven by a power supply, there were four gains for the  $x$  planes, and there were also four corresponding  $y$  plane gains. The LGC plane gain was the conversion factor from ADC to energy, like the glass gain.

There were also plane gains for the GTH. But since little energy was deposited in the GTH, those gains had only relative meanings for  $x$ - $y$  match-ups.

Before the plane gains could be determined, the fluctuations of different tube channels in each plane had to be smoothed out. This procedure did not use the calibration data; instead, it used data taken under normal running conditions.

The GTH  $x$ -east plane tube by tube correction will be used as an example to describe it. Figure 4.1 shows a profile of the plane after accumulating 30,000 events of normal data. The horizontal axis is the tube number, and

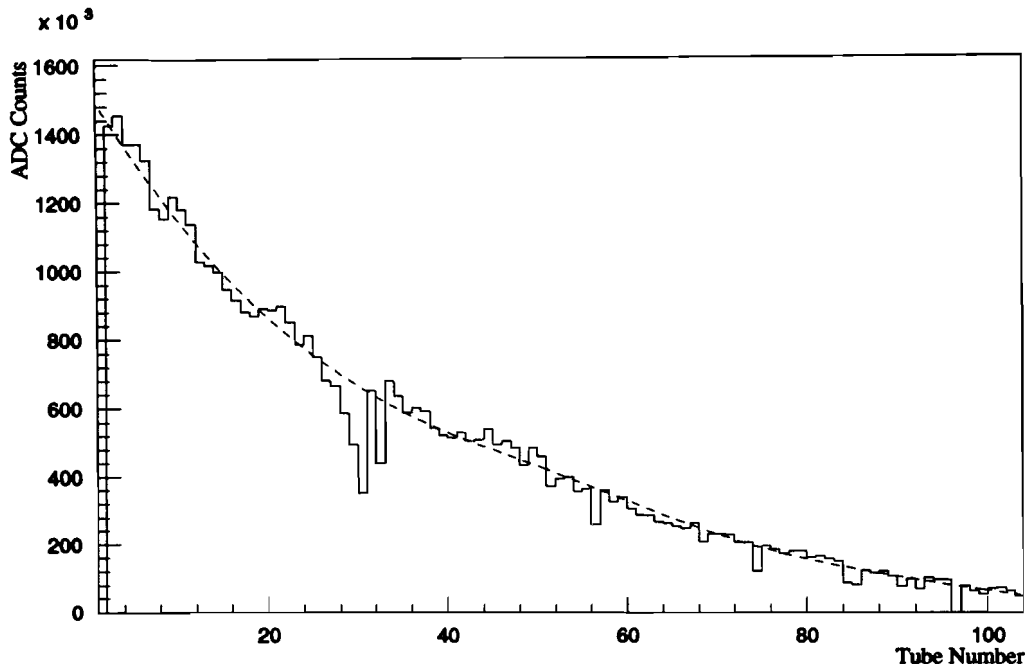


*Figure 4.1: GTH x-east ADC profile. The dashed line is the spline fit.*

the vertical axis is the summed ADC counts. The first tube is closest to the beam, so it is most probable to get hit. The farther a tube is away from beam, the less probable it will get hit. The profile, then, should show a smooth decay from the first tube to the last tube. But fluctuations from tube to tube, due to the tubes themselves and the associated electronics, are evident in the plot.

A spline fit was used to smooth out the fluctuations. The ratio of the fitted value and the raw ADC sum was calculated for each channel, and was stored in a parameter file as the tube gain (inverse gain, actually). The same (gain corrected) ADC counts from different tubes in one plane should

represent the same amount of charges on the wires.

The same was done for all of the GTH and LGC planes. This procedure was repeated whenever there was any change in any of the planes. The tube gains were stored in the corresponding parameter files. From here on, the GTH and LGC ADC counts will mean the tube-gain-corrected ones, unless otherwise stated explicitly.

So far, only the fluctuations within a plane were corrected. The differences among the planes, due to the power supplies and the 2280 crates, was corrected as follows.

For the GTH planes, the gains in the two  $x$  views were not very different, and it was not necessary to have them the same. The only importance was to have the ADC counts from the  $x$  view and  $y$  view in the same GTH wing representing the same charge. So the  $y$  plane gains were set to 1 and the  $x$  plane gains were adjusted to match the  $y$  gains.

The 30 GeV calibration data was used to determine these GTH gains. Figure 4.2 shows the ADC distribution of the electron events for  $x$ -east view. Its mean and sigma were computed. A second iteration was done to discard the events three sigmas away from the mean. The ratio between the new mean of the  $x$  view and that of the  $y$  view was considered as the  $x$  view plane gain. The same was true for the west wing.

The situation for the LGC was a little more complicated. First, the LGC plane gains were the conversion factors from ADC counts to energies. They had absolute meanings. Secondly, ADC counts in the  $y$  views had an  $x$ -

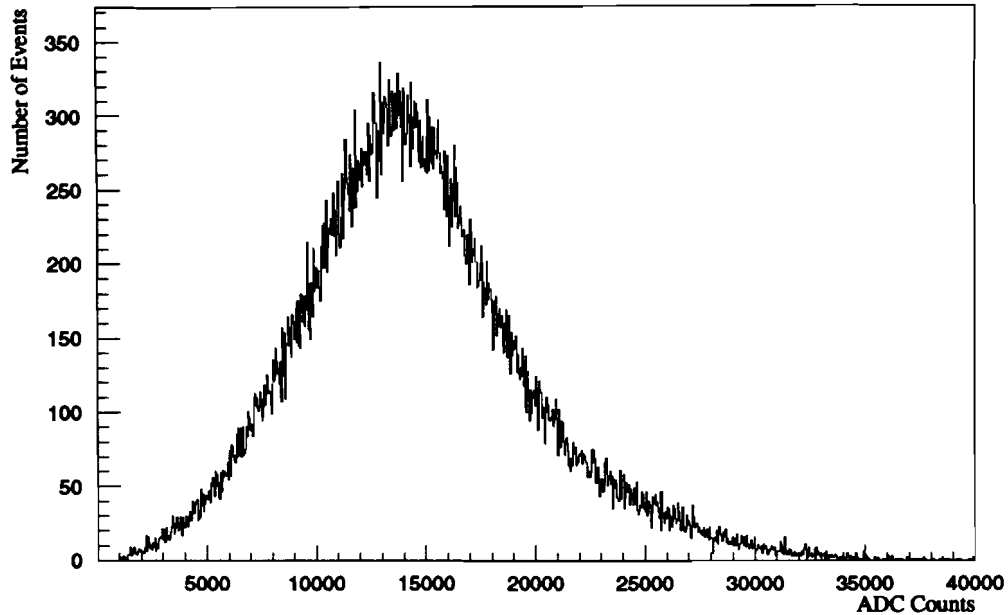


*Figure 4.2: ADC distribution of the GTH x-east view*

position dependence, even after the tube to tube correction. This dependence was caused by tightening the bolts at the LGC edges which held the device together, resulting in a bowed plane and different capacitance at different positions.

Figure 4.3 is an example of the  $x$  dependence. The points are the average ADC counts (in arbitrary scale) in the  $y$  view, when the 30 GeV beam hits the device along the same  $y$ , but at seven different  $x$  positions. A parabolic curve was fit through the points, and the inverse of the curve was applied to the ADC counts to correct for the dependence. The  $x$ -dependence had a slight  $y$  position dependence too, so that the  $x$ -dependence had to be

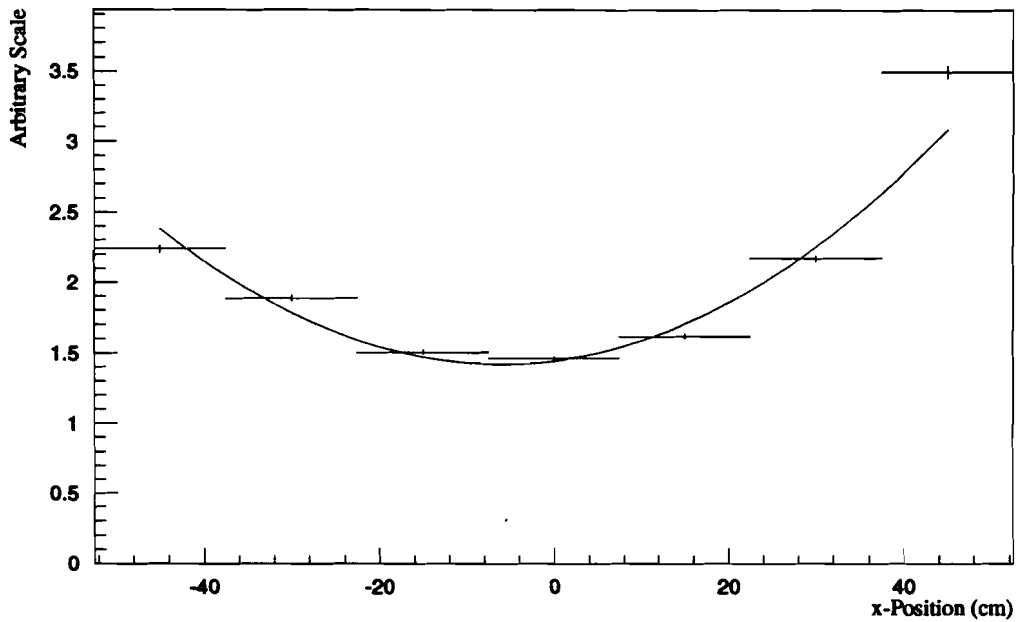


*Figure 4.3: A typical  $x$ -position dependence of the LGC  $y$ -view energy. The curve is a quadratic fit*

corrected in different  $y$  intervals. There were 18 such curves, representing 18  $y$  intervals.

Mean ADC values were calculated for all eight planes of the LGC, after those corrections. The ratios of an EGS predicted energy deposition of 3.0 GeV in the LGC to those means represented the ADC to energy conversion factors, thus were the LGC plane gains.

#### 4.4.3 Glass Gains

The LGC gains were used in the overall off-line calibration of the electromagnetic calorimeter. The calibration program performed a  $\chi^2$  minimization

about the target glass blocks. Correction due to light attenuation effects were also made in the same program.

The long dimension of the active converter was along the  $y$ -axis. Light produced by showers would attenuate before it reached the phototube at the end of each AC block. The attenuation was formulated in a  $y$ -dependent form

$$E_{AC}(y) = G_{AC}(y + D)^c P(y) \quad (4.1)$$

where  $y$  is the distance between the beam and the phototube,  $D$  is a parameter fixed at 10 cm,  $G_{AC}$  is the gain constant of the active converter,  $c$  is the power of the attenuation curve, and  $P$  is the measured ADC counts.

From the on-line calibration sequence, each active converter block was exposed to the beam at least at three  $y$  positions. The average energy,  $E_{AC}$ , deposited in the active converter should be independent of the position of the beam, at one beam momentum. An EGS predicted energy deposition of  $\langle E_{AC} \rangle = 4.34$  GeV in the active converter by 30 GeV/c electrons was used in a fit to determine the gain constant and the power. A  $\chi^2$  was formed

$$\chi^2 = \sum_{i=1}^{i=3} \{ \log \langle E_{AC} \rangle - [\log G_{AC} + c \times \log(y_i + D) + \log P(y_i)] \}^2, \quad (4.2)$$

the term in square brackets is just the logarithm of the right side of Equation 4.1. Three  $y_i$  beam positions were used in the fit, the fourth position at  $y = 0$  was not used because the electron could deposit its energy in both the top row and bottom row converters.

The longitudinal light attenuation in the main array blocks is evident in

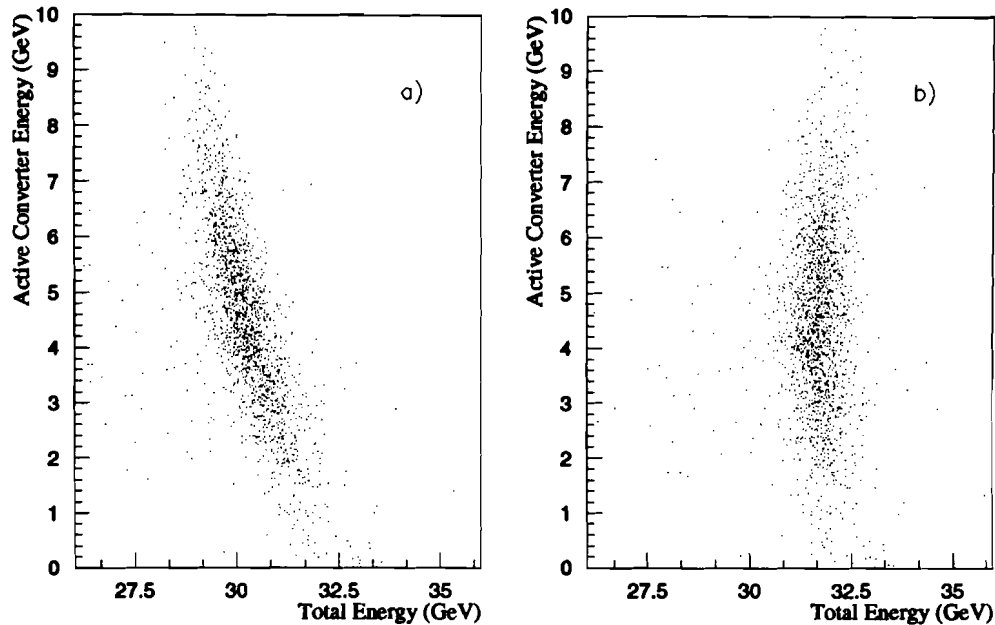


*Figure 4.4: Effect of longitudinal light attenuation in main array. Plotted quantities are the measured active converter energy versus the total shower energy. a): without correction; b): with correction*

Figure 4.4(a), showing the correlation between the measured AC energy and the measured total energy (AC energy + MA energy) for 30 GeV showers in the SF5 block region. It was clear that the more the energy deposited in the AC was (which meant the shower started earlier), the smaller the total apparent energy was. For all 30 GeV showers, the total light produced in the glass (AC and MA) should be about the same, without counting a small amount shower leakage out of the rear end of the calorimeter. But if a shower starts early, more light will be subject to absorption in the main array as it travels towards the phototube which will then detect less light.

So the apparent energy measured by the glass-phototube system will be less than the real energy deposited in the main array, leading to the correlation shown on the plot. From the linearity of the correlation, a linear correction to the total energy could be made by just multiplying the AC energy by a parameter greater than unity.

This longitudinal light attenuation was parameterized in terms of a  $z$  dependence, the actual energy was expressed as

$$E_T = E_{MA}(1 + b_m/z) + E_{AC}, \quad (4.3)$$

where  $z$  is the mean shower depth,  $m$  denotes the target block number, and  $E_{MA}$  and  $E_{AC}$  are the measured main array energy and active converter energy, respectively. Empirically, the depth was represented by  $E_{MA}/E_{AC}$ . The above formula then becomes

$$E_T = E_{MA} + (1 + b_m)E_{AC}. \quad (4.4)$$

It could be further reduced, by replacing  $(1 + b_m)$  by  $f_m$ , to

$$E_T = E_{MA} + f_m E_{AC}, \quad (4.5)$$

as required by Figure 4.4. So the effect of light attenuation in the main array can be corrected numerically in terms of the active converter energy. The same was true for the LGC region.

The last formula can be expanded in terms of the target block energy and the neighboring block energies,

$$E_T = G_m P_m + \sum_{n=1}^N E_n + f_m [G_a (y + D)^c P_a + G_b (y + D)^c P_b + \sum_{i=1}^I E_i + \sum_{j=1}^J E_j], \quad (4.6)$$

where the first term is the energy of the target main array block energy, the second term is the sum of  $N$  (nominally eight) neighboring main array block energies, and the first two terms in the brackets are the target front and back converter energies. The last two terms, the energies of the neighboring front and back active converters, are small, since the beam is positioned at the center of the target AC blocks. The number of front converters,  $I$ , and the number of back converters,  $J$ , were equal to two (counting one neighboring block on each side) in most cases, but were equal to four when the beam was positioned at  $y = 0$ , to count neighboring blocks in both top and bottom rows.

In the fit, the  $\chi^2$

$$\chi^2 = \sum_{k=1}^{N_{events}} (E_{Beam} - E_T)^2 \quad (4.7)$$

was minimized, where  $E_T$  is the measured total energy. By absorbing the factors in front of  $P_a$  and  $P_b$  and neglecting a very small contribution of the neighboring AC blocks to the correction of the longitudinal light attenuation in Equation 4.6, the total energy can be expressed as

$$E_T = G_m P_m + \sum_{n=1}^N E_n + H_a P_a + H_b P_b + \sum_{i=1}^I E_i + \sum_{j=1}^J E_j, \quad (4.8)$$

where the unknowns are the target block gains (main array,  $G_m$ ; front converter,  $H_a$ ; back converter,  $H_b$ ). The energies,  $E_n$ ,  $E_i$ , and  $E_j$ , of the neighboring blocks were treated as known in the fit by taking gains from the previous iteration. The number of independent gain factors to be determined depends on the location of the main array block. The following is a

list of all the possible combinations:

1.  $G_m$  on the outer columns of main array blocks with nothing in front;
2.  $G_m$ ,  $H_a$ , and  $H_b$  in the active converter area where  $y$  is not near zero;
3.  $G_m$ ,  $H_{a1}$ ,  $H_{a2}$ ,  $H_{b1}$ , and  $H_{b2}$  in the active converter area near  $y = 0$ ;
4.  $G_m$ ,  $H_l$  for a given quadrant of the  $x$ -plane of the LGC.

It is clear that this procedure could yield up to four different  $H$  gains for each AC block and many different  $H$  gains for each LGC quadrant. These  $H$  gains reflected the differences in main array blocks absorbing the light, since the absolute gain for each active converter should be independent of beam position, and was already determined using Equation 4.1. The  $H$  gains were used to determine the  $z$  factor for each main array block, by comparing Equations 4.6 and 4.8 for the active converter regions (for case 2 listed above),

$$f_m = \frac{H_a P_a + \sum_{i=1}^I E_i + H_b P_b + \sum_{j=1}^J E_j}{G_a (y + D)^c P_a + G_b (y + D)^c P_b + \sum_{i=1}^I E_i + \sum_{j=1}^J E_j}. \quad (4.9)$$

In the LGC region where  $H_a$  and  $H_b$  coalesce into  $H_l$  and the energy sums over active converter block  $i$  and  $j$  are non-existent, the  $z$  factor is simply the ratio of  $H_l$  and the plane gain  $G_{LGC}$

$$f_m = H_l / G_{LGC} \quad (4.10)$$

where  $m$  denotes the main array block number.

To determine the total energy in a shower centered on block  $m$ , one uses the equation

$$E_T = f_m E_{AC} + \sum_{n=1}^N G_n P_n \quad (4.11)$$

where  $n$  counts (nominally) nine blocks of the main array shower centered on block  $m$ . When evaluating Eq.(4.11) during the analysis of data where showers were not block centered as in calibration, an energy weighted average  $f_m$  given by

$$\langle f \rangle = \frac{\sum_{n=1}^N f_n E_n^2}{\sum_{n=1}^N E_n^2} \quad (4.12)$$

was used. This was most important for cases where a shower divided its energy fairly evenly over several blocks.

## 4.5 Energy Dependence

The procedure just described was performed for each of the 30 GeV calibration runs taken in monthly intervals. The gain constants,  $z$  factors, and  $y$  attenuation powers were stored in parameter files labeled by the data tape numbers. But those parameters did not necessarily optimize the energy distribution at other energies. It was discovered that the absolute gain of each block had a small energy dependence. This dependence was corrected by the following procedure.

It was assumed that all gain constants determined at 30 GeV correctly represent the relative gains among main array blocks. The energy dependence was then represented by two additional parameters,  $\alpha$  and  $\beta$ , in the

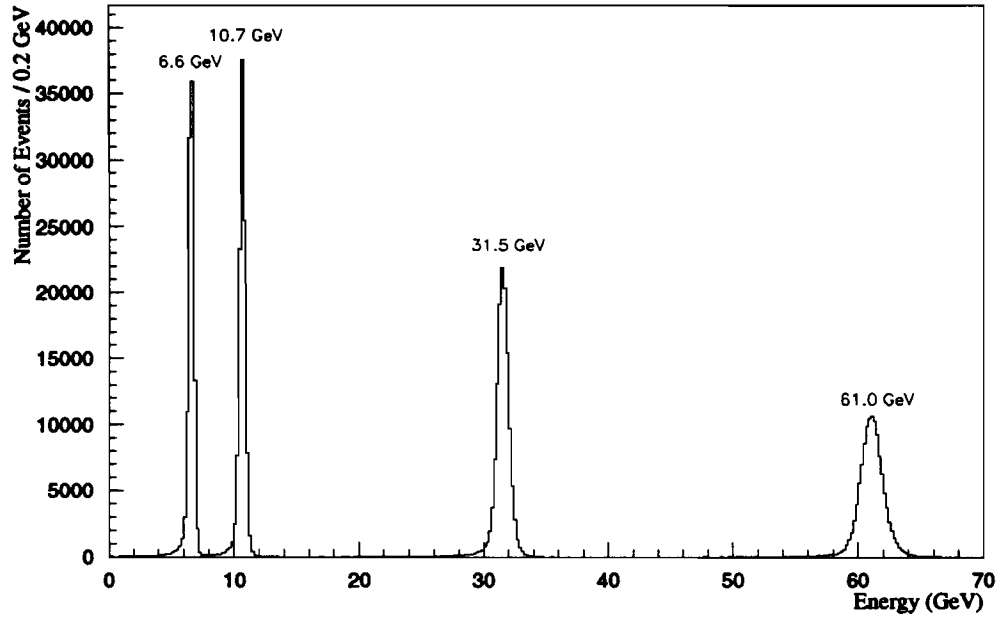


*Figure 4.5: Reconstructed calibration electron energies. The numbers are the best estimates of the beam energies.*

total energy calculation:

$$E_T = \alpha_m f_m E_{AC} + \beta_m E_{MA} \quad (4.13)$$

where  $E_{AC}$  is the active converter (or LGC) energy and  $E_{MA}$  is the main array energy. Both of these energies were obtained using the 30 GeV calibration gain constants. The  $\alpha$  and  $\beta$  parameters were determined by minimizing the total energy distribution using a least-square-fit for each calibration energy. Five  $\alpha_m$  and  $\beta_m$  parameters, corresponding 6, 10, 30, 60, and 100 GeV calibrations, were extracted for each main array block. These numbers vary slowly with energy and are unity at 30 GeV.

*Table 4.2: Energy Resolutions in Various Regions*

	6 GeV	10 GeV	30 GeV	60 GeV
Small SCG	$5.91 \pm 0.21$	$4.71 \pm 0.14$	$3.26 \pm 0.12$	$2.97 \pm 0.06$
Large SCG/LGC	$4.83 \pm 0.21$	$3.68 \pm 0.12$	$2.37 \pm 0.10$	$2.04 \pm 0.07$
Large SCG/AC	$2.98 \pm 0.11$	$2.19 \pm 0.08$	$1.53 \pm 0.08$	$1.20 \pm 0.06$
SF5	$2.87 \pm 0.08$	$1.98 \pm 0.05$	$1.26 \pm 0.05$	$1.03 \pm 0.04$

In data analysis, the shower energy was first estimated using Eq.(4.11). The  $\alpha$  and  $\beta$  parameters at that energy were determined by interpolating the  $\alpha$  and  $\beta$  from the two adjacent calibration energies. The total energy of the shower is determined from Eq.(4.13), with energy weighted averages of  $f$ ,  $\alpha$ , and  $\beta$ .

## 4.6 Energy Resolutions

Figure 4.5 shows the reconstructed energy distributions for nominal 6, 10, 30, and 60 GeV electrons in the SF5 region. The best estimates of the beam energies from the reconstructed  $\pi^0$  and  $\eta$  invariant mass in our data are written on the plot. A Gaussian fit was used to determine the  $\sigma$  for each distribution. Energy resolutions ( $\sigma/E$ ) are listed in Table 4.2 for different regions, after a 1% beam momentum uncertainty was subtracted in quadrature. The numbers are plotted in Figure 4.6 with their fits to

$$\frac{\sigma}{E} = a + \frac{b}{\sqrt{E}} \quad (4.14)$$

superimposed. The parameters,  $a$  and  $b$ , are listed in Table 4.3

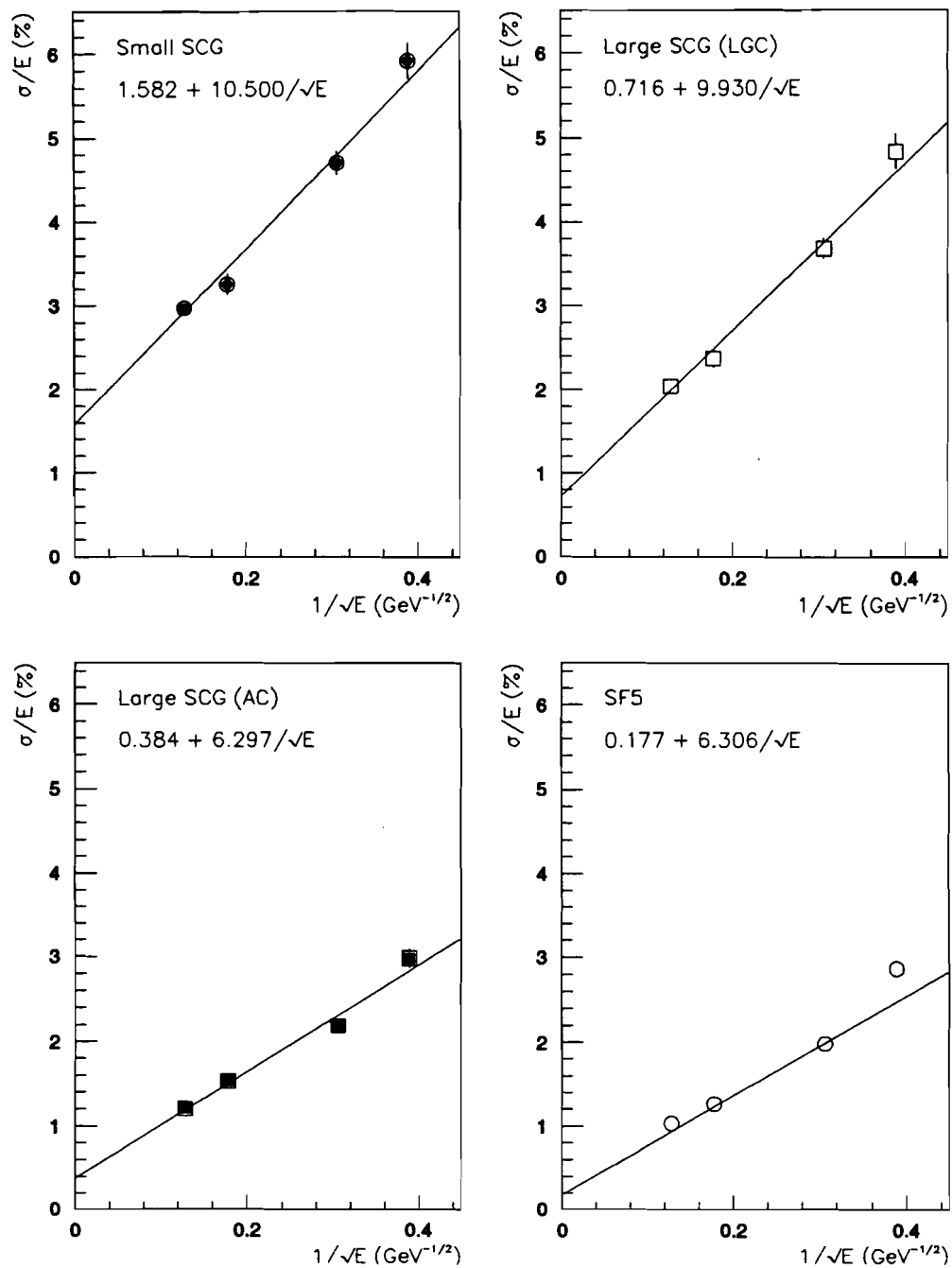


Figure 4.6: Energy resolutions of four regions. The curves are straight line fits whose parameters written on the plots

Table 4.3: The  $a$ ,  $b$  Parameters of Various Regions

	$a$	$b$
Small SCG	$1.582 \pm 0.118$	$10.500 \pm 0.628$
Large SCG/LGC	$0.716 \pm 0.125$	$9.930 \pm 0.616$
Large SCG/AC	$0.384 \pm 0.094$	$6.297 \pm 0.404$
SF5	$0.177 \pm 0.063$	$6.306 \pm 0.274$

## 4.7 Glass Gain Monitoring and Correction

The glass gain was tracked by the LED pulser. During the normal data-taking run and the electron calibrations, pulser trigger events were taken between beam spills, and the LED pulse height was read out for each glass block.

During the 30 GeV calibration, the ADC value of each glass channel was recorded as the pedestal of the channel when the LED filter wheel was at position 1. The LED pulse height at filter wheel position 12 was recorded and stored in the gain parameter file. A special kind of parameter file, known as Q file, was used to record the LED pulse height of filter wheel position 12 at different times during the normal run. A *reference* Q file containing pulse heights from all glass channels was produced after each calibration. Subsequent Q files were created for every 11 minutes of running, the time it took for the LED filter wheel to complete a cycle. Those files only contained data for channels whose pulse height changed more than 0.5% with respect to the reference Q file, which was produced whenever a major change occurred

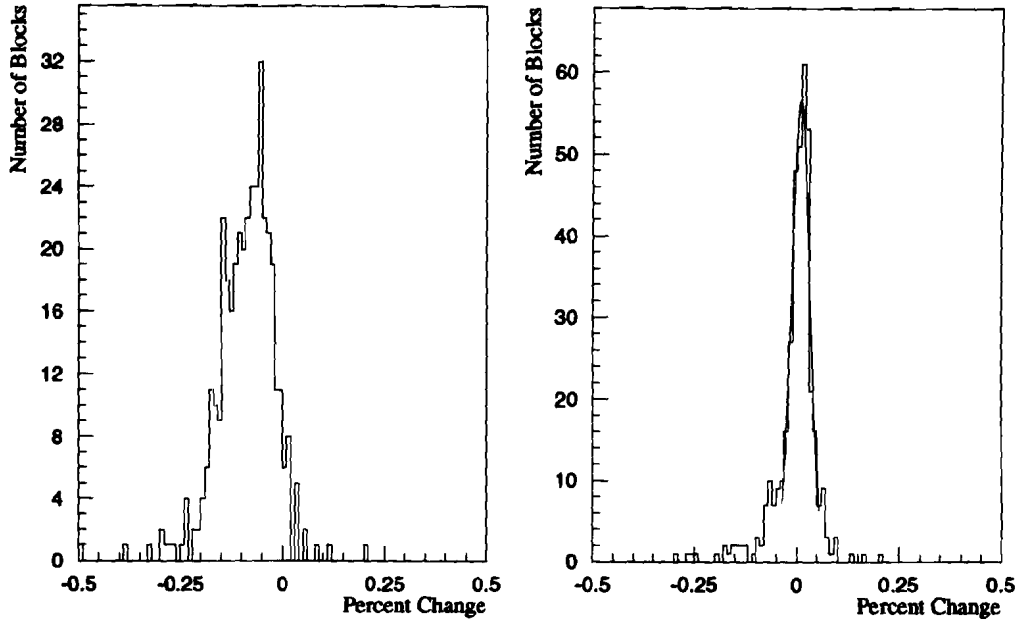


Figure 4.7: Percent changes of the main array block gains in six months. a): no correction; b): with LED correction

during the run (e.g. Rosie polarity, power outage, high voltage adjustment to the phototubes).

The light output from the LED was further monitored by three PIN diodes. The gain constant at any time  $t$  could be calculated as following:

$$G_t = G_{cal} \times \frac{PH_{cal}^{LED} \times PH_t^{PIN}}{PH_t^{LED} \times PH_{cal}^{PIN}}, \quad (4.15)$$

where  $PH$  stands for pulse height, and  $cal$  refers to calibration time.

Figure 4.7 shows the difference in gain constants from two calibrations six months apart. The left plot is the difference without any correction. It can be seen that some channels changed as much as 20% over the period.

This was caused by voltage adjustments made during the run and phototube gain drifting. After applying the LED-PIN correction, the right graph shows the constants agreed quite well. A Gaussian fit to its central bins indicated that the average change was 0.9%, with a  $\sigma$  of 2.2%. This indicated that the correction was working properly and tracked the gains well.

## Chapter 5

# The Shower Position Measurement

The measurement of  $\pi^0$  and  $\eta$  production requires a detector with a very good position resolution in order to resolve two nearby photons. This feature is particularly important for reconstructing  $\pi^0$  mesons, because of their small mass.

Suppose a  $\pi^0$  of energy  $E$  decays into two photons of energies  $E_1$  and  $E_2$ , the mass square of the  $\pi^0$  is then

$$m^2 = 4E_1E_2 \sin^2 \frac{\theta}{2}, \quad (5.1)$$

where  $\theta$  is the opening angle of the two photons. To show the effect of measurement error in  $\theta$  on the mass, a small angle approximation is used here, with the result

$$m^2 = E_1E_2 \theta^2. \quad (5.2)$$

The percent error on the mass is

$$\frac{\Delta m}{m} = \frac{1}{2} \sqrt{\left(\frac{\Delta E_1}{E_1}\right)^2 + \left(\frac{\Delta E_2}{E_2}\right)^2 + 4\left(\frac{\Delta \theta}{\theta}\right)^2} \quad (5.3)$$

This indicates that the position resolution affects the width of the invariant mass distribution more than the energy resolution does.

It can be shown that the opening angle in the laboratory for photons from high  $p_T$   $\pi^0$  and  $\eta$  is generally small. The energy asymmetry of the photons is defined as

$$x = |E_1 - E_2|/(E_1 + E_2). \quad (5.4)$$

Equation 5.1 becomes

$$m^2 = E^2 (1 - x^2) \sin^2 \frac{\theta}{2}. \quad (5.5)$$

Using the small angle approximation again, the opening angle is then

$$\theta = \frac{2m}{E\sqrt{1-x^2}}. \quad (5.6)$$

This angle reaches its minimum in a symmetric decay (two photons with the same energy). A typical high  $p_T$   $\pi^0$  in the LGC region has an energy of about 90 GeV, and has a minimum opening angle,  $\theta_{min} = 2m/E$ , of 3 mrad corresponding to photon separation of 3 cm.

Since the  $\pi^0$  and  $\eta$  are pseudoscalars, they decay isotropically in their rest frame. This leads to a flat distribution of asymmetry  $x$ , ranging from 0 to 1. From Equation 5.6, it can be shown that about 94% of the meson decays will have opening angles smaller than  $3\theta_{min}$ . This makes a detector with excellent shower separation ability a must.

The position resolution also has a great effect on the differential cross section of  $\pi^0$  production. The cross section of the high  $p_T$   $\pi^0$  production

falls off very quickly with increasing  $p_T$ . From the theoretical predictions and earlier experimental measurements, the cross section's  $p_T$  dependence is roughly of  $p_T^{-9.5}$ , where  $p_T$  is measured in GeV. The  $p_T$  can be calculated in terms of energy  $E$  and position of the particle

$$p_T = E r/R, \quad (5.7)$$

where  $r$  is the distance between the  $\pi^0$  and the center of the calorimeter, and  $R$  is the distance between the  $\pi^0$  and the target. A 1% error in  $r$  would result in 1% error in  $p_T$ , leading to a 9.5% error in the differential cross section.

A deconvolution technique used in the analysis to search for electromagnetic showers and determine their positions will be described in the following section. Subsequent results, including position resolutions, from a study of calibration electrons will be presented.

## 5.1 The Deconvolution Method

A deconvolution technique [32] was used to find showers in the hodoscopes and determine their positions as well as their energies. The technique is basically to determine the Fourier transform of the input signal, divide it by an expected shower shape in the frequency space, and transform it back to the position space, then extract the peaks out of the signal.

Suppose a signal is composed of several showers with the same shape, but different integrated area of  $A_i$  at different positions  $x_i$ . If the normalized

shower shape is  $p(x)$ , then the signal at a given position  $x$  can be expressed as

$$s(x) = \sum A_i p(x - x_i). \quad (5.8)$$

Its Fourier transform is simply

$$D(\omega) = \sum A_i \int_{-\infty}^{+\infty} p(x - x_i) e^{-j\omega x} dx. \quad (5.9)$$

With the shift theorem, it becomes

$$D(\omega) = \sum_i A_i e^{-j\omega x_i} \int_{-\infty}^{+\infty} p(x) e^{-j\omega x} dx. \quad (5.10)$$

If the Fourier transform of the shower shape is

$$P(\omega) = \int_{-\infty}^{+\infty} p(x) e^{-j\omega x} dx, \quad (5.11)$$

then we can form

$$\frac{D(\omega)}{P(\omega)} = A(\omega) = \sum_i A_i e^{-j\omega x_i}. \quad (5.12)$$

The inverse transformation of  $A(\omega)$  is

$$a(x) = \frac{1}{2\pi} \int_{-\infty}^{+\infty} \sum_i A_i e^{-j\omega x_i} e^{j\omega x} dx. \quad (5.13)$$

which reduces to

$$a(x) = \frac{1}{2\pi} \sum_i A_i \delta(x - x_i). \quad (5.14)$$

Scanning across the signal in  $x$ , it is clear that  $a(x)$  takes the value of the area of the the shower,  $A_i$ , at the shower center  $x_i$ , apart from the factor of  $1/2\pi$ .  $a(x)$  is zero elsewhere. So, if the shower shape,  $p(x)$ , is precisely

*Table 5.1: Widths of Symmetric Showers (cm)*

LGC $x$	LGC $y$	GTH $x$ -single	GTH $y$	GTH $x$ -double
0.3	0.4	0.9	1.3	1.2

known and the bin size in  $x$  is infinitesimal, the deconvolution method can find the showers and determine their energies and positions very well.

But the information available in the analysis was in a discrete domain, and the bin (tube or strip) size was finite. Some corrections were needed based on a study of calibration electron data, in order to get the right shower energy (the area) and the right position.

## 5.2 Shower Widths

To use the deconvolution method, it is necessary to have an assumed pulse shape close to the real shower shape in the hodoscopes. Since the showers of interest were electromagnetic ones, the shape used in the analysis was extracted from the electron calibration data.

In the calibration data, each event had only one shower. The peak of the shower was defined as a tube (or strip) with the largest pulse height above a certain threshold. If the sum of the pulse heights from two neighboring tubes at each side of the peak tube were equal within 10%, then the shower was called a symmetric shower. Fifteen bins (seven on each side of the peak) were used to obtain the normalized shapes of these symmetric showers. The

shapes are shown in Figure 5.1 for different hodoscope planes. The error bar on each point is statistical. The shapes were parameterized by a functional form

$$p(x) = Ae^{-|x-x_i|/\sigma}, \quad (5.15)$$

where  $\sigma$  is defined as the width of the shape, and  $x_i$  is the location of the shower center. The widths of the symmetric showers in different regions are listed in Table 5.1. These shapes are used in the analysis.

The symmetric shower was found to be the narrowest, while the average shower shape was a little bit broader. The symmetric shower shape was chosen to avoid high frequency ringing in the Fourier transformed space.

Further study showed that, within the statistical errors, the average shower shape did not depend significantly on the incident energy (10 to 100 GeV) as can be seen in Figure 5.2, nor did it depend on the energy deposition in the hodoscope for one incident energy.

### 5.3 The Position and Energy Determination Using Deconvolution

The deconvolution technique used in our software works for a spectrum with  $2^N$  points, with its last  $2 \times N_F + 1$  elements reserved for the known pulse shape. In our case,  $N_F$  was equal to seven, and  $N$  varied from five to be six depending on the length of the input signal.

The computing time used in the deconvolution depends mostly on  $N$ . For a fixed  $N$ , it is rational to take the maximum possible number of bins

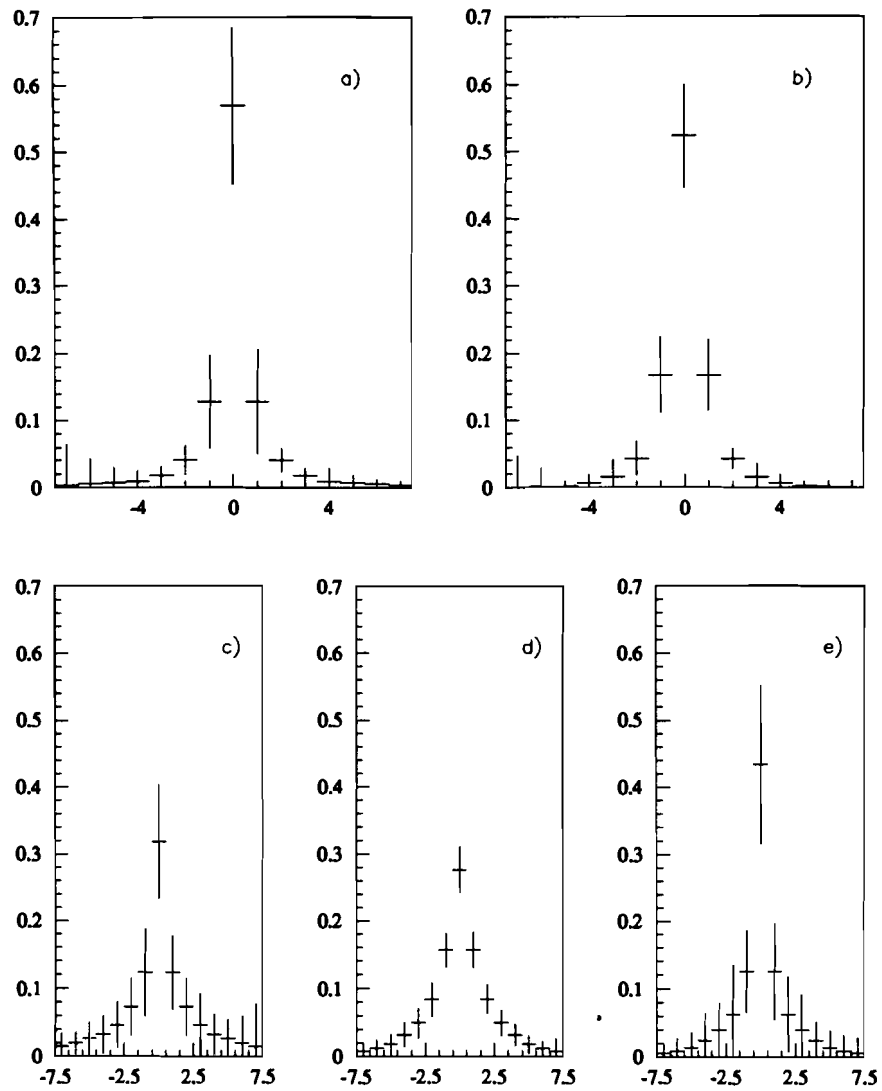


*Figure 5.1: Hodoscope shower shapes normalized to 1. Horizontal axes are in units of tube widths. a): LGC x-view; b): LGC y-view; c): GTH x-view single tube region; d): GTH y-view; e): GTH x-view double tube region.*

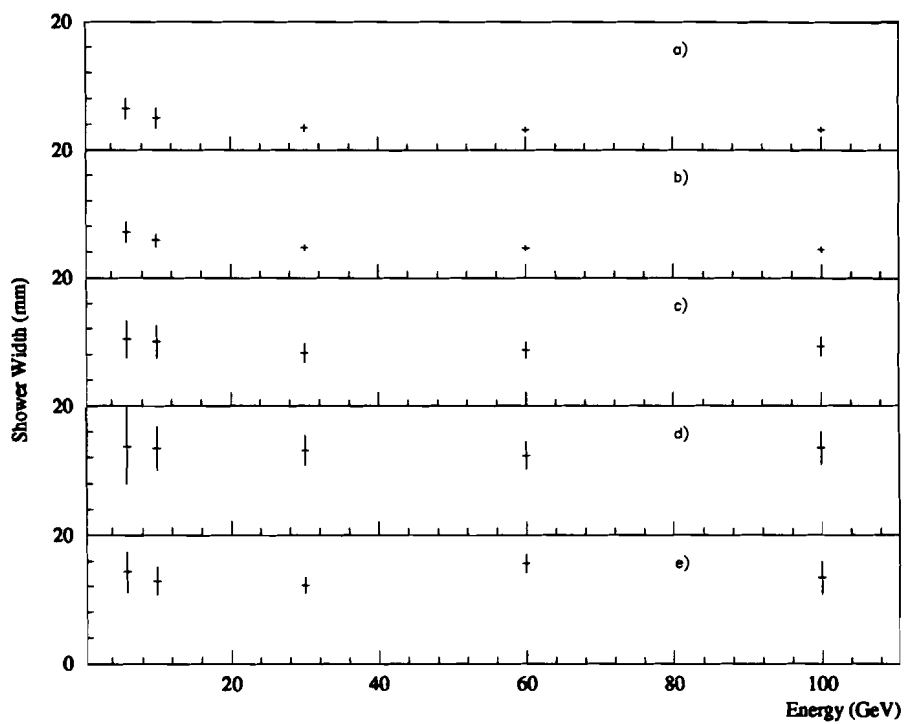


Figure 5.2: Hodoscope shower width as function of energy. a): LGC x-view; b): LGC y-view; c): GTH x-view single tube region; d): GTH y-view; e): GTH x-view double tube region.

for a signal, since the longer the input signal is, the less the edge effect will be.

In the analysis, a peak searching subroutine opened up a window in the hodoscope based on the information from either the main array (in case of the normal data) or the beam (in case of calibration events). If the window covered less than 49, but more than 13 tubes, the window was then expanded to cover 49 tubes if possible (it may not be possible when the window is at the edges of the hodoscopes). But only the peaks found inside the original window would be returned by the subroutine. On the other hand, if there were more than 49 tubes in the window, tubes at each edge were cut, only 49 tubes in the center were kept. The two edge tubes on each side of the 49-tube signal were not allowed to be peaks because of the possible ringing at the ends of the deconvoluted spectrum, but they were used as neighbors in position and energy determination procedure. If the input signal was less than 13 tubes long,  $N$  was chosen to be equal to five to save time, and the working space was 17 tubes long.

In reality, there were fluctuations in the shower development and noise in the electronic system causing the shower shape to differ from the "known" shape. The deconvoluted spectrum  $a(x)$  would not be like what Equation 5.14 indicated. Each peak would not be a  $\delta$ -function, instead, it would have a narrow width.

The input signal was fed into a subroutine which did the deconvolution. The procedure basically followed the description of the previous section,

except that the Fourier transformation was done in the discrete domain. The high frequency components of the shower fluctuation and/or electronic noise would result in ringing in the deconvoluted spectrum, leading to more small peaks than there should be. A software filter was applied to  $A(\omega)$  before the inverse Fourier transformation to reduce the high frequency components.

The GTH is noisier than the LGC, so different filter widths were applied to the two devices. The GTH and the LGC were also treated differently in the peak searching procedure.

For LGC, if the pulse height of a tube was larger than that of its neighboring tubes on each side and larger than a software threshold, then it was said that a peak was found and the tube was called the peak tube. In the ideal case, the pulse height of the peak tube was the area of the input shower. But in the real data, the peak was not a  $\delta$ -function and was generally represented by the peak bin and one of its neighboring bin with the larger pulse height. Those two bins were used to determine the position and energy of the shower. In the position calculation, an empirical formula was used to make the reconstructed peaks to be distributed uniformly in the bin. Another empirical formula obtained from studies on the electron calibration data was used in the energy calculation:

$$E = \kappa A_p f(x_0), \quad (5.16)$$

when  $\kappa$  is a parameter determined from the calibration data,  $A_p$  is the energy in the peak tube in deconvoluted space, and  $f(x_0)$  is a function of the distance of the shower peak to the center of the peak tube.

The definition for a peak in the GTH required that its peak bin pulse height be larger than that of two neighboring bins on each side. The rest of the procedure is the same as for the LGC. Only the parameters in Equation 5.16 were different from those of the LGC.

## 5.4 Comparison between the Deconvolution and the Sum-over-tubes Methods

In the case of an isolated shower in a calibration event, the shower energy in the hodoscopes could be calculated by summing the energies in all the tubes. The sum-over-tubes technique does not deal with the presumed shower shape, which is needed for all of the fitting techniques. It is best suited for the isolated showers, and is able to reconstruct energies of those shower accurately. Other techniques can be compared with this method to see how well they can determine the shower energy.

The parameters in Equation 5.16 were tuned to match energy values returned by the deconvolution technique to that from the sum-over-tubes method using 30 GeV/c electron calibration data. After the parameters were determined, the energies obtained by the two methods were compared at different calibration energies and were found to be in good agreement. Figure 5.3 shows examples of this comparison in different hodoscope planes at 10 GeV. The calibration electron energy correlation between  $x$  view and  $y$  views was also good as shown in Figure 5.4. In the normal hadronic interaction data, most showers are overlapped with others and may well

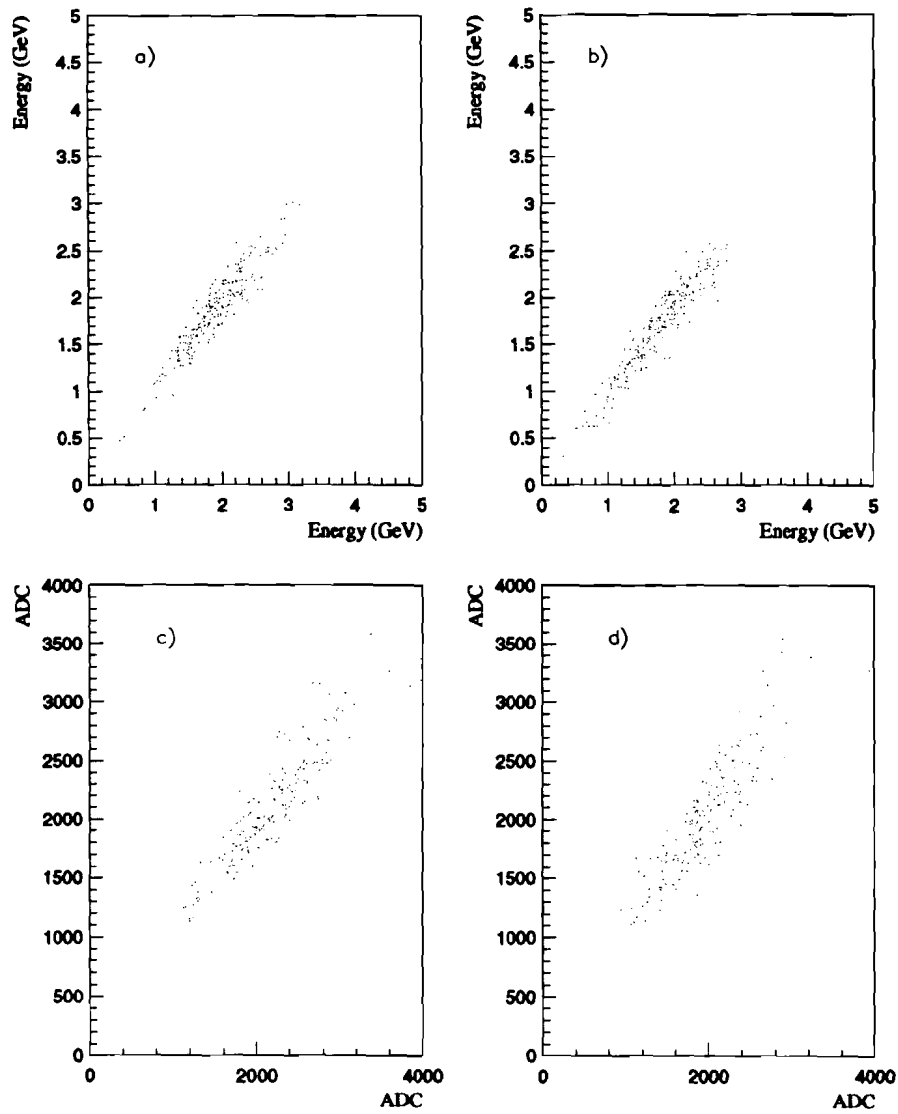


Figure 5.3: Correlation between deconvolution and sum-over-tubes. Vertical axis is energy energy from deconvolution technique, horizontal axis is energy from sum-over-tubes method. a): LGC x-view; b): LGC y-view; c): GTH x-view; d): GTH y-view.

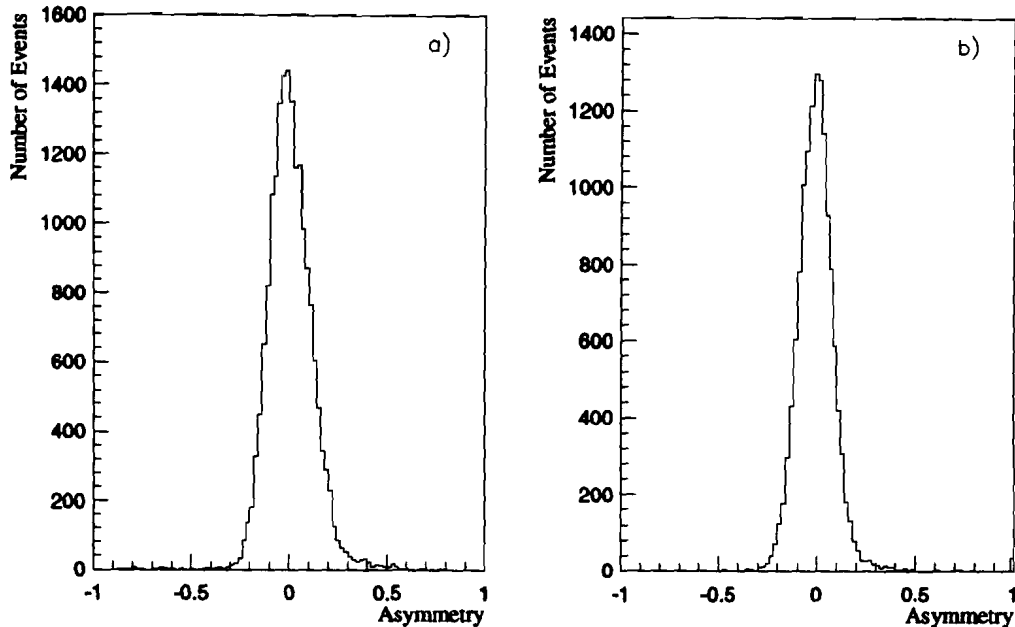


Figure 5.4:  $x - y$  energy match-up in hodoscopes. Asymmetry is defined as  $E_x - E_y / E_x + E_y$ . a): LGC; b): GTH.

fluctuate due to various reasons. The sum-over-tubes method cannot be used to get shower energies. Worse yet, it can not be used to determine the shower position for the overlapped showers.

## 5.5 Position Resolution

The  $x$  and  $y$  positions of an electromagnetic shower were determined by the hodoscopes, using the deconvolution technique.

There were five regions of different tube sizes as indicated in section 5.2. The position resolution depended on the tube size and shower width in each region. To determine the resolution, tracked beam positions were projected

*Table 5.2: Parameters of the Position Resolutions*

View	a	b	c
LGC $x$	$0.183 \pm 0.007$	$-0.556 \pm 0.085$	$5.569 \pm 0.202$
LGC $y$	$0.110 \pm 0.016$	$-0.286 \pm 0.186$	$5.272 \pm 0.411$
GTH $x$	$0.243 \pm 0.021$	$-0.425 \pm 0.223$	$6.287 \pm 0.469$
GTH $y$	$0.092 \pm 0.015$	$-0.752 \pm 0.189$	$4.018 \pm 0.432$
GTH $x$ (double)	$0.572 \pm 0.056$	$-2.059 \pm 0.490$	$8.999 \pm 0.966$

to the front face of the hodoscopes. A difference between the beam position and the position determined by the deconvolution method was calculated for each calibration event. Figure 5.5 shows the residuals of four different regions for 30 GeV/c calibration electrons. A Gaussian fit was applied to each distribution, and its width — the position resolution — was determined.

Figure 5.6 shows the position resolutions for the four regions. The error bars are not the error from the fit, which is much smaller. Instead, they came from the uncertainties of how many bins should be included in the fit. The GTH- $x$  double tube region did not have the 100 GeV/c beam and its resolution curve is not plotted in the figure. The other regions all had five calibration energies. A fit to the form

$$\sigma = a + \frac{b}{\sqrt{E}} + \frac{c}{E} \quad (5.17)$$

was performed for each region. The parameters are listed in Table 5.2. The overflow in the electronics (ADC) system clearly affected the resolutions at high energies.

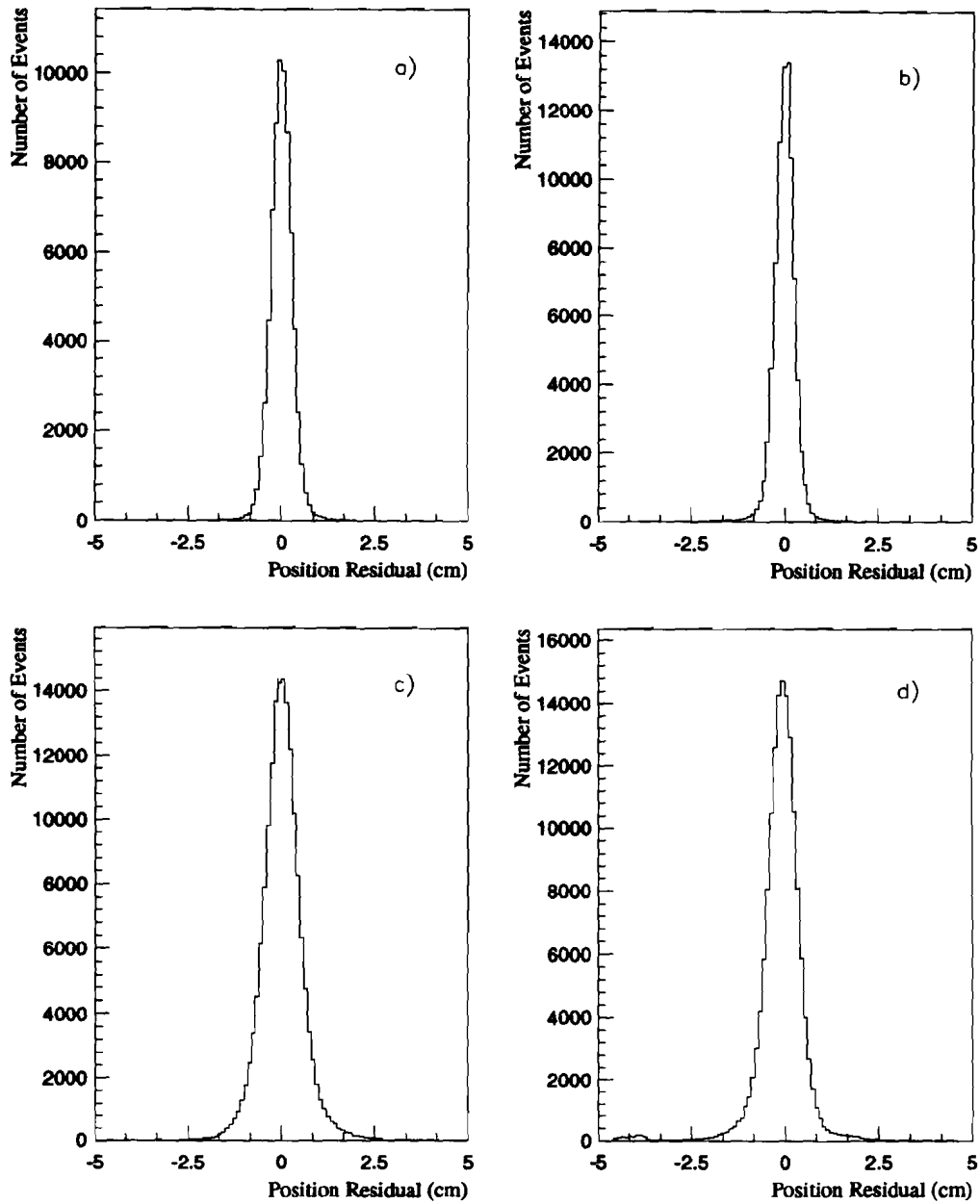


Figure 5.5: Hodoscope position - beam position residuals. a): LGC x-view; b): LGC y-view; c): GTH x-view; d): GTH y-view.

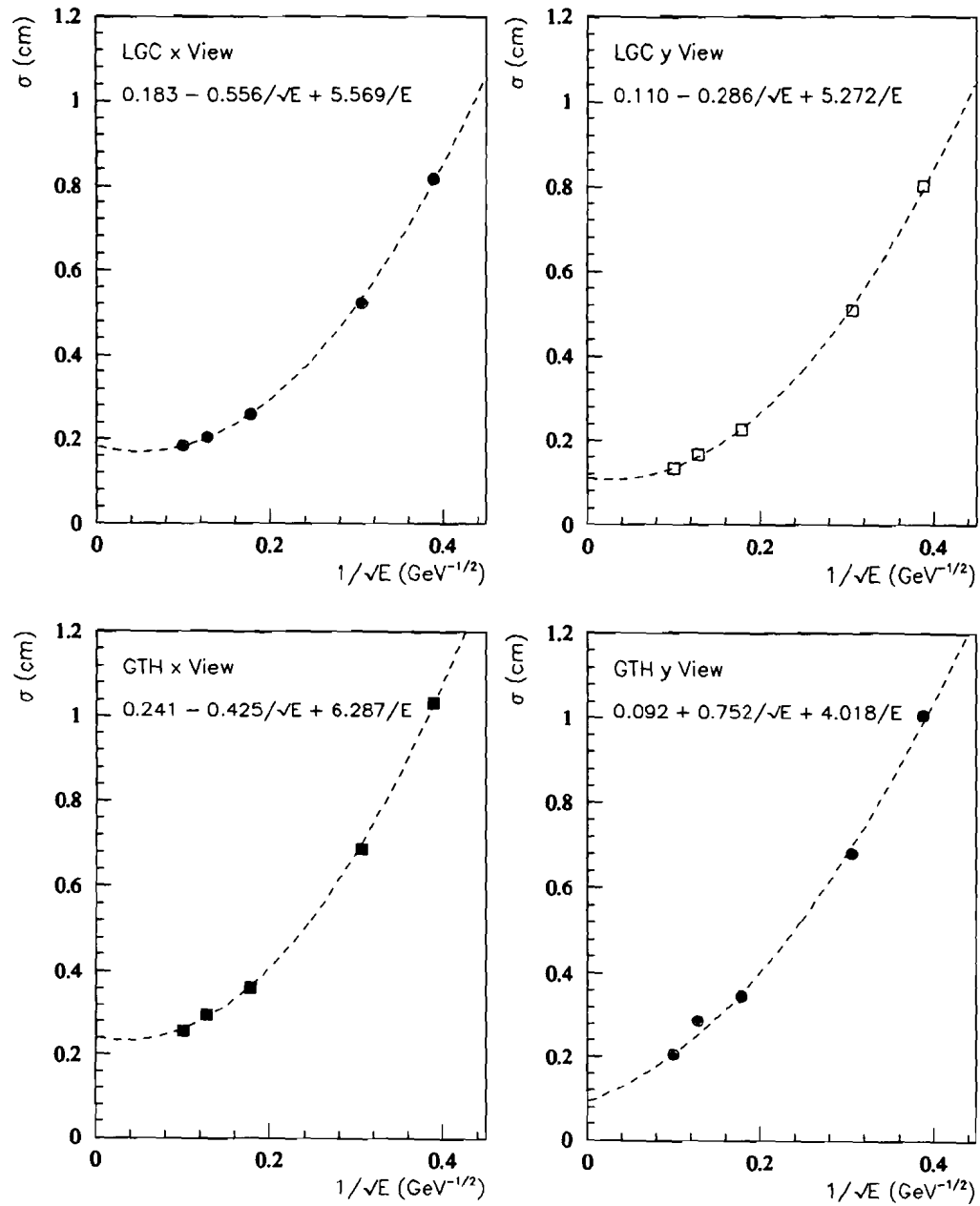
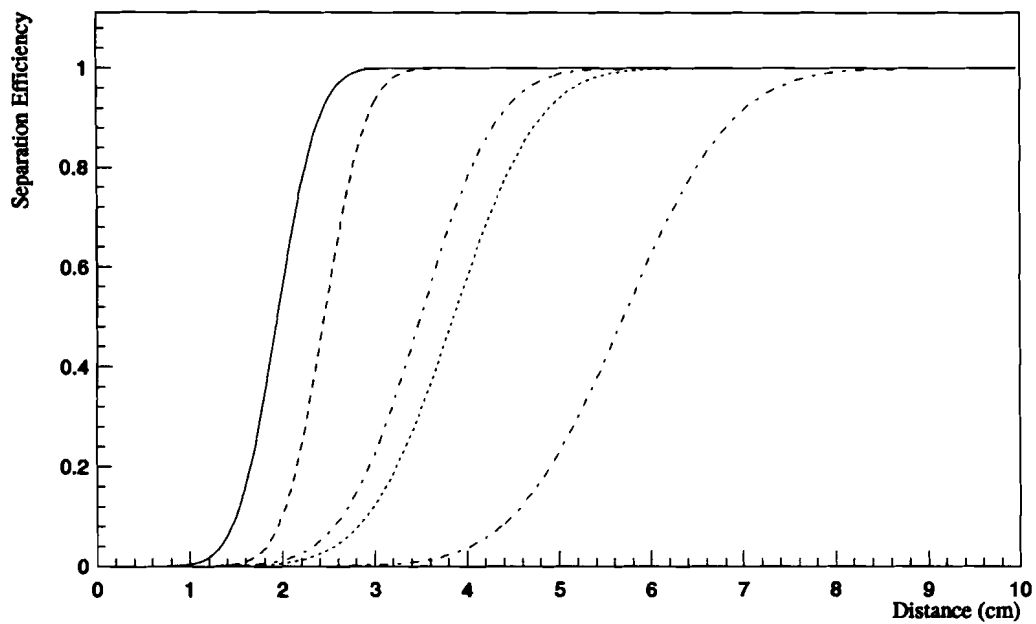


Figure 5.6: Position resolutions

## 5.6 Separation of Showers

The deconvolution technique showed its strength not only on determining positions of isolated showers, but also on resolving overlapping showers. The separation efficiencies depended on the tube sizes of different planes. For each type of tubes (strips), about one thousand 30 GeV calibration events were chosen to study the efficiency. The selection criteria were to have the distance between electrons fall within 10 cm with respect to a fixed reference point in the dimension of study, and to eliminate showers that involve bad tubes. Otherwise, the event selection was arbitrary.

Each electron shower was superimposed on all the other showers one at a time. The distances between the electrons were determined from the beam trajectories in both  $x$  and  $y$  views. Whether the program using deconvolution could resolve the showers depended on the peak definition, the shower shape, and the filter width. Figure 5.7 shows the separation efficiencies for the five tube types. The starting point, where the separation efficiency reached 10%, depended mainly on the peak definition and tube width, while the rising slope depended on the filter width and shower shape.



*Figure 5.7: Hodoscope shower separation efficiency. Solid line: LGC x-view; Dashed line: LGC y-view; Dash-dotted line: GTH y-view; Dotted line: GTH x-view single tube region; Right-most dash-dotted line: GTH x-view double tube region*

## Chapter 6

# Electromagnetic Shower Reconstruction

Less than 1/3 of the secondary particles produced in  $\pi Li$  and  $p Li$  interactions were  $\pi^0$  and  $\eta$  mesons, the rest were mostly other hadrons. In order to measure the production cross sections of those mesons, it is important for the experiment to be able to distinguish the  $\pi^0$  and  $\eta$  decay products — photons — from hadronic background and reconstruct their energies and positions accurately.

A shower reconstruction program was developed to search for photons. It used information from the EM calorimeter and tried to find electromagnetic showers and determine their energies and positions. Its basic algorithm included decoding, pattern recognition, shower energy and position fit based on the main array information, energy sharing among overlapping showers, and shower position determination from the hodoscope information. This procedure will be described in the following sections.

## 6.1 Decoding

As described in Section 3.6, the LGC and the GTH shared the same read-out system of LeCroy 2280 ADC, and the main array and active converter signals were digitized by a custom-built ADC system.

### 6.1.1 Main Array and Active Converter

The decoding of each glass channel included unpacking the ADC, subtracting a pedestal, and converting the result to energy. As described in Section 3.6.2, each ADC word had 16 bits. Its top bit was an indicator of whether a  $\times 8$  factor was needed to be applied to the lowest 12 bits which represented the signal of interest. The three bits next to the top bit were a measure of the *before* level when the signal was produced. Those bits were decoded and served as the parameter to correct the dynamic pedestal mentioned in Section 3.6.2.

In addition to the pedestal recorded with the LED pulser trigger during the electron calibration time when the beam particle rate was low, another pedestal component was identified and was found to have an approximately linear dependence on interaction rate. This dynamic pedestal was proportional to the average energy deposited in a block per second. The blocks in the central region could have dynamic pedestals up to 2 GeV, and this effect could cause problems in determining shower energies, particularly the low energy showers. A detailed discussion can be found in chapter 6 of reference [29].

The dynamic pedestal  $p$  in a main array channel  $m$  was represented by

$$p = \langle E_m \rangle \times (A_m \times E_{before} + B_m), \quad (6.1)$$

where  $\langle E_m \rangle$  is the average energy of the channel and depends on the polarity of the magnet and the beam particle type. It was extracted from normal running data and stored in parameter files representing different running conditions.  $A_m$ , and  $B_m$  are the slope and  $y$ -intercept of a plot whose  $x$ -axis is the "before" energy and the  $y$ -axis is the pedestal shift divided by the average energy in the channel, and they are block dependent. The rate dependence is represented by the "before" energy,  $E_{before}$ .

A main array block's energy was the product of the gain constant and the pedestal subtracted ADC counts. It was stored in an array  $EMA$  for every event. The energy of an active converter block was the product of the pedestal subtracted ADC counts and the first term,  $G_{AC}$ , in Equation 4.1 and was stored in an array  $EAC$ . The  $y$ -dependent correction was incorporated later after the  $y$  position of a shower was determined.

### 6.1.2 The LGC and the GTH

In the normal running, the LeCroy 2280 was set in the sparcified mode. The pedestal was automatically subtracted on-line. The pulse height was simply taken from the 12-bit ADC. For GTH- $x$  double tube region, the ADC value was divided by 2 for the following reason.

If a shower took place right on the boundary of the single tube and the double tube regions, the charges accumulated should be equal in both

regions. But the number of ADC channels in the double tube region was only one half of that in the single tube region, so the ADC values in the double tube channels would on average be twice as much as those in the single tube channels. This caused a sudden jump in the ADC value on the boundary, the deconvolution technique would not work properly in this kind situation. So it was necessary to divide the ADC values of the double tube channels, in order to reduce the error at the boundary in data analysis.

The ADC values were multiplied by the plane gains and relative tube gains to get the energies. The term “energy” will be used hereafter for both the LGC and the GTH, unless otherwise stated, even though it is the “gain corrected ADC” for the GTH.

The LGC energy needed further correction due to gain sagging and ADC overflow. The charged particles produced from showers would cause electric current on the LGC wire and reduce the voltage on the wire due to the power supply circuitry, thus, reduce the effective gain on the wire. The wires in the center were affected most, since there were more showers there. The current drawn was monitored on an event by event basis, and a correction was applied based on the current.

During the first half of the run, the high voltage on the LGC was set too high, resulting ADC overflows. The number of tubes with saturated ADC values is listed in Table 6.1 at different electron calibration energies. This posed a problem for the high  $p_T$  trigger events, since triggering cluster would have high energy and would likely saturate the LGC ADC. The voltage was

*Table 6.1: Percentages of Calibration Events with LGC ADC Overflows*

# of overflow tubes	<i>x</i> -view			<i>y</i> -view		
	1	2	3	1	2	3
<b>Earlier half</b>						
10 GeV	5.3	0.0	0.0	0.1	0.0	0.0
30 GeV	53.7	4.8	0.0	1.8	0.3	0.0
60 GeV	66.7	17.9	0.4	7.2	1.0	0.0
100 GeV	61.8	27.6	1.3	16.0	2.1	0.1
<b>Later half</b>						
10 GeV	0.0	0.0	0.0	0.0	0.0	0.0
30 GeV	0.3	0.0	0.0	1.5	0.0	0.0
60 GeV	12.2	0.1	0.0	8.8	0.6	0.0
100 GeV	37.4	1.3	0.0	22.0	2.3	0.0

lowered after the first half of the run, to reduce the ADC overflow problem. But for very high energy showers, the overflow still existed. The bottom half of Table 6.1 lists the percentage of overflow tubes in the last half of the run.

A fit was used in the analysis to correct the overflow whenever it occurred. The pulse shapes used in the fit differed a little from Equation 5.15, and took the form

$$P(x) = A[e^{-|x-B|/C} + \frac{D}{(x-B)^2 + F^2}], \quad (6.2)$$

where the first term has the same form as Equation 5.15, the second term is added in to take care of possible background from other showers. The parameters  $C$ ,  $D$ , and  $F$  were determined from a study of the calibration data. There were 12 different sets of  $C$ ,  $D$ , and  $F$  parameters, corresponding to 12 different locations of the shower peak in the peak tube. And  $B$  was

estimated by using the energy first moment of the two bins on each side of the overflowing bin. The magnitude  $A$  was the only free parameter in the fit. The fitted  $P$  was restricted between one and three times of the ADC full range (4095–12285).

If a tube was dead (or effectively so), its ADC value was taken from the geometric average of its neighboring channels, based on the shower shape in Equation 5.15. This method failed if the shower peak sat on the dead tube, or if two or more contiguous tubes were dead. This effect was corrected on average by a Monte Carlo program which will be discussed in Chapter 8.

## 6.2 Shower Reconstruction in the Main Array

The search for showers started in the main array. A pattern recognition routine looked for possible clusters, and split the energy of a block crudely when two or more clusters shared the same block. A more sophisticated fitting algorithm was used iteratively to find the energy and position of the showers, based on the *known* shower patterns generated by a Monte Carlo program.

### 6.2.1 Pattern Recognition and Initial Sharing

The cluster definition in the data analysis was similar to that in the cluster finder hardware. In order to find as many as possible clusters in the first try, the initial pattern recognition compared the central block energy only

with that of its side neighbors (the ones that shared a common plane), but not that of its corner neighbors (the ones that touched only by a common line). So two corner neighbors could both be peaks. The initial cluster energy was the sum of all neighbors' energies, and the position was initially taken to be at the center of the peak block. The clusters were listed in descending energy order, the high energy cluster (shower) was treated first in the following iterative fitting and sharing procedure.

In case of overlapping showers, the energy in one block could come from more than one showers. If this happened, this block's energy was initially distributed among the clusters proportionally to their total energies. The exception was that if the block was a peak of one cluster, then the energy was assigned solely to that cluster, its contribution to other clusters was set to be zero. This happened when both corner neighbors were peaks.

### 6.2.2 Shower Tables

The initial shower energy and position estimated in the pattern recognition and initial sharing were used as first approximations. To better determine the quantities, it was necessary to know the shower shape. An EGS based Monte Carlo program was written to generate photons which produced showers in the materials of the calorimeter. Shower shapes were extracted from those events based on energy, position in the calorimeter, incident angle, and longitudinal development of the photons.

About 100,000 photons were generated at each of the five energies: 1.00,

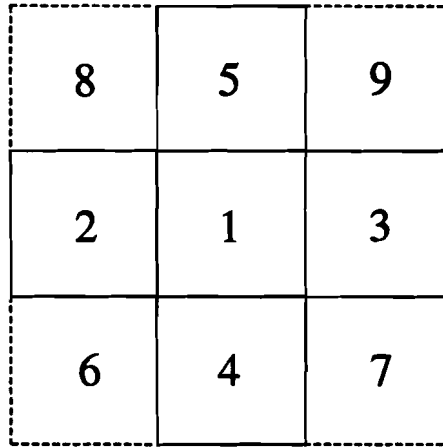


*Figure 6.1: Numbering convention for the nine-block cluster pattern.*

2.46, 6.05, 14.88, and 36.60. The energies were chosen with a formula

$$E_n = e^{0.9(n-1)}, \quad n = 0, 1, 2, 3, 4. \quad (6.3)$$

The exponential form was taken because of the logarithmic dependence of the shower shape on energy, and the value 0.9 was chosen so that the resulting energies would be close to our calibration energies.

Energies deposited in a cluster of nine blocks were recorded for each event. The naming convention is depicted in Figure 6.1. Block 1 is the peak, block 2 (4) is closer to the origin than block 3 (5) in  $x$  ( $y$ ). There could be seven different combinations of the small SCG, large SCG, and SF5 blocks in either the  $x$  dimension or the  $y$  dimension. Figure 6.2 shows examples of those combinations in  $x$ .

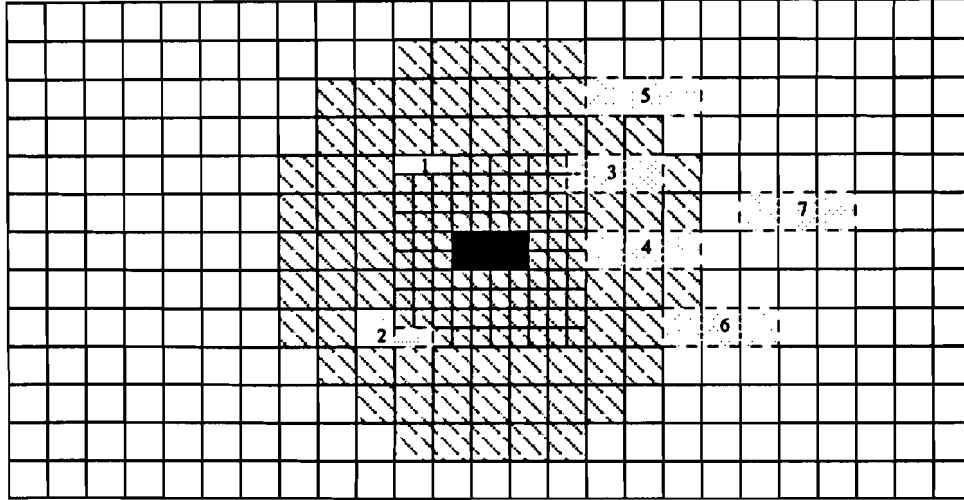


Figure 6.2: Examples of the three-block set combinations.

The shower shapes stored in a set of tables came from the energy ratios of five blocks forming a cross pattern. The ratios were:

$$\begin{aligned}
 e_1 &= \frac{E_1}{E_1 + E_2 + E_3}, & e_2 &= \frac{E_2}{E_1 + E_2 + E_3}, & e_3 &= \frac{E_3}{E_1 + E_2 + E_3}; \\
 r_{12} &= \frac{E_1 - E_2}{E_1 + E_2}, & r_{13} &= \frac{E_1 - E_3}{E_1 + E_3}, & r_{32} &= \frac{E_3 - E_2}{E_3 + E_2}
 \end{aligned} \quad (6.4)$$

where  $E_i$  is the energy in block  $i$ . The values of  $r_{12}$  and  $r_{13}$  would fall between 0 and 1, since the peak block energy  $E_1$  should always be greater than both  $E_2$  and  $E_3$ . The ratio  $r_{32}$  varied from -1 to 1. All three  $r$  ratios were divided into 10 segments evenly from their low limits to their upper limits. Tables of the  $r_{ij}$  ratios were generated by averaging the photon positions with respect to the peak block centers for all showers in certain  $r_{ij}$  segments. And tables of the  $e_i$  ratios were produced by dividing the peak blocks into

1 cm bins and averaging all the ratios for all showers in a given bin. The standard deviation of each ratio in each bin (segment) was also calculated, and was tabulated. So there were total of four kinds of tables: one for the  $e'_i$ 's which predicted the relative energies if position was known, another for the position when  $r'_{ij}$ 's were given, the other two for corresponding standard deviation tables.

Those tables were also indexed on calorimeter geometric region, energy, incident angle, and shower depth.

FXGEN(IVALUE,IRATIO,IREGION,IENERGY,IANGLE,IZ)

DXGEN(IVALUE,IRATIO,IREGION,IENERGY,IANGLE,IZ)

FEGEN(IVALUE,IRATIO,IREGION,IENERGY,IANGLE,IZ)

DEGEN(IVALUE,IRATIO,IREGION,IENERGY,IANGLE,IZ)

The last four indices have the same meaning in all four tables. The index *IRATIO* in the first two arrays (giving position and its uncertainty) runs from 1 to 3, indicating which  $r_{ij}$  is being used, and the first index *IVALUE* is the value of the ratio. In the last two arrays (providing energy and its uncertainty), *IVALUE* is the position (in cm) with respect to the center of the peak block, and *IRATIO* represents which of the three  $e'_i$ 's in Equation 6.5 is of interest.

To test the analysis program, the same tables were also produced for electrons hitting the calorimeter straight ahead (simulating the calibration events). Running the program on the electron calibration events using those tables was a routine procedure in the program development stage. The elec-

trons produced inside the target volume and deflected by the analysis magnet were simulated too. Their shapes were used in the analysis to reconstruct electrons, mostly from photon conversion in the target, in normal data.

### 6.2.3 Position and Energy Determination in Main Array

For a shower of estimated energy  $E$  in data, if  $E$  fell between interval  $[\text{IENERGY}, \text{IENERGY}+1]$ , its energy and position were determined by interpolating the values obtained from the tables with energy indices  $\text{IENERGY}$  and  $\text{IENERGY}+1$ . If  $E$  was below 1 GeV (or above 36.6 GeV), the position would take the value predicted by the 1 GeV (or 36.6 GeV) table. In energy determination, an extrapolation was used if  $E$  was above 36.6 GeV.

As a first step, the position were fitted right after the initial pattern recognition and crude energy sharing. In the  $x$  dimension, the three  $r_{ij}$  ratios were calculated from the three blocks in the central row (blocks 1, 2, and 3). All three  $r$  ratios were used in position calculation. For each ratio, *e.g.*  $r_{12}$ , if

$$r(\text{IVALUE}) < r_{12} < r(\text{IVALUE} + 1),$$

the position  $x_{12}$  was obtained from interpolating between the numbers given by two position tables with their first index being  $\text{IVALUE}$  and  $\text{IVALUE}+1$ . The error on the position was calculated accordingly. The resulting (possibly different) three positions,  $x_{12}$ ,  $x_{13}$ , and  $x_{32}$  were averaged again to give a

better estimate of the shower position:

$$x = \frac{\frac{x_{12}}{\sigma_{x_{12}}^3} + \frac{x_{13}}{\sigma_{x_{13}}^3} + \frac{x_{32}}{\sigma_{x_{32}}^3}}{\frac{1}{\sigma_{x_{12}}^3} + \frac{1}{\sigma_{x_{13}}^3} + \frac{1}{\sigma_{x_{32}}^3}} \quad (6.5)$$

where the  $\sigma$ 's are the error deduced from the tables. The  $y$  position was determined in the same way using information from blocks 1, 4, and 5.

The position determined above was used in the shower energy calculation. The relative energies in blocks 1, 2, and 3 were estimated based on the  $x$  position by looking into the energy tables, *FEGEN*. The same was done to get the relative energies in blocks 1, 4, and 5 based on the  $y$  position. The peak block (block 1) was involved in both the row energies and column energies. Its energy  $E_1$  would have two slightly different values. A constraint was imposed to equalized the energies,  $E_1^x$  and  $E_1^y$ . The energies of blocks 4 and 5 were multiplied by the ratio of block 1 values to get a normalized shower shape in the cross pattern.

$$E'_4 = \frac{E_1^x}{E_1^y} E_4; \quad E'_5 = \frac{E_1^x}{E_1^y} E_5. \quad (6.6)$$

The above procedure gave only the relative energies among the five blocks. The absolute energy scale came from a  $\chi^2$  fit [33], which used a  $9 \times 9$  covariance matrix to take care of the correlation among the nine blocks. The matrix  $M_{ij}$  element was 1 on diagonal or if block  $i$  and block  $j$  were neighbors, and 0 otherwise. The correlation was modified by the energy ratio  $E_i \times E_j / \max(E_i, E_j)^2$ , meaning that if the energies in two blocks were equal, then they were completely correlated, and if one energy was much smaller

than the other, then they were uncorrelated. The  $\chi^2$  of the fit was:

$$\chi^2 = \sum_{i,j} (E'_i - E_i)(E'_j - E_j) M_{ij} \frac{E'_i E'_j}{\max(E'_i, E'_j)^2}, \quad (6.7)$$

where the primed terms were the energies estimated in the current iteration, while the un-primed terms came from the previous iteration. And  $\max(a, b)$  means to take the largest of the two.

The corner blocks were not used in the fit, because that the energies deposited in them were small and had relatively large fluctuations, and also because that there were possible overlap of showers in those blocks. Their energies were estimated after the energies of the five blocks in the cross pattern were determined. If a photon hit the peak block at normal incident, the shower would (on average) be a circle in the  $x$ - $y$  plane. If the photon position was on either of the boundaries common to blocks 1 and 6, then the energy deposited in blocks 6 is given by:

$$E_6 = E_2 \times E_4 / E_1. \quad (6.8)$$

Further empirical corrections were made to the corner block energies based on the photon incident angle, the shower position with respect to the center of the peak block, and the peak block type. The factors came from a study of the EGS events.

A new  $\chi^2$  was calculated with Equation 6.7 using all blocks in the shower. The final estimated error used as a criteria to judge the shower quality was the product of this  $\chi^2$  and the sum of energy errors determined from the EGS tables. From now on, this product will be called  $\chi^2$ .

If one main array block's energy came from more than one shower, the energy was partitioned among the showers. The energy,  $E_i$ , assigned to  $i$ th shower was proportional to the estimated energy contribution from that particular shower to the block based on the fit.

$$E_i = E_i^{fit} \frac{E_{raw}}{\sum_{j=1}^n E_j^{fit}}, \quad (6.9)$$

where the sum is over,  $n$ , number of shower sharing the block. Thus, for a given block, the sum of its shared energies (input to various shower fits) was always equal to the raw block energy,  $E_{raw}$ .

The fitting and sharing procedure was iterated several times in the program. The energies and positions of the showers were stored in a common block, *SHOWER*, after each iteration and were used as initial values for the next iteration.

### 6.3 Shower Reconstruction in Hodoscopes

After three iterations of shower reconstruction in the main array, the program started looking into the hodoscopes to find showers there and to provide a more accurate position measurement.

#### 6.3.1 The Initial Search

In the first search, it was intended to find a peak in the hodoscopes associated with each main array shower. For each shower, the position estimated from the main array was projected to the hodoscope as the center of a searching

window. The window was a rectangle with area of  $2a \times 2b$ . The half window width in  $x$ ,  $a$ , was equal to three times of the error in  $x$  and was restricted between 3 and 6 cm; the half window width in  $y$ ,  $b$ , was equal to three times of the error in  $y$  and was restricted between 3.5 and 7 cm. The search was carried out with the procedure described in Chapter 5 using the deconvolution technique. Peaks in  $x$  and  $y$  views were found independently, and were arranged in descending energy order in each view. In case the searching window was in the LGC and the GTH overlapping region, or the window crossed the device boundaries, the peak found in the LGC took higher priority. If a GTH peak was within 1 cm of an LGC peak in either view, it was dismissed and only the LGC peak was kept.

After the peaks were established in both views, an attempt was made to match the energies in the  $x$  with those in the  $y$  view and find  $x$ - $y$  crossings. The requirements for a possible crossing were:

- A peak in either view had not already been associated with another main array shower;
- The energy asymmetry

$$A = |E_x - E_y| / (E_x + E_y) \quad (6.10)$$

was less than 0.5

- For the LGC,

$$E_x, E_y > 0.04\sqrt{E_{BMA}},$$

where  $E_{BMA}$  is the energy in the main array block directly behind the possible crossing.

In case two showers overlapped in one view (*e.g.*  $x$  view), but not in the other view ( $y$  view), it was tried to match the  $x$  energy,  $E_x$  with the sum of the two  $y$  energies,  $E_y^1$  and  $E_y^2$ . (This happened often since two photons from a high energy  $\pi^0$  decay were likely to produced showers close by.) The asymmetry of the one-to-two match-up was

$$A = |E_x - E_y^1 - E_y^2| / (E_x + E_y^1 + E_y^2). \quad (6.11)$$

The cut on the asymmetry for the two-to-one match-up was 0.25 for the LGC, and 0.35 for the GTH. If a possible two-to-one match was found, the  $x$  energy was split into two portions whose values were proportional to the  $y$  energies:

$$E_x^1 = \frac{E_y^1}{E_y^1 + E_y^2} E_x; \quad E_x^2 = \frac{E_y^2}{E_y^1 + E_y^2} E_x. \quad (6.12)$$

The asymmetries were the same for both crossings as determined from Equation 6.11.

Sometimes, there were more than one match-up found inside the searching window. In the initial iteration, only the match-up with the best asymmetry was picked. In the two-to-one match-up case, the crossing with higher energy was selected. The asymmetry of the final acceptable crossing had to be less than 0.25 in the LGC region and 0.35 in the GTH region.

If a crossing was found in the hodoscopes for a main array shower, its position was projected to the main array and used as the optimal shower

position. This position was not changed in further iteration of shower fitting in the main array. The energy of that shower could still change because of the sharing. If there was no match-up found in the hodoscopes, the position estimated from the main array was retained. Further fitting iterations could change the shower position, as well as the shower energy.

### 6.3.2 Adding New Showers

The above procedure did not change the number of showers in the event. It merely provided a better position measurement for a given shower. In many cases, there were showers overlapping together, and the pattern recognition in the main array could not pick all of them out because of the large size of the glass blocks. If two showers centered on one block, the pattern recognition could only find one shower. Another case was that two showers centered on blocks 2 and 3 (Figure 6.1), and near their borders with block 1, the energy deposited in block 1 contributed by both showers could exceed that in both blocks 2 and 3. Block 1 would mistakenly be picked up as the center of a single shower.

The hodoscopes had finer cell widths, and were designed to pick out all electromagnetic showers. The only handicaps to them were the noise in the devices and their electronics, and the statistical fluctuations of showers which could lead to mismatches in the  $x$  and  $y$  views.

After four more fitting and sharing iterations in the main array, the hodoscope information was used a second time to search for more showers. The

criteria of defining peaks and crossings remained unchanged. But the searching window was enlarged to cover the area of nine blocks associated with the main array shower. The maximum number of crossings allowed was four in a single window. If a shower did not have its position determined in the first hodoscope search, or if it did, but the position was not close to any of the new crossings, the shower was discarded. New showers were added to the original shower list based on the positions found in the hodoscopes. To establish a new shower, it was required that:

- Sufficient energy be present in the main array block directly behind the hodoscope crossing;
- No existing shower was within 1 cm of the crossing in either  $x$  or  $y$  view.
- In the GTH region,

$$E_{BC} \geq 30 \text{ MeV}, \quad \text{and} \quad E_{BC} \geq 0.005E_{BMA},$$

$$ADC_x, ADC_y > 100E_{AC},$$

where  $E_{BC}$  is the energy of the second layer active converter block directly in front of the crossing,  $ADC_x$  and  $ADC_y$  are the ADC counts of the  $x$  and  $y$  views, and  $E_{AC}$  is the total active converter energy in GeV. (Figure 6.3 shows the correlation between the ADC counts and the AC energy for 30 GeV electron showers.)

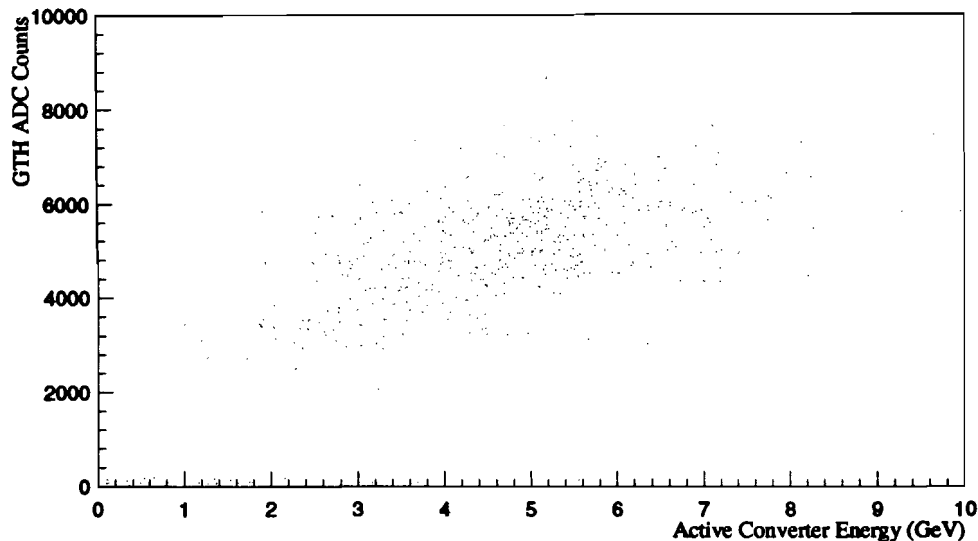


*Figure 6.3: Correlation between the GTH ADC counts and the active converter energy for 30 GeV electron showers*

## 6.4 Further Iterations

After adding new showers, further fitting and sharing was carried out for up to 14 more times or until all of the showers converged, whichever came the first. A shower was converged if in two consecutive iterations its  $x$  and  $y$  positions were changed no more than 0.5 mm and its total energy change was less than 10 MeV. If a shower's position was determined from the hodoscopes, the position was fixed in the subsequent iterations, the energy of the shower could still change.

Before getting the total energy of a shower in the GTH region, it was

necessary to determine the energy deposited in the active converters. As mentioned in Section 6.1, the values stored in the  $EAC$  array represented the apparent energies, they had to be converted into absolute energies by taking the light attenuation into account. This could only be achieved after a shower's  $y$  position was determined.

Both  $x$  and  $y$  positions of a shower were projected onto the active converter planes. If the  $x$  center of an active converter was within 4.5 cm of the shower  $x$  position, the converter was considered to be associated with the shower. Considering the width of the converter (being 7.5 cm), this requirement meant that in most cases, only one front converter and one back converter were involved. About 20% of the times, there would be two converters in both front and back layers got counted. The  $y$  position of the shower was used, in Equation 4.1, to calculate the active converter energies. If  $-2 \text{ cm} \leq y \leq 2 \text{ cm}$ , the converters in both the top rows and the bottom rows were taking into account. If a converter block was occupied by more than one showers, its energy was shared among the showers, according to the main array energies of those showers. It was assumed the active converter energy was proportional to the square root of the main array energy for each shower.

$$E_{AC}^i = E_{AC} \frac{\sqrt{E_{MA}^i}}{\sum_j \sqrt{E_{MA}^j}} \quad (6.13)$$

After the energies in the LGC, the active converter, and the main array were determined, the total energy of a shower was calculated using Equation 4.13. The parameters  $\alpha$ ,  $\beta$ , and  $f$  were weighted averages as discussed

in Sections 4.4 and 4.5.

Besides the position and the total energy, the  $\chi^2$  of the fit, the energy contributions of each individual block, the sum of the main array energy, the sums of front and back converter energies, and the LGC  $x$  and  $y$  energies were all stored in the *SHOWER* common block for each shower. The timing of each main array block was also stored. The total number of showers was one of the parameters stored for each event. The higher energy showers was assigned higher priorities to be accepted in the later analysis to which we shall turn now.



# Chapter 7

## Data Analysis

To reduce the unnecessary computing time, a software filter was applied to the experimental data before the program described in the previous chapter was used to analyze the high  $p_T$  photon trigger data. The events which passed through the filter were processed by the analysis program. The photon with the largest  $p_T$  in each event was combined with other photons in the event in an attempt to reconstruct the  $\pi^0$  and  $\eta$  mesons.

### 7.1 Data Reduction

The experiment took not only the single photon trigger events, but also di-muon and di-photon triggers. The single photon trigger events amounted to only about 13% of total data. It was therefore unnecessary to run the electromagnetic analysis program through all of the data. A filter program, running on the Fermilab ACP system, was used to branch the raw data into three different tapes, one for each trigger type mentioned above. It applied some minimal trigger dependent cuts to eliminate the unreasonable events.

For the single photon events, the main concern was to eliminate triggers caused by hadronic showers in the calorimeter, and by noise in the electronic system. Since the program was a fast filter, it worked with the raw clusters, defined in a similar fashion to the cluster finder hardware. For a cluster to be accepted as a good photon candidate, it had to meet the following requirements:

- The peak block of the cluster had to be outside of the central area of 45 cm to avoid the busy region;
- The minimum energy threshold of the peak block was set to 4 GeV.
- One of the peak block's  $p_T$  bits had to be set in order for the cluster to be accepted as legitimate;
- The  $p_T$  of the cluster, converted from the raw energy of the cluster according the peak block position, had to be larger than certain thresholds in order to dismiss accidental triggers caused by the electronic noise. The threshold were set to be 1, 2 and 3 GeV for  $P_{T2}$ ,  $P_{T3}$ , and  $P_{T4}$  triggers, respectively.

Those candidates were subject to further cut of 200 MeV on energy deposited in the active plane, which was calculated in the following way. In the LGC region, the energies of the tubes and the strips within an area covered by the (nominally) nine block cluster were added together to give  $E_x$  and  $E_y$ . Both  $E_x$  and  $E_y$  had to be larger than 200 MeV. In the active converter

region, energies of four (two on each side of the peak main array block center) front and four back converters were summed up in most cases. When the peak MA block was in the middle row near  $y = 0.0$ , both top and bottom rows of the converters were used. This very minimal cut was intended to eliminate triggers induced by hadron pile-up in the calorimeter.

The resulting events after the cuts were analyzed by a track reconstruction program, which provided charge particles' momenta, slopes, and interceptions at the front face of the calorimeter and interaction vertices. If a vertex was not reconstructed for an event, it was assumed that the interaction occurred at the center of the target. That is the reason that the vertex distributions, shown in Figure 7.1, have spikes in the center. The track information was pasted at the end of each event record and was later used in the photon reconstruction program to remove showers with charge tracks in their vicinity.

## 7.2 Event Selection

The events passing the filter were analyzed on several VAX-workstations using the procedure described in the previous chapter. Further cuts were applied to those events before going through the whole procedure. First, events with two overflowing LGC tubes within 5 cm were eliminated. As shown in Figure 5.1, the LGC shower widths were very narrow. The central bin contained most of the shower energy, leaving less than one half of the shower energy in the side bins. The fit described in Section 6.1.2 relied

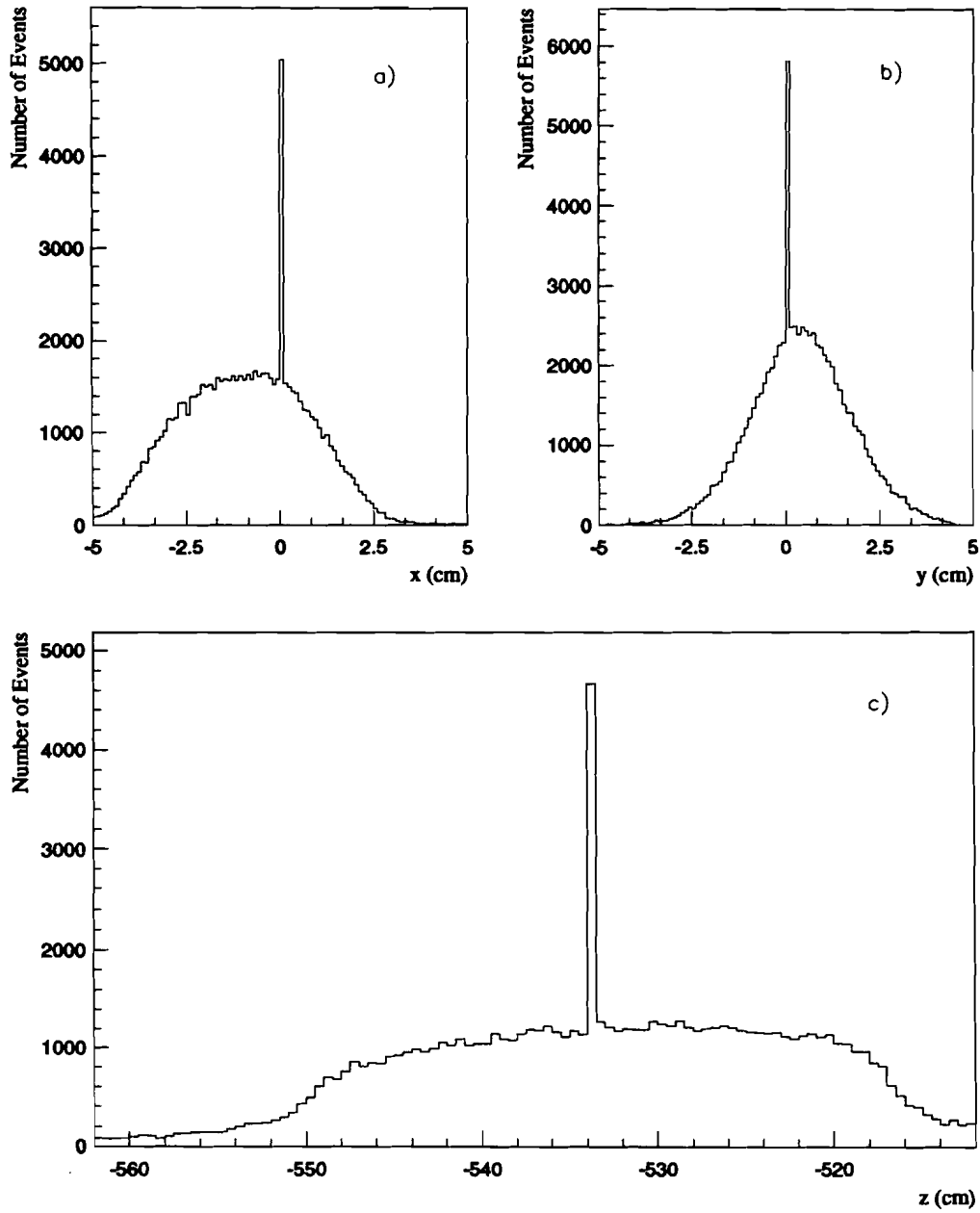


*Figure 7.1: Interaction vertex distributions. Positions are measured with respect to the origin of the experiment coordinate system.*

entirely on the sidebins. If two tubes nearby (within 5 cm) overflowed, the fit generally failed to predict the energies deposited in those tubes, resulting in big errors in both energy and position determinations. This situation occurred when a high energy  $\pi^0$  decayed symmetrically into two nearby photons, each of which caused one tube to overflow, or the  $\pi^0$  decayed very asymmetrically and the higher energy photon caused two contiguous tubes to overflow. The event lost due to this cut had to be estimated and corrected using a Monte Carlo simulation program. Second, an event was not accepted unless the raw  $p_T$  of its triggering cluster was greater or equal to 2.5 GeV.

The remaining events were then analyzed. After going through the reconstruction procedure, the program worked with showers rather than clusters. A shower was tagged as an electromagnetic one if its active plane energy was greater than 150 MeV. The shower of the highest  $p_T$  of an event had to meet the following requirements before the event was accepted and written to the tape for further study:

- Its center had to be outside of the central  $45 \times 45 \text{ cm}^2$  area;
- Had to be associated with the triggering cluster, *i.e.* the distances between the shower center and the cluster center had to be less than 15 cm in both  $x$  and  $y$  dimensions;
- Its active plane energy had to be no less than 200 MeV, *i.e.*  $E_{AC} \geq 200 \text{ MeV}$ ;
- Its  $p_T$  had to be no less than 2.8 GeV, or the  $p_T$  of its combination

with another electromagnetic shower had to be no less than 2.8 GeV with their invariant mass smaller than 1.5 GeV.

The shower information mentioned in the last paragraph of the previous chapter was appended to the end of each event surviving these cuts. The survival rate was about 20% for the early half of the data and about 27% for the later half of the data.

A series of stricter cuts were further applied to these events in an attempt to get good quality photons:

1. Vertex Cut. The interaction had to occur in the target, requiring the  $z$  position of the reconstructed vertex be within a range of -552 to -514 cm.

2. Timing Cut. Due to the nature of the high beam intensity, the 19 ns beam bucket interval, and the 200 ns of the calorimeter electronics gate, some energy measured by the electromagnetic detector came from the out-of-time particles, leading to higher apparent energy in the calorimeter and resulting in high  $p_T$  triggers that otherwise would not occur. As mentioned before, the difference between the time that energy was deposited in a main array block and the time that an interaction occurred in the target was measured by the TDC system associated with the main array. If the time difference in any of the blocks related to a shower was larger than  $\pm 10$  ns, the shower was tagged as out-of-time and was rejected. The event loss due to this cut will be discussed later in Section 8.3.

3. Hadron Rejection. The background to the photon signal in the calorimeter came mostly from hadrons which happened to shower in the

detector. And most hadrons were charged pions whose contamination could be reduced by cutting out showers with charge tracks within 8 cm from the shower centers. The loss of photon showers resulting from the cut was estimated by a PYTHIA Monte Carlo program and found to increase from 0% to 15% as  $x_F$  increased from -0.25 to 0.35 [34, pages 105 and 123].

But not all hadrons are charged, and not all charged hadron showers were reconstructed due to software and hardware inefficiency, more cuts were needed to clean up the hadronic background. Since the characteristics of hadronic showers are different from that of electromagnetic ones, one could minimize the hadronic background based on the difference. The LGC and active converter had only 0.1 and 0.33 absorption lengths, comparing to 3.0 and 3.5 radiation lengths, respectively. A hadron would much less likely (in contrast to photon or electron) to start showering in the active plane and deposit more than 200 MeV of energy there. Figure 7.2(a) shows the distributions of active plane energies deposited by 60 GeV charged pions and electrons, and Figure 7.2(b) shows the distributions of the ratios of the active plane energies to the square root of total energy measured in the calorimeter,  $E_{AC}/\sqrt{E_T}$ . The hadron rejection rates and the electron losses after three cuts applied sequentially in three different detector regions are listed in Table 7.1.

To further reduce the hadronic contamination, the  $\chi^2$  of a shower was required to be less than 3. The  $\chi^2$  cut was effective because the typical hadronic shower develops slower than the electromagnetic shower in the longitudinal

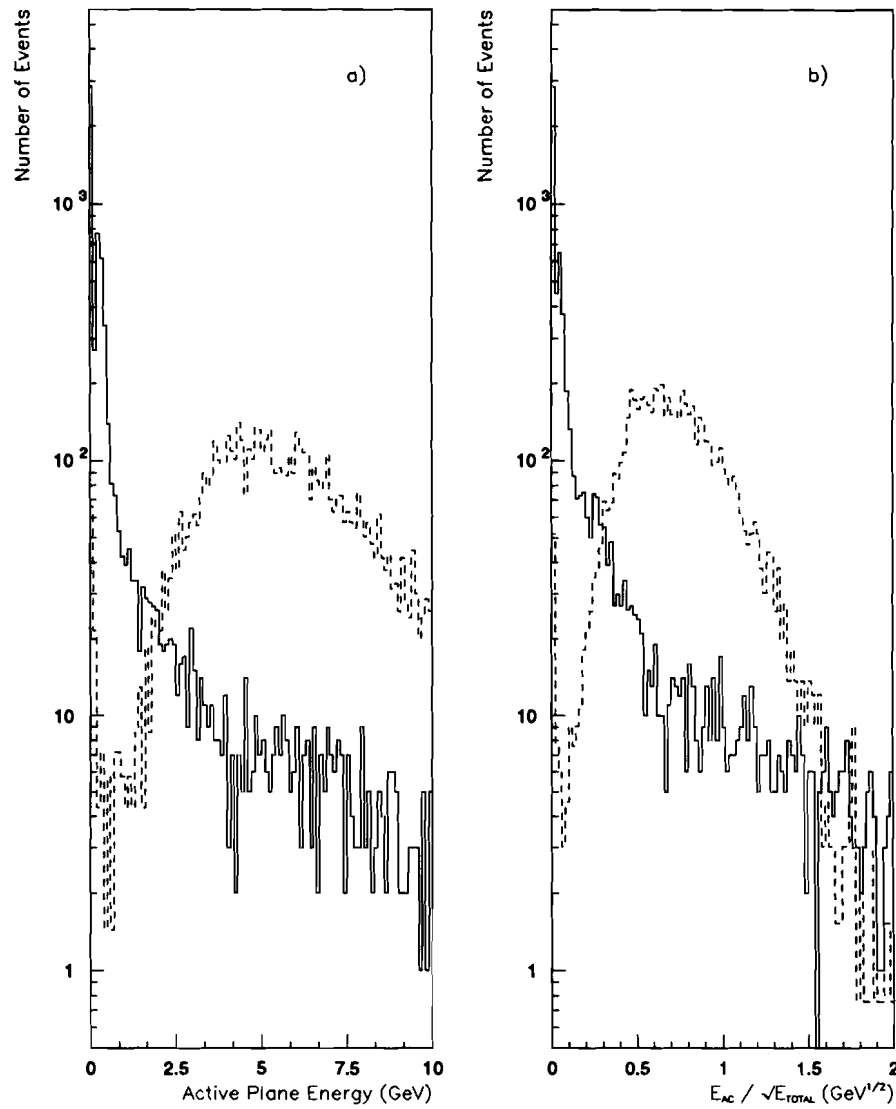


*Figure 7.2: Active plane energy for 60 GeV charged pion and electron. Solid line – pion; dashed line – electron. a): Active plane energy; b): ratio of active converter energy to square root of total energy in the calorimeter.*

Table 7.1: Hadron Rejection Rate and Electron Loss (%)

Cuts	Hadron			Electron		
	SF5	SCG/AC	SCG/LGC	SF5	SCG/AC	SCG/LGC
$E_{AC} \geq 200 \text{ MeV}$	39.5	26.3	90.2	2.2	0.5	1.5
$E_{AC}/\sqrt{E_T} \geq 0.15$	67.6	65.7	93.7	2.3	1.3	2.3
$\chi^2 \leq 3$	86.7	88.0	99.1	12.4	4.3	11.6

direction and has a broader shape in the transverse directions. Since the transverse shape used in the shower fitting routine was obtained for the electromagnetic one, the resulting  $\chi^2$  was much larger for the hadronic shower than for the photon or electron shower.

4. Hodoscope Crossing. As described in the previous chapter, the position of a shower could come from the fit based on the main array information alone, if no hodoscope crossing was found for the shower. But to ensure the good measurement of the shower position and thus the good measurement of meson decay angle as well as its transverse momentum, an electromagnetic shower was not accepted unless its position was determined from the hodoscope.

### 7.3 $\gamma$ - $\gamma$ Invariant Mass

The shower with the highest  $p_T$  (the triggering shower) in each event was combined with each of the rest of the showers in the event to form a  $\gamma$ - $\gamma$  invariant mass. Figure 7.3 shows an example of the invariant mass from the data of Negative 1 era. The kinematic range of the  $\gamma$ - $\gamma$  combination in the

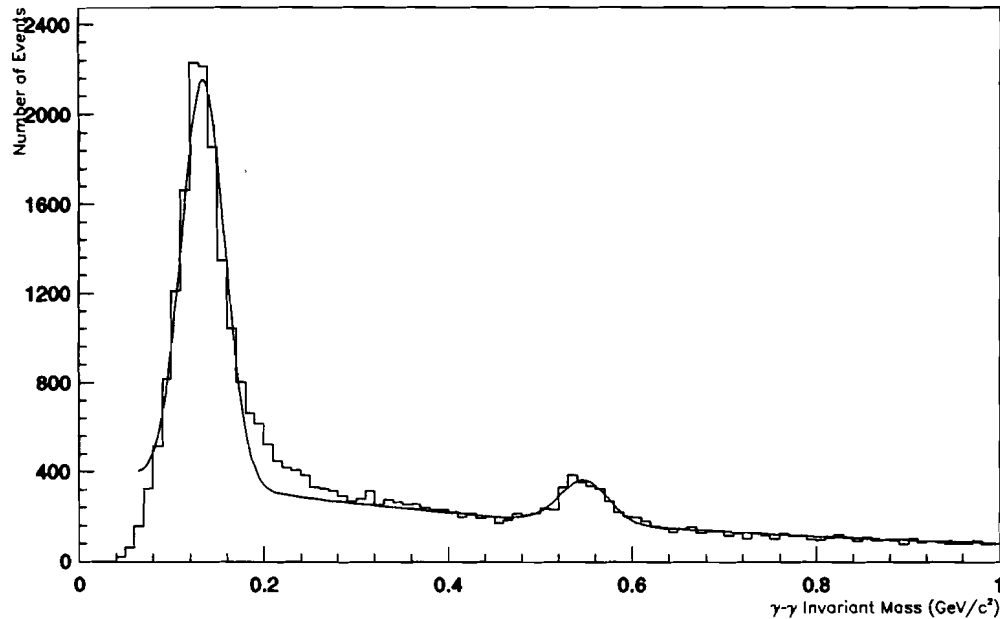


*Figure 7.3:  $\gamma\text{-}\gamma$  Invariant Mass.*

plot is  $3.5 \leq p_T \leq 7.0$ , and  $-0.25 \leq x_F \leq 0.35$ . A  $\pi^0$  peak and an  $\eta$  peak are evident in the plot. A fit to the mass plot using two Gaussians (one for  $\pi^0$ , one for  $\eta$ ) and an exponential (for the background) gave the central mass values and widths of the  $\pi^0$  and  $\eta$ . The fitted values of the  $\pi^0$  and  $\eta$  mass and width are listed in Table 7.2 for different eras. For the Positive 2 era, the  $\eta$  peak was not well established due to low statistics, so its value is not listed. It is clear from the table that the central values of the meson masses agree within 1% during the entire run. This indicates the energy scale of the experiment was accurate within 1%.

The shape of the background underneath the  $\pi^0$  was not known precisely

Table 7.2:  $\pi^0$  and  $\eta$  Mass and Width (in MeV).

Era	Negative 1	Positive 1		Negative 2	Positive 2	
	$\pi^-$	$\pi^+$	$p$	$\pi^-$	$\pi^+$	$p$
$\pi^0$ Mass	$134.7 \pm 0.3$	$134.8 \pm 0.9$	$135.0 \pm 1.0$	$133.6 \pm 0.8$	$135.0 \pm 1.8$	$136.9 \pm 1.9$
$\pi^0$ Width	$23.2 \pm 0.3$	$22.6 \pm 0.9$	$22.3 \pm 1.1$	$22.3 \pm 0.8$	$23.1 \pm 1.5$	$24.3 \pm 1.7$
$\eta$ Mass	$547.7 \pm 1.5$	$546.4 \pm 3.5$	$544.0 \pm 5.8$	$549.0 \pm 3.8$	-	-
$\eta$ Width	$26.5 \pm 1.8$	$23.4 \pm 3.9$	$28.4 \pm 4.2$	$27.4 \pm 3.7$	-	-

due to the lack of information on the lower side of the mass distribution. Several different shapes were tried. Using those different shapes could vary the  $\pi^0$  production cross section as much as 8%.

The width of the relatively broad  $\pi^0$  peak came mostly from the position resolution of the detector. As was discussed in Chapter 5, the photon opening angle from  $\pi^0$  decay was very small, making the mass very sensitive to the opening angle (Equation 5.3). The small opening angle also meant small spatial separation of the photons in the main array. This made it difficult to partition the main array energy properly for the two highly overlapping photon showers, and led to a relatively large error on the energy of each shower, although the error on the total energy of the two showers remained small. Figure 7.4(a) shows a distribution of the two-photon energy asymmetry of the  $\pi^0$ , defined as

$$A = \frac{|E1 - E2|}{E1 + E2}. \quad (7.1)$$

Since  $\pi^0$  is a pseudoscalar, the asymmetry is expected to show a flat distribution up to 0.8, then start to fall off due to the detector acceptance. The unphysical spike at zero on the plot came from the situation where two

photons were very close such that the fitting and sharing algorithm had to assign equal energy to the two photons.

For  $\eta$ , the photon opening angle was (on average) more than three times larger than that of  $\pi^0$ , the contribution of the position resolution to the  $\eta$  width was not as important. Its width listed in Table 7.2 was consistent with the energy resolution of the detector. Figure 7.4(b) plots the distribution of the  $\eta$  two-photon energy asymmetry. It has the shape expected for a spin zero particle measured in our detector.

An asymmetry cut of  $A \leq 0.8$  was applied to the  $\gamma\text{-}\gamma$  mass combination shown in Figure 7.2. This cut was intended to reduce the background coming from direct photon induced electromagnetic showers and the the remaining hadronic showers. Since the triggering shower was required to have high  $p_T$ , this cut implies an energy cut (low limit) for the second shower. This, along with the position separation efficiency (Section 5.6), produces the cut-off at the low end of the mass plot (Figure 7.3). The tail on the high side of the  $\pi^0$  peak came from two sources. In part, this tail is due to the inability to partition the photon energies properly. The mass square in Equation 5.1 is proportional to the product of the photon energies. Given the total energy ( $E1 + E2$ ), the product is at its maximum when two photons have the same energy. From the asymmetry plot in Figure 7.2(a), the energies of the two photons were forced to be equal even when they were not really equal, resulting in a higher mass. Second, the mismeasurement of the position also tended to give a higher mass. As was discussed in Section 5.6, the

hodoscopes have finite shower separation efficiency. Showers located closer than the minimum separation distance cannot be resolved by the program and may be reconstructed as one shower, leading to the loss of the  $\pi^0$ . So if the mismeasured distance is shorter than the real distance, the showers would have less chance to survive and form a  $\pi^0$ . While if the mismeasured distance is larger than the real distance, the showers will confine to a mass above  $\pi^0$  mean value.

The  $\eta$  does not have this problem, since the photons from its decay had well partitioned energies and well measured positions. But the fall-off at the large asymmetry end is faster for  $\eta$  than for  $\pi^0$ , due to the geometric acceptance.

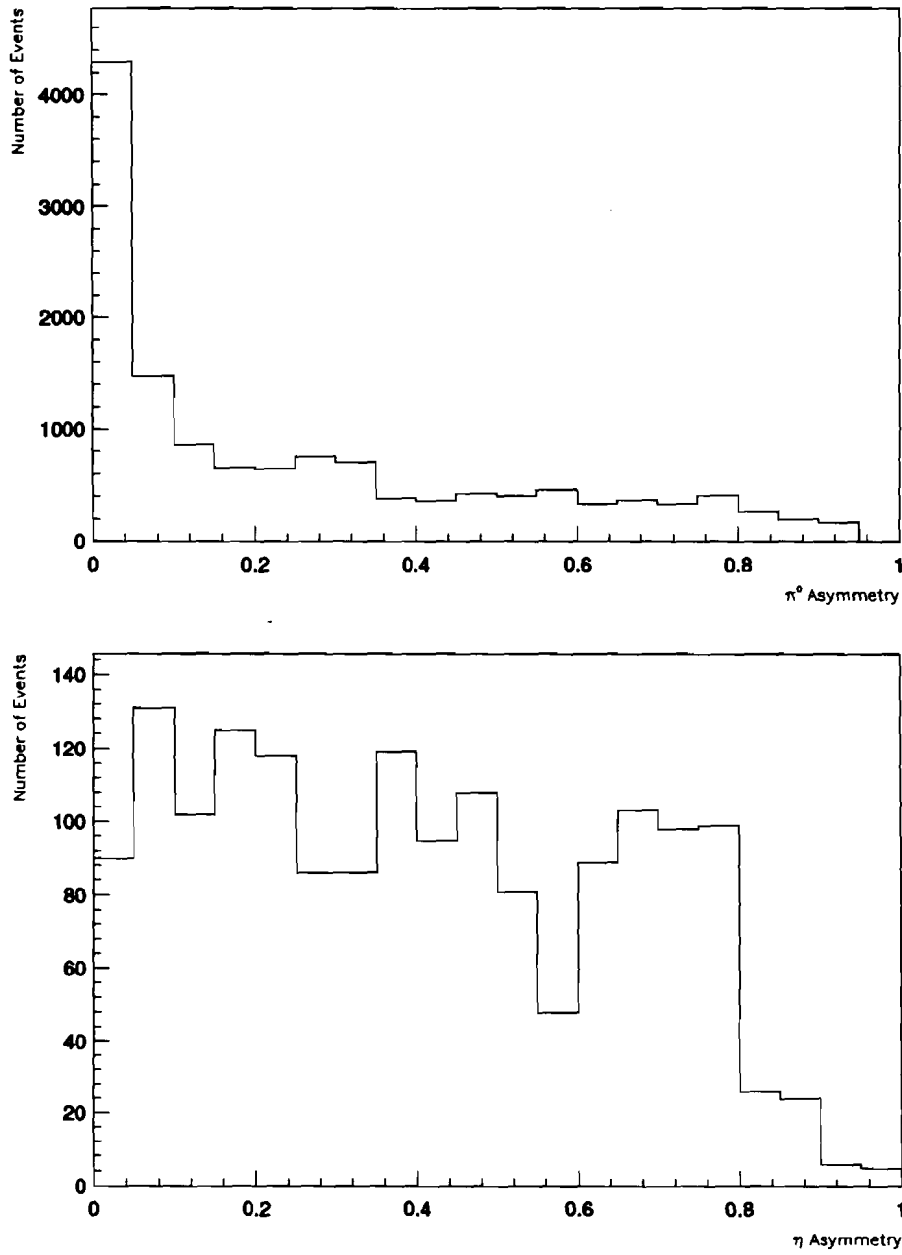


Figure 7.4: Two-photon Energy Asymmetry. Top):  $\pi^0$  ; Bottom):  $\eta$

# Chapter 8

## Normalization

In order to calculate the cross section of  $\pi^0$  and  $\eta$  production, it was essential to know the number of beam particles which causes the interactions, as well as the numbers of  $\pi^0$  and  $\eta$  produced in the interactions. The latter quantity was deduced from the number of the particles reconstructed, the reconstruction efficiency, the geometric acceptance of the detectors, and the trigger efficiency.

In this chapter, we will discuss the counting of beam particle, the cluster and meson trigger efficiencies, the loss of events due to the timing cut, and the acceptance and reconstruction efficiency derived from a Monte Carlo program.

### 8.1 Beam Counting

The numbers of pions and protons in each beam spill were read out and written to tapes in the end-of-spill record. In principle, the total number of the beam particles should just be the sum of pions and protons from all of the

spills. But the beam particle counting turned out to be not so simple. As was discussed in Section 2.1.2, the beam definition varied during the run, based on the number of hits in the beam station counters. The earlier definition implied that for each accepted event there was only one beam particle in a single bucket. The later definition allowed two particles in a single bucket. The double occupancy in a single beam bucket has to be properly corrected.

The correction was based on several latched quantities, *PION*, *PROT*, *BYG2*, and *BY2<sub>i</sub>*, written in the end-of-spill record on tape. The *BYG2* latch was set about 3.4% of the times to flag more than two particles in a bucket. When it was set, it was most likely that there were three particles in a bucket since the quadruple occupancy was very rare. The *BY2<sub>i</sub>* was the latch of the *i*th counter of beam station 2. The arithmetic sum of the *BY2<sub>i</sub>*'s,  $\sum BY2_i$ , indicated the number of particles in a bucket (discounting the rare occasions when two particles hit the same counter). The quantity *SBY2*,

$$SBY2 = \sum_{i=1}^{i=8} BY2_i - 3 \times BYG2,$$

was proportional to the number of beam particles accepted by the experiment. A scatter plot of *PION* versus *SBY2*, shown in Figure 8.1, shows that the pion scaler sagged as beam intensity increased. This is because that pion scaler would only count one particle when the *PION* latch was set, even if there were two particles in a bucket. The probability of double occupancy in a single bucket increases with intensity, leading to more pronounced sagging at high intensity. The same argument holds for the proton beam.

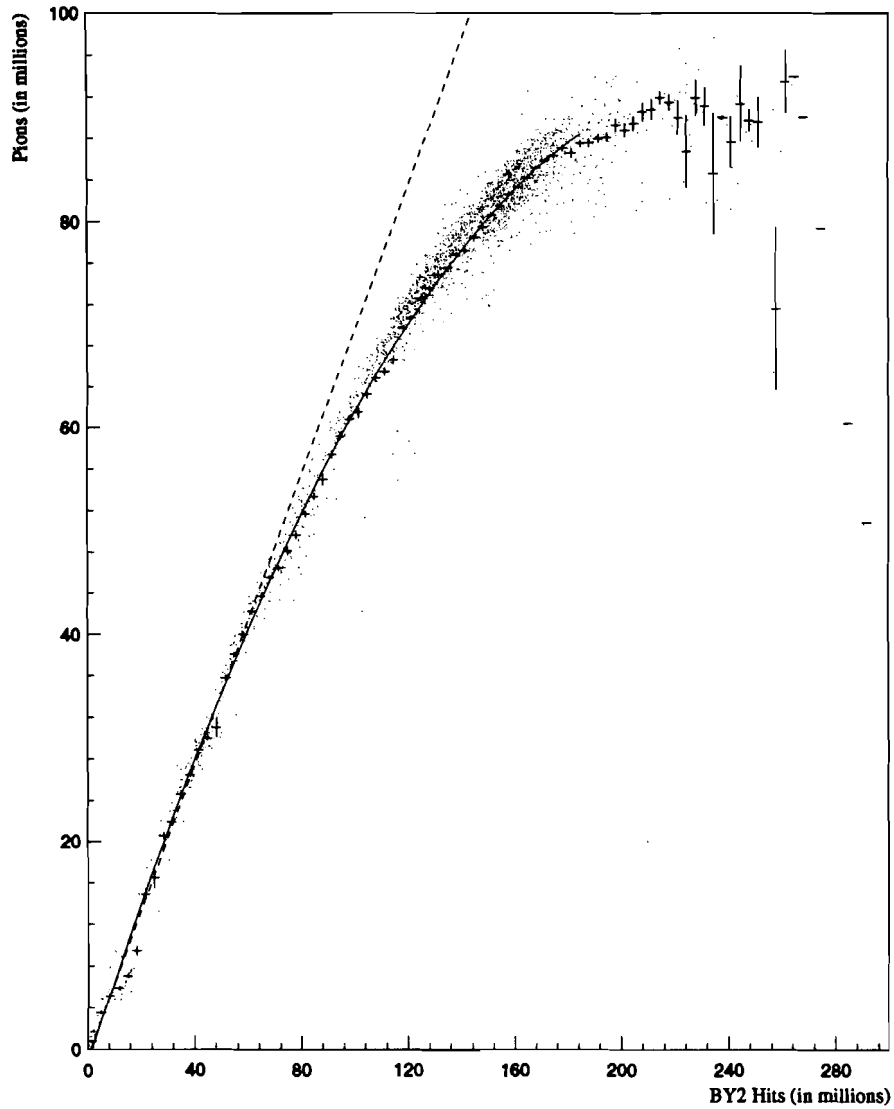


*Figure 8.1: Pion scaler sagging as function of beam intensity. The crosses represent the profile of the scatter plot. A quadratic curve is fitted to the profile. The straight line is a linear fit to the lower part of the plot*

*Table 8.1: Number of Beam Particles in Four Running Eras ( $\times 10^9$ )*

Era	Negative 1	Positive 1		Negative 2	Positive 2	
	$\pi^-$	$\pi^+$	$p$	$\pi^-$	$\pi^+$	$p$
Raw	1482	629	814	677	541	620
Corrected	1531 $\pm$ 42	655 $\pm$ 21	874 $\pm$ 32	873 $\pm$ 80	584 $\pm$ 24	701 $\pm$ 28
Live	1086 $\pm$ 30	456 $\pm$ 15	613 $\pm$ 23	617 $\pm$ 56	396 $\pm$ 16	475 $\pm$ 19

In order to correct the double occupancy phenomena, fits were performed to the scatter plots. First, a line was fitted to the lower part of the plot. Then a quadratic curve was fitted to the entire plot. The division of the line by the curve gave the needed correction factor. The error in the beam counting came from the efficiency of the latches and from the uncertainty of where the double occupancy became significant, *i.e.* where the line turned into a quadratic curve.

Table 8.1 lists the numbers of beam particles, with their corresponding errors, of four different running eras, before and after the correction. For the first negative beam era, only a small portion (about 15%) of the data needed the correction, since most data were taken with the earlier beam definition during that period. From the first positive era on, all of the data needed the double occupancy correction.

Also listed in the table are the numbers of CF-live beams which were defined as the number of particles arriving at the target when the cluster

finder was *alive*. The (percent) experiment live time was

$$t_l = \frac{\text{Number of Live Beam}}{\text{Number of Total Beam}}. \quad (8.1)$$

The *Live Beam* was latched when particles hit the target and the data acquisition (DA) system was alive. So  $t_l$  is the live time of the DA. For the subject of this study, we should count the number of beam particles when the cluster finder was also alive. This overall (percent) live time is

$$t_{CF} = t_l \times \frac{\text{Number of CFstrobe}}{\text{Number of Interaction}}. \quad (8.2)$$

From here on, the term *live beam* will be used for the *CF-live beam*. The live beam was calculated spill by spill based on the live time.

## 8.2 Trigger Efficiency

### 8.2.1 Physics Triggers

Besides the photon triggers, the experiment also recorded events caused by other physics triggers. The simplest one was the interaction (minimum bias) trigger, similar to what was described in Section 2.3.2. The only difference was that the trigger required the cluster finder be alive. So it was also called CF-strobe trigger which was very heavily pre-scaled to keep the number of minimum bias events written to the tape very small.

One of the two major goals of the experiment was to study the charmonium state production. In order to find the charmoniums, the experiment relied on a di-muon trigger. The electronic system searched for triple coincidence in two opposite quadrants of the three muon counter planes, MU1,

*Table 8.2: Percentage of Various Triggers*

Era	Negative 1		Positive 1			Negative 2		Positive 2
	1	2	3	4	5	6	7	8
di- $\mu$	53.0	70.8	71.8	74.5	71.2	66.2	83.2	87.2
di- $\gamma$	7.4	8.3	11.9	11.0	14.0	18.9	6.2	5.4
Strobe	1.0	1.2	0.8	0.7	0.6	0.5	0.6	0.8
2-V	6.2	11.0	5.6	6.8	3.5	0.5	0.6	1.1
$PT_2$	12.1	3.2	4.4	4.0	4.6	4.9	1.1	0.9
$PT_3$	12.4	3.7	4.1	1.9	3.7	4.9	4.3	2.6
$PT_4$	7.8	1.7	1.3	1.2	2.4	4.2	4.0	2.0

MU2, and MU3. A fast trigger processor then combined the information with those from the three down stream drift chambers (DC4, DC5, and DC6) to select events with the  $\mu$ - $\mu$  invariant mass exceeding 2.4 GeV.

Another trigger, called two-V trigger, was added to the experiment to select events with double "V" decays between two proportional chambers, PC2 and PC3.

The percentages of triggers written on tapes are tabulated in Table 8.2 for different eras. They depended on the prescale factor of each trigger, and the threshold in case of photon trigger. The change in those percentages reflected the need for the experiment to accommodate more di-muon triggers in the latter part of the run.

### 8.2.2 Cluster Finder Trigger Efficiency

The photon trigger thresholds and the prescale factors were sometimes altered even within one running era. This happened more frequently in the

*Table 8.3: Sub-eras of Different Photon Trigger Conditions.*

Era	Sub-era	Live Beams		Tape Range
		$\pi$	$p$	
Negative 1	1	633.4	-	1324-2578
	2	452.9	-	2579-3152
Positive 1	3	74.1	102.0	3230-3595
	4	69.7	93.7	3664-3916
	5	312.6	417.0	3917-5116
Negative 2	6	199.0	-	5155-5547
	7	417.7	-	5548-6017
Positive 2	8	396.1	474.8	6148-7350

earlier half of the run. Table 8.3 lists the sub-eras based on the tape numbers, along with the numbers of live beam particles (in unit of billion) accepted during the various conditions. The thresholds and prescale factors are tabulated in Table 8.4. The triggers indicated by the \* sign were not used in this analysis because of the low threshold and/or high prescale factor.

Figure 8.2(a) is an example of the raw  $p_T$  distribution from the accepted events, after adjustment of the prescale factors. The dark circles are for the high  $p_T$  triggers observed by the experiment electronics. The triangles are for all events that should have been seen, had there been no threshold cut. The two curves merge together at high  $p_T$  as they should. The fact that the high  $p_T$  trigger curve did not rise sharply meant that the trigger was not 100% efficient at the cut-off threshold due to the detector resolution. The

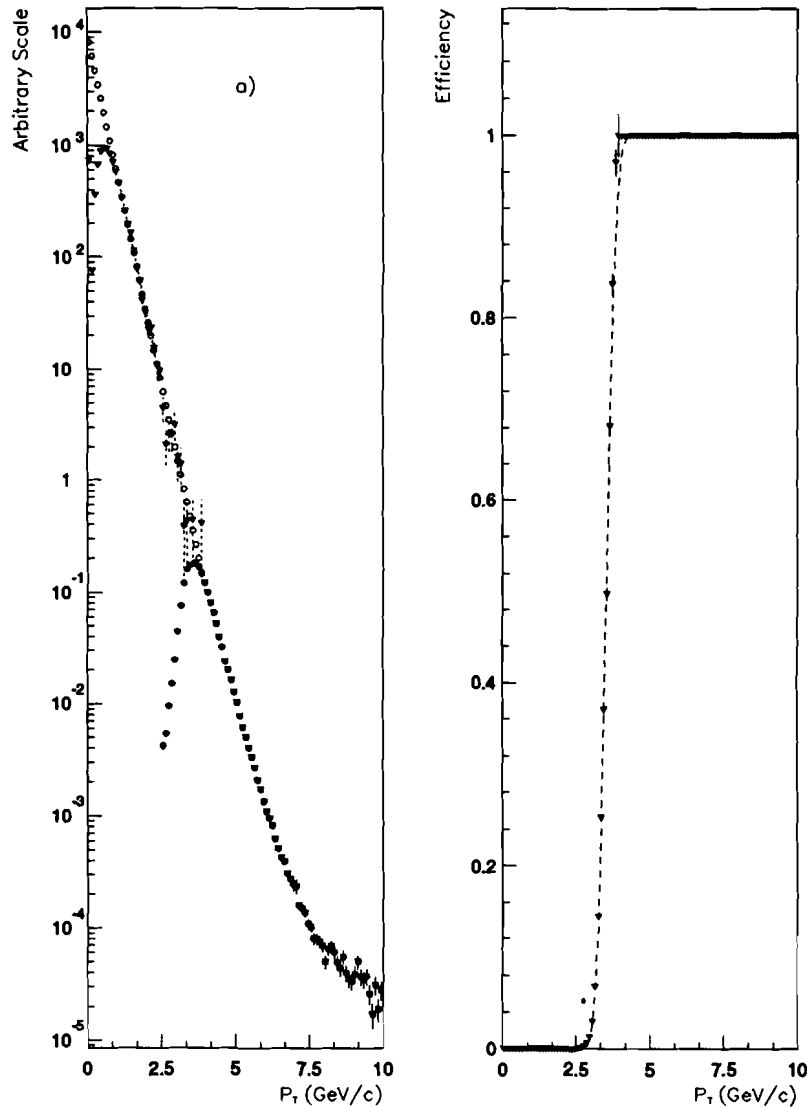


Figure 8.2: a): Raw  $p_T$  distribution. Solid circles are for  $P_{T2,3,4}$  trigger events; triangles are for all events (minimum bias and  $P_T$  triggers); open circles are from a fit to the minimum bias events (from 1 to 2.5 GeV). b): Trigger efficiency. Errors are statistical, and the dashed line is the fit.

Table 8.4: Thresholds and Pre-scale Factors for the  $P_T$  Triggers.

Sub-era	1	2	3	4	5	6	7	8
$p_{T2}$ threshold	2.4*	3.2	3.0	3.2	2.5*	2.5*	2.7*	2.8*
$p_{T3}$ threshold	2.8	4.1	3.8	4.1	3.4	3.4	3.8	3.9
$p_{T4}$ threshold	3.6	5.0	4.7	5.2	4.4	4.4	5.0	5.1
$p_{T2}$ pre-scale	32	32	32	32	128	128	512	512
$p_{T3}$ pre-scale	4	2	2	4	8	8	8	8
$p_{T4}$ pre-scale	1	1	1	1	1	1	1	1
$\tau^{**}$ (in GeV)	3.4	3.5	3.5	3.6	4.0	4.3	4.5	4.7

\* Triggers not used in this analysis

\*\*  $\tau$  was calculate based on the triggers used

ratio of the two curves should represent the trigger efficiency:

$$\epsilon = \frac{(S_2 \times N_2) + S_3 \times N_3 + S_4 \times N_4}{S_0 \times N_0 + S_2 \times N_2 + S_3 \times N_3 + S_4 \times N_4}. \quad (8.3)$$

The  $S_i$  is the prescale factor of a particular trigger, and  $N_i$  is the corresponding number of events recorded for the trigger. Their product is the observed number of events for the trigger. The extra term in the denominator is the number of the minimum bias events. For the latter half of the data, the  $P_{T2}$  trigger events were not used in the analysis due to the large prescale factor, eliminating the first term in the numerator.

The ratio is plotted in Figure 8.2(b). The errors are statistical. The data points are fitted to an error function, shown as dashed curve on the plot:

$$P(p_T) = \frac{1}{2} \times \frac{2}{\sqrt{\pi}} \int_{\frac{\tau-p_T}{\sqrt{2}\sigma}}^{\infty} e^{-t^2} dt. \quad (8.4)$$

The function represents the probability of a cluster with transverse momentum  $p_T$  could causing a trigger whose threshold is  $\tau$ , which is listed by sub-era

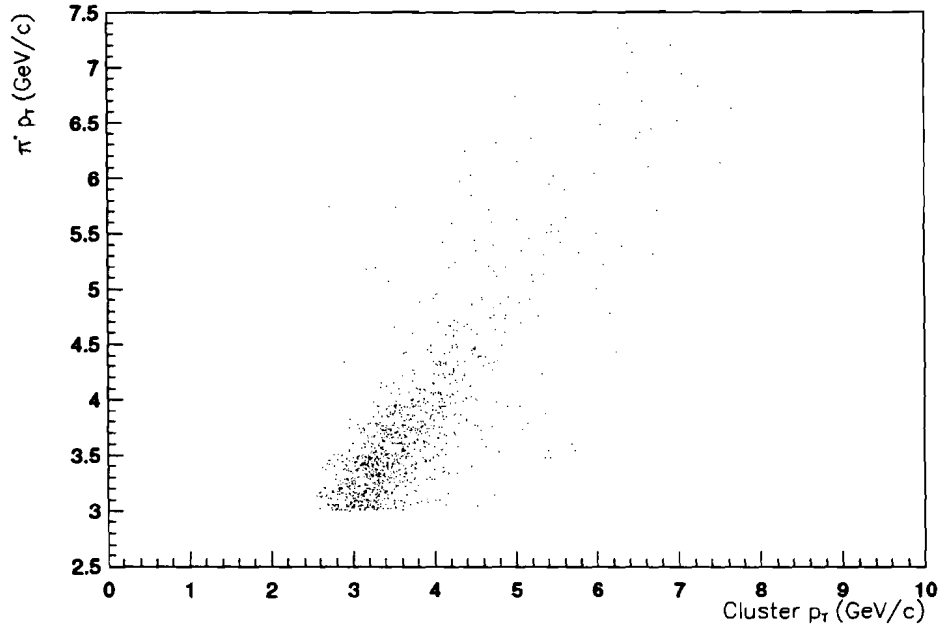


*Figure 8.3: Correlation between  $p_T$  of  $\pi^0$  and  $p_T$  of cluster. A cut at 3 GeV is applied to the  $\pi^0 p_T$ .*

in Table 8.4.

### 8.2.3 $\pi^0$ and $\eta$ Trigger Efficiency

The trigger efficiencies for  $\pi^0$  and  $\eta$  were different from that of the cluster. First, the two photons from the meson decay might not be in the same cluster. Thus, the  $p_T$  of the particle might not be the same as that of the cluster. Second, there is a difference between the  $p_T$  of a cluster and that of a reconstructed photon shower, due to energy contributions from other particles surrounding the shower.

In order to obtain the meson trigger efficiency, the  $p_T$  of the meson is

plotted against that of the cluster. Figure 8.3 shows an example. The meson trigger efficiency in a particular  $p_T$  interval,  $P_T$  to  $P_T + \Delta P_T$ , can be calculated in terms of the cluster efficiency:

$$\epsilon(P_T^{meson}) = \frac{\sum_{j=1}^{j=N_{bin}} \epsilon_j \sum_{i=2}^{i=4} S_i N_i}{\sum_{j=1}^{j=N_{bin}} \sum_{i=2}^{i=4} S_i N_i}, \quad (8.5)$$

where  $N_i$  is the number of events of  $P_{Ti}$  trigger in  $p_T$  bin  $j$ ,  $S_i$  is the corresponding prescale factor,  $\epsilon_j$  is the cluster trigger efficiency in that bin, and  $N_{bin}$  is the number of  $p_T$  bins along the  $x$ -axis. This method was sensitive to the statistical fluctuation in each  $p_T$  bin.

An alternative way to determine the meson trigger efficiency was to use the reconstructed meson and its reconstructed energy, let it decay isotropically into two photons in its CMS inside the target, and propagate the photons through the spectrometer, then use the pattern recognition program (simulating the hardware cluster finder) to find the  $p_T$  of the highest  $p_T$  cluster. The probability for that cluster (thus, the meson) to cause a trigger was determined by the cluster trigger efficiency (ref Equation 8.4 and Figure 8.2(b)). This method was less sensitive to the statistics, and was used in the analysis.

The trigger efficiencies of the reconstructed mesons are listed in Tables 8.5 and 8.6 in  $p_T$  bins for various sub-eras. Those numbers were used in calculating the meson production cross sections. In the cross section calculation, any data with meson trigger efficiencies below 10% were not used, since the percent errors on those efficiencies were large.

Table 8.5:  $\pi^0$  Trigger Efficiency (%).

Sub-era	$p_T$ bins (in GeV/c)									
	3.5	3.75	4.0	4.25	4.5	4.75	5.0	5.25	5.5	6.0
1	44.7	61.1	76.1	87.2	94.2	97.7	99.1	99.7	100.0	100.0
2	34.7	55.5	73.9	87.5	95.2	98.6	100.0	99.8	100.0	100.0
3	38.4	57.6	74.6	87.3	94.7	98.2	99.1	99.8	100.0	100.0
4	32.0	51.2	69.9	84.0	93.4	97.7	99.1	99.7	100.0	100.0
5	9.4	20.7	35.8	52.8	69.9	81.7	90.5	95.2	98.4	100.0
6	7.9	14.7	24.0	36.5	52.7	66.1	79.0	87.2	94.2	99.0
7	6.9	12.2	18.6	27.6	41.3	53.7	67.5	76.9	87.4	97.1
8	4.3	8.0	12.9	18.6	30.4	41.9	57.2	68.9	82.3	95.4

Table 8.6:  $\eta$  Trigger Efficiency (%).

Sub-era	$p_T$ bins (in GeV/c)					
	3.5-4.0	4.0-4.5	4.5-5.0	5.0-5.5	5.5-6.0	6.0-7.0
1	35.4	64.9	85.6	94.7	98.3	99.6
2	28.4	61.6	85.2	94.6	98.3	99.3
3	30.9	62.8	85.3	94.6	98.3	99.3
4	26.1	58.2	83.1	94.1	98.1	99.2
5	13.8	35.2	63.9	84.5	94.4	98.6
6	9.7	24.1	49.2	74.5	89.5	96.8
7	6.7	17.5	38.2	63.3	82.2	94.0
8	3.6	11.0	28.6	54.5	76.3	91.7

*Table 8.7: Event Loss Resulted from the Timing Cut (%).*

Sub-era	1	2	3	4	5	6	7	8
Loss	6.3	10.2	9.7	9.3	7.8	8.2	10.8	11.0

### 8.3 Timing Cut

As discussed in the previous two chapters, a shower could be totally out of time with respect to the interaction or a shower could be contaminated by other out-of-time showers. The timing of a shower was defined as the timing of the most out-of-time block in that shower. In this analysis, any shower with any contribution of out-of-time energy was not counted in the final calculation of cross sections.

Figure 8.4 shows the timing distributions of the cluster with the highest raw  $p_T$  in an event. The increasing number of the out-of-time high  $p_T$  events in the  $p_T$  triggers reflected the trigger bias. In case the trigger was caused by an out-of-time particle, the event was eliminated in the analysis and there was no correction applied to the cross section due to this cut. If the event was triggered by an in-time particle whose shower was contaminated by some out-of-time energies, cutting that event out will certainly result in underestimating the production cross section.

The minimum bias events were used here to estimate the loss of the good events due to the timing cut. The minimum bias trigger was independent of any information from the calorimeter and, unlike the  $p_T$  triggers, it did

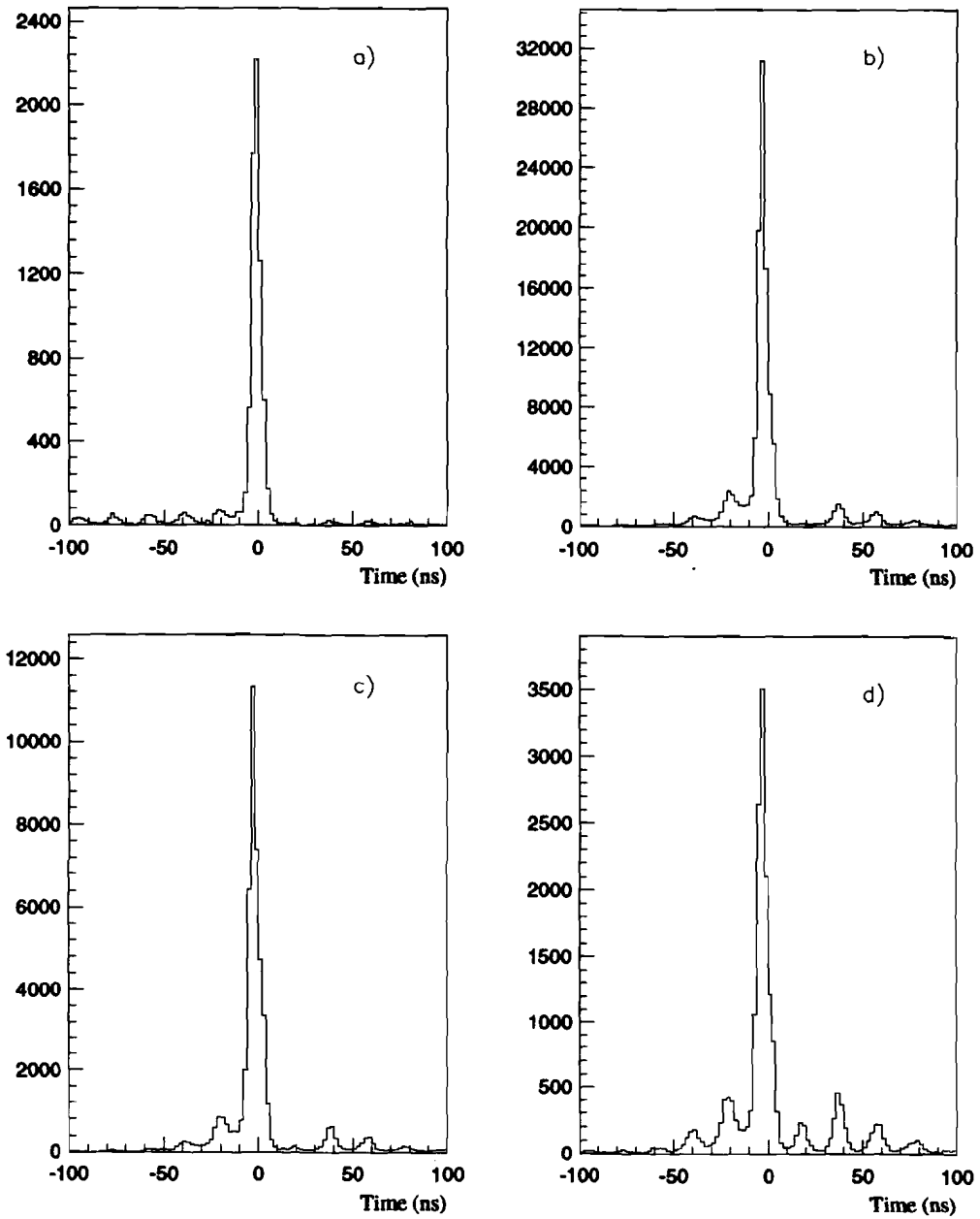


Figure 8.4: Timing with respect to interaction. a): Minimum bias trigger; b):  $P_{T2}$  trigger; c):  $P_{T3}$  trigger; d):  $P_{T4}$  trigger.

not bias toward higher energy. The fraction of minimum bias triggers with out-of-time energy reflected the percentage that a good event could be contaminated. The loss due to the timing cut is listed in Table 8.7 for various sub-eras.

## 8.4 Monte Carlo Simulation

### 8.4.1 Geometric Acceptance

The  $\pi^0$  mesons can possibly be reconstructed only if *both* photons were accepted by the calorimeter. When a  $\pi^0$  is produced in an interaction, it will most likely decay into two photons in about  $10^{-16}$  sec. The photons could convert into  $e^+e^-$  pairs inside the target. If a photon converted, it would not be reconstructed by the analysis program and is considered to be lost. In addition, any photon that hit the steel of the magnet was absorbed and could not arrive at the calorimeter. Even if both photons travel through the relatively empty air volume in front of the calorimeter, there is still a probability for the photons to be lost outside of the detector, because of the finite size of the detector and the opening angle between the photons.

This acceptance due to the spectrometer geometry was modeled by a Monte Carlo program. Since the final cross section will be calculated in terms of  $x_F$  and  $p_T$ , more than 100,000  $\pi^0$ 's were generated. The kinematic ranges were from 2.5 to 7.5 GeV/c for  $p_T$  and -0.35 to 0.45 for  $x_F$ . The events were evenly distributed in the area formed by the  $p_T$  and  $x_F$  bounds. The  $(x, y)$  position of the  $\pi^0$  was distributed in the target according to the vertex

Table 8.8:  $\pi^0$  Geometric Acceptance (%)

$p_T$	$x_F$					
	-0.2	-0.1	0.0	0.1	0.2	0.3
3.50-3.75	12.45	43.02	68.48	99.05	99.75	98.75
3.75-4.00	18.59	44.36	70.25	98.39	99.75	99.68
4.00-4.25	20.81	42.84	66.79	97.95	99.74	99.84
4.25-4.50	29.07	44.31	67.37	98.01	100.00	100.00
4.50-4.75	30.48	49.10	64.61	98.50	99.58	99.70
4.75-5.00	30.77	49.02	67.37	96.43	99.81	100.00
5.00-5.25	38.12	42.73	65.66	96.80	100.00	100.00
5.25-5.50	35.41	46.58	66.26	97.68	100.00	100.00
5.50-6.00	37.97	46.31	68.81	95.83	99.85	99.89
6.00-7.00	40.48	50.33	66.90	94.47	99.91	99.94

profile obtained from the real data analysis, as shown in Figure 7.1. The  $z$  position in the target had the distribution of the probability of interaction in the target. The  $\pi^0$  was allowed to decay isotropically into two photons in its center-of-mass system. The photon conversion probability was determined according to the  $z$  position of the decay and its average was found to be about 13%. The converted photons were flagged for further analysis, and the photons which missed the calorimeter due to the geometry were also identified. A program, weighting each event by the production cross section, determined the geometric acceptance in the  $p_T$  and  $x_F$  bins by dividing the number of  $\pi^0$ 's (both photons) reaching the calorimeter by the total non-converting  $\pi^0$ 's. The result is listed in Table 8.8. The geometric acceptance for  $\eta$  is listed in Table 8.9.

It is clear that for a fixed  $x_F$  the acceptance increases with  $p_T$ . This is

*Table 8.9:  $\eta$  Geometric Acceptance (%)*

$p_T$	$x_F$					
	-0.2	-0.1	0.0	0.1	0.2	0.3
3.50–4.00	6.46	31.31	52.79	87.38	95.60	96.21
4.00–4.50	12.17	34.58	55.81	87.75	96.86	95.41
4.50–5.00	21.16	36.46	58.27	87.91	96.01	97.32
5.00–5.50	27.73	40.61	58.20	87.27	96.93	98.36
5.50–6.00	30.16	43.00	58.83	86.34	96.71	98.31
6.00–7.00	35.11	45.00	59.67	84.21	97.05	98.54

because with increasing  $p_T$ , the  $\pi^0$  energy increases and the opening angle between the two photons decreases, resulting in a smaller probability of losing one of the photons outside the detector. For a fixed  $p_T$ , larger  $x_F$  means larger energy, and smaller probability of losing one of the photons outside the detector. In addition, larger  $x_F$  implies the  $\pi^0$  will hit closer to the center of the detector and will be less likely to lose its photons beyond the out-edge of the detector. The rapid increase of the acceptance with  $x_F$  is the result of those two facts.

### 8.4.2 Reconstruction Efficiency

The photons reaching the calorimeter were showered through its materials using an EGS simulation. Their  $(x, y)$  positions were projected from the target to the front face of the calorimeter. The energy deposited in each glass block, as well as in the LGC, was stored in an array. Those events were analyzed by the same program used for real data, and the software

reconstruction efficiency, as well as the effect of each cut was derived.

One major difference between the Monte Carlo events and the real events was in treating the hodoscopes. It was difficult to simulate a shower development in the hodoscopes on a tube by tube basis. The treatment of the hodoscopes will be discussed in the following paragraphs.

In the GTH, the total charge accumulated depended on the energy deposited in the active converters. The correlation was studied using the calibration electrons, with the result shown in Figure 6.3. The expected charge in the GTH was deduced from the active converter energy according to this distribution. In order to account for the effect of some inactive tubes, the charge was distributed into tubes with the pulse shape determined from the calibration data (ref. Section 5.2). Any charge falling into an inactive tube was subtracted from the total charge. This was done for both  $x$  and  $y$  views. The resulting charges are used in the  $x$ - $y$  match-up. If the two photons are close together, it is likely that their showers will overlap in one or both views of the hodoscope. In the latter case, the showers cannot be resolved. In the former case, the charges in the overlapping view were added together, and the position was an energy-weighted average of the two showers. This posed difficulties in the  $x$ - $y$  match-ups. The one-to-two match-up might result in only one matched pair, and we would not be able to reconstruct the  $\pi^0$ .

The total shower energy deposited in the LGC was determined from the EGS simulation and did not depend on anything else. But the complication for the LGC came from the overflow of the ADC and the dependence of

the  $y$ -view energy on  $x$  position. The energy distributed in each tube was divided by the tube's (relative and plane) gains to convert back into ADC counts. If the counts exceeded the full range of the 12-bit ADC, the tube was tagged. If there was more than one overflowing tube within five tubes, the event was discarded as was done in the real data analysis. If there were not any other overflowing tubes in the vicinity, a fit to the sidebands gave the ADC value of the overflowing central tube. The ADC was then converted back into energy. The  $y$ -view energy was multiplied by the  $x$ -dependence function as illustrated in Figure 4.3.

The average energy in the LGC region was higher than that in the GTH region. The photon opening angle was smaller in LGC region, resulting in bigger losses due to the inefficiency of resolving the showers. This is evident in the reconstruction efficiency listed in  $p_T$  and  $x_F$  bins in Table 8.10. The ADC overflow also contributed to the losses.

In order to verify the simulation procedure, the reconstructed mass from the Monte Carlo events were checked against those from the real events. Figure 8.4 shows the comparison of the mass and two photon energy asymmetry distributions. They are in good agreement.

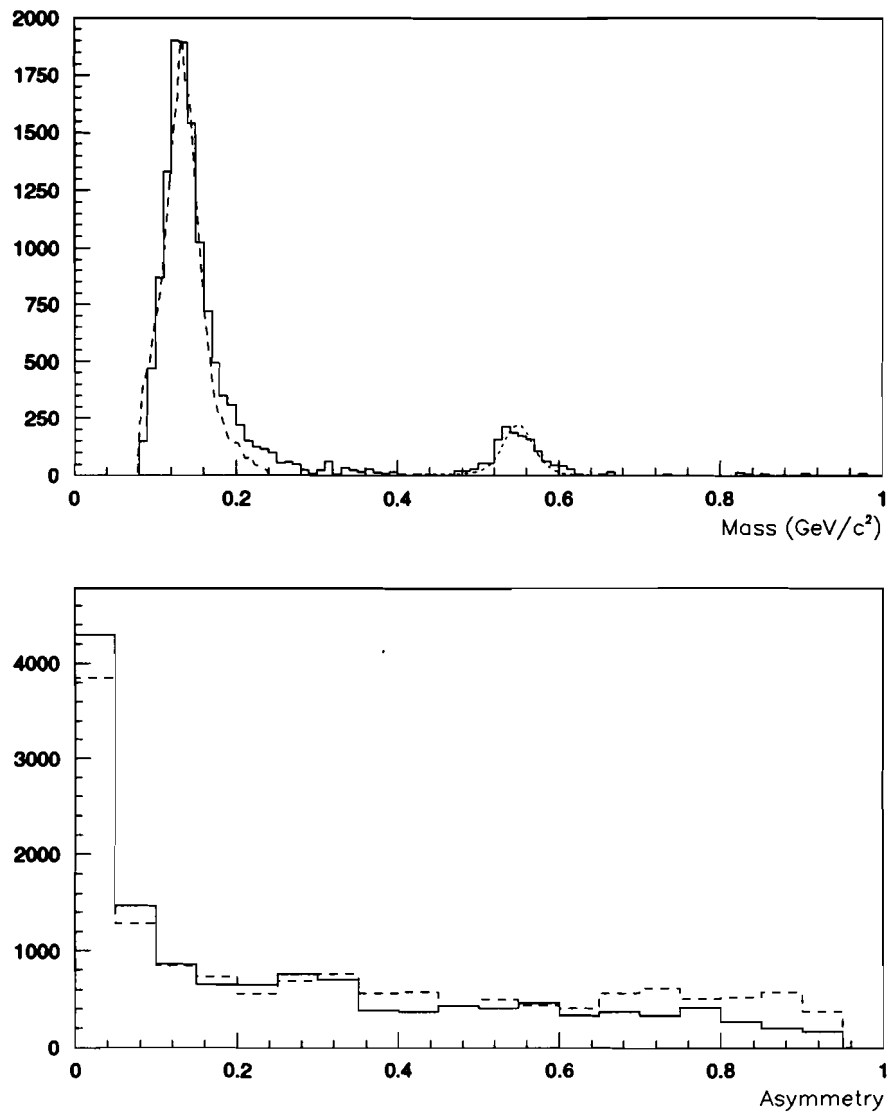
The largest uncertainty from the simulation procedure was the event migration from one  $p_T$  bin to its neighboring  $p_T$  bins because of the resolutions put into the Monte Carlo program to smear the energy and position. Due to the nature of the fast fall-off of the cross section with increasing  $p_T$ , there will be a lot more events going into a high  $p_T$  bin from a low  $p_T$  bin than

Table 8.10:  $\pi^0$  Reconstruction Efficiency (%)

$p_T$	$x_F$					
	-0.2	-0.1	0.0	0.1	0.2	0.3
3.50–3.75	19.60	21.94	19.49	16.70	14.74	9.15
3.75–4.00	17.26	21.19	18.68	16.86	16.37	10.75
4.00–4.25	17.86	20.26	17.66	17.33	16.54	10.94
4.25–4.50	21.41	19.97	17.87	16.69	16.35	10.79
4.50–4.75	20.41	18.45	18.49	15.47	15.49	10.13
4.75–5.00	16.66	15.09	16.22	15.91	13.29	9.69
5.00–5.25	15.77	15.07	16.04	14.74	12.54	9.04
5.25–5.50	15.56	13.18	14.01	15.24	11.12	8.97
5.50–6.00	14.86	13.22	12.69	13.81	10.38	8.11
6.00–7.00	12.01	11.79	12.63	11.26	9.11	6.01

Table 8.11:  $\eta$  Reconstruction Efficiency (%)

$p_T$	$x_F$					
	-0.2	-0.1	0.0	0.1	0.2	0.3
3.50–4.00	6.70	8.03	15.07	20.63	17.75	18.27
4.00–4.50	13.72	20.37	24.54	21.36	18.59	21.32
4.50–5.00	20.11	26.71	26.77	21.39	19.13	20.66
5.00–5.50	25.25	28.05	27.61	22.57	18.55	19.20
5.50–6.00	25.25	25.79	25.40	22.23	17.79	18.64
6.00–7.00	24.19	24.14	24.97	20.01	18.40	16.38



*Figure 8.5: Comparison of real data and Monte Carlo events. The solid histograms are the results from real data, and the dashed lines are the results from the Monte Carlo simulation. Top):  $\gamma\text{-}\gamma$  invariant mass (a  $\pi^0$  peak and an  $\eta$  peak); Bottom): Two photon energy asymmetry.*

vice versa. That was the reason that there were events generated outside of the  $p_T$  and  $x_F$  bounds of our data ( $3.5 \leq p_T \leq 7.5$ ,  $-0.25 \leq x_F \leq 0.35$ ). The average error from this simulation on the cross section calculation was about 10%, and was counted as one of the systematical errors.

The same procedure was applied to  $\eta$  as well. The reconstruction efficiencies of the  $\eta$  are listed in Tables 8.11.

# Chapter 9

## Results and Conclusions

### 9.1 formulation

The invariant differential cross section for the inclusive  $\pi^0$  and  $\eta$  production can be expressed as [34]

$$E \frac{d^3\sigma}{dp^3} = \kappa \frac{A^\alpha}{N_A N_B \lambda (1 - e^{-\rho l / \lambda})} \frac{\sqrt{x_T^2 + x_F^2}}{p_T \Delta p_T \Delta x_F \Delta \phi} N^{meson}(p_T, x_F). \quad (9.1)$$

where  $N_A$  is the Avogadro's number, and  $N_B$  is the number of live beam particles.  $A$ ,  $\rho$ ,  $l$ , and  $\lambda$  are the atomic number, the density (in g/cm<sup>2</sup>), the length (in cm), and the interaction length (in cm) of the experiment target, respectively.  $\alpha$  is the nuclear dependence parameter for the total absorption cross section of  $\pi N$ (nucleon) interaction, and is taken to be 0.755, 0.751, and 0.718 for  $\pi^-$ ,  $\pi^+$ , and proton beams respectively [40].  $\phi$  is the azimuthal angle.  $x_T$  and  $x_F$  are defined in terms of the transverse momentum  $p_T$ , longitudinal momentum in the  $\pi N$  center-of-mass system  $p_z$ , and the total

energy of system  $\sqrt{s}$ :

$$x_T = \frac{2p_T}{\sqrt{s}}, \quad x_F = \frac{2p_z}{\sqrt{s}}. \quad (9.2)$$

$\kappa$  is the nuclear dependence for the single meson inclusive production, and is equal to  $A^{1.1}$  [41].  $N^{meson}(p_T, x_F)$  is the number of mesons in each  $p_T$  and  $x_F$  bin:

$$N^{meson}(p_T, x_F) = \frac{\sum_i S_i N_i(p_T, x_F)}{(\text{trigger eff.})(\text{acceptance})(\text{reconstruction eff})}, \quad (9.3)$$

where  $N_i$  is the number of the reconstructed mesons in trigger level  $i$ , and  $S_i$  is the prescale factor of that trigger level. This number is further corrected by the trigger efficiency, the detector geometric acceptance, and the software reconstruction efficiency.

A  $\pi^0$  is counted if the  $\gamma$ - $\gamma$  invariant mass falls between 80 and 240 MeV/c<sup>2</sup>, and an  $\eta$  is counted if the  $\gamma$ - $\gamma$  invariant mass falls between 480 and 620 MeV/c<sup>2</sup>. The side bands around the meson peaks are used to estimate the background under the peaks.

## 9.2 $\pi^0$ Cross Section

The invariant cross sections of the inclusive  $\pi^0$  production by  $\pi^+$  and  $\pi^-$  beams were measured in the  $p_T$  range of 3.5–7.0 GeV/c and the  $x_F$  range of  $-0.25$ – $0.35$ . For the proton beam, there were few events (some bins in  $p_T$  did not have any entry) in the  $x_F$  range of  $-0.25 \leq x_F \leq -0.15$ , so the kinematic region for the proton beam was reduced to  $3.5 \leq p_T \leq 7.0$  and

Table 9.1: Inclusive Cross Section of  $\pi^- + Li \rightarrow \pi^0 + X$ , in pbarn.

$p_T$	$x_F$					
	-0.2	-0.1	0.0	0.1	0.2	0.3
3.61	3547 ± 799	3606 ± 350	5941 ± 409	9479 ± 570	7764 ± 627	4972 ± 668
3.86	2202 ± 367	2776 ± 257	3317 ± 250	4769 ± 282	3029 ± 279	1948 ± 318
4.11	878 ± 156	1327 ± 147	1332 ± 138	1856 ± 145	1786 ± 170	1295 ± 190
4.36	482 ± 89	465 ± 75	675 ± 87	766 ± 82	753 ± 97	668 ± 106
4.61	191 ± 43	310 ± 50	374 ± 56	405 ± 55	206 ± 53	294 ± 68
4.86	161 ± 43	135 ± 26	141 ± 31	154 ± 28	141 ± 27	106 ± 40
5.11	83 ± 19	95 ± 20	54 ± 9	93 ± 13	87 ± 15	82 ± 22
5.36	42 ± 11	50 ± 11	40 ± 9	30 ± 4	39 ± 6	57 ± 19
5.71	12.4 ± 3.1	19.4 ± 4.8	17.2 ± 3.5	15.1 ± 3.4	15.9 ± 4.2	7.0 ± 2.5
6.38	4.8 ± 1.5	3.0 ± 1.1	3.1 ± 1.0	3.1 ± 1.1	1.4 ± 0.6	1.1 ± 1.0

Table 9.2: Inclusive Cross Section of  $\pi^+ + Li \rightarrow \pi^0 + X$ , in pbarn.

$p_T$	$x_F$					
	-0.2	-0.1	0.0	0.1	0.2	0.3
3.61	680 ± 680	6089 ± 1047	7093 ± 1026	12547 ± 1537	6871 ± 1390	3728 ± 1572
3.86	2834 ± 813	1803 ± 334	2223 ± 375	4544 ± 556	3457 ± 567	1236 ± 512
4.11	670 ± 307	1278 ± 220	1623 ± 261	2087 ± 303	2100 ± 331	1066 ± 324
4.36	424 ± 140	356 ± 119	1073 ± 188	625 ± 168	782 ± 198	741 ± 239
4.61	248 ± 96	381 ± 91	445 ± 106	291 ± 90	109 ± 93	109 ± 86
4.86	133 ± 54	284 ± 85	150 ± 61	140 ± 41	242 ± 80	87 ± 86
5.11	62 ± 27	130 ± 43	132 ± 34	74 ± 22	97 ± 38	71 ± 43
5.36	23 ± 15	7 ± 6	38 ± 16	35 ± 14	69 ± 31	83 ± 40
5.71	22.5 ± 10.9	20.8 ± 9.1	8.5 ± 4.3	10.8 ± 3.7	4.6 ± 2.2	17.3 ± 10.0
6.38	4.6 ± 4.2	9.1 ± 4.7	2.0 ± 0.9	3.2 ± 0.9	1.7 ± 0.8	2.6 ± 1.3

Table 9.3: Inclusive Cross Section of  $p + Li \rightarrow \pi^0 + X$ , in pbarn.

$p_T$	$x_F$				
	-0.1	0.0	0.1	0.2	0.3
3.61	5384 $\pm$ 1532	5405 $\pm$ 1358	8228 $\pm$ 1799	4545 $\pm$ 1788	3816 $\pm$ 1958
3.86	2783 $\pm$ 459	3190 $\pm$ 388	2273 $\pm$ 383	2431 $\pm$ 403	1060 $\pm$ 389
4.11	1011 $\pm$ 181	1408 $\pm$ 200	1124 $\pm$ 172	399 $\pm$ 158	290 $\pm$ 114
4.36	374 $\pm$ 94	437 $\pm$ 101	688 $\pm$ 114	211 $\pm$ 88	423 $\pm$ 121
4.61	192 $\pm$ 54	315 $\pm$ 69	367 $\pm$ 67	126 $\pm$ 45	51 $\pm$ 46
4.86	61 $\pm$ 28	104 $\pm$ 41	76 $\pm$ 30	92 $\pm$ 47	36 $\pm$ 31
5.11	101 $\pm$ 37	40 $\pm$ 18	14 $\pm$ 9	18 $\pm$ 14	1 $\pm$ 2
5.36	21 $\pm$ 13	9 $\pm$ 8	11 $\pm$ 7	9 $\pm$ 4	24 $\pm$ 18
5.71	17.4 $\pm$ 9.7	5.9 $\pm$ 3.9	2.1 $\pm$ 1.0	2.0 $\pm$ 1.0	1.5 $\pm$ 1.1
6.38	0.6 $\pm$ 0.4	0.9 $\pm$ 0.5	0.2 $\pm$ 0.2	1.2 $\pm$ 0.5	0.0 $\pm$ 0.0

Table 9.4: Parameters of the Phenomenological Fit.

	C(mb/GeV <sup>2</sup> )	n	m	$x_0$	$\chi^2/d.o.f$
$\pi^-$ beam					
Value $\pm$ stat.err	34.5 $\pm$ 9.0	3.56 $\pm$ 0.40	10.86 $\pm$ 0.29	0.098 $\pm$ 0.010	2.9
Correlation	C	-0.711	0.946	0.317	
Coefficients	n		-0.899	-0.484	
	m			0.408	
$\pi^+$ beam					
Value $\pm$ stat.err	33.4 $\pm$ 17.8	4.25 $\pm$ 0.83	10.56 $\pm$ 0.61	0.082 $\pm$ 0.016	1.9
Correlation	C	-0.778	0.957	0.300	
Coefficients	n		-0.925	-0.379	
	m			0.345	
proton beam					
Value $\pm$ stat.err	150.5 $\pm$ 126.3	6.70 $\pm$ 1.27	11.09 $\pm$ 0.93	0.019 $\pm$ 0.017	1.8
Correlation	C	-0.767	0.957	-0.447	
Coefficients	n		-0.919	0.618	
	m			-0.543	

$-0.15 \leq x_F \leq 0.35$ . The cross sections are listed in Tables 9.1–9.3, in  $p_T$  and  $x_F$  bins. The  $\pi^\pm$  and  $p$  beam data were each fit to the phenomenological form,

$$E \frac{d^3\sigma}{dp^3} = C \frac{(1 - x_D)^n}{p_T^m} \quad (9.4)$$

where

$$x_D = \sqrt{x_T^2 + (x_F - x_0)^2}. \quad (9.5)$$

The fit parameters are listed in Table 9.4. From the coefficients listed in the table, it is clear that those parameters are highly correlated, in particular,  $C$  and  $m$ , and  $m$  and  $n$ .

### 9.2.1 $\pi^+$ and $\pi^-$ Beams

Figure 9.1 shows the  $\pi^0$  cross section  $\sigma(\pi^- + Li \rightarrow \pi^0 + X)$  as a function of  $p_T$ . Each point on the plot is averaged over the six  $x_F$  bins. The first 8 data points span equal intervals in the  $p_T$  range from 3.5 to 5.5 GeV/c, and the last two points cover  $p_T$  ranges from 5.5 to 6.0 and from 6.0 to 7.0 GeV/c. The similar plot for  $\pi^+$  beam is shown in Figure 9.2.

Since the  ${}^7\text{Li}$  was nearly an isoscalar target, it was expected that the  $\pi^0$  cross sections from  $\pi^+\text{Li}$  and  $\pi^-\text{Li}$  interaction are the same, by the isospin argument. The  $\pi^0$  cross sections by the  $\pi^\pm$  beams are superimposed in Figure 9.3. The cross sections are equal within statistical errors. The ratio of these two cross sections is shown in Figure 9.4 as a function of  $p_T$ . A fit

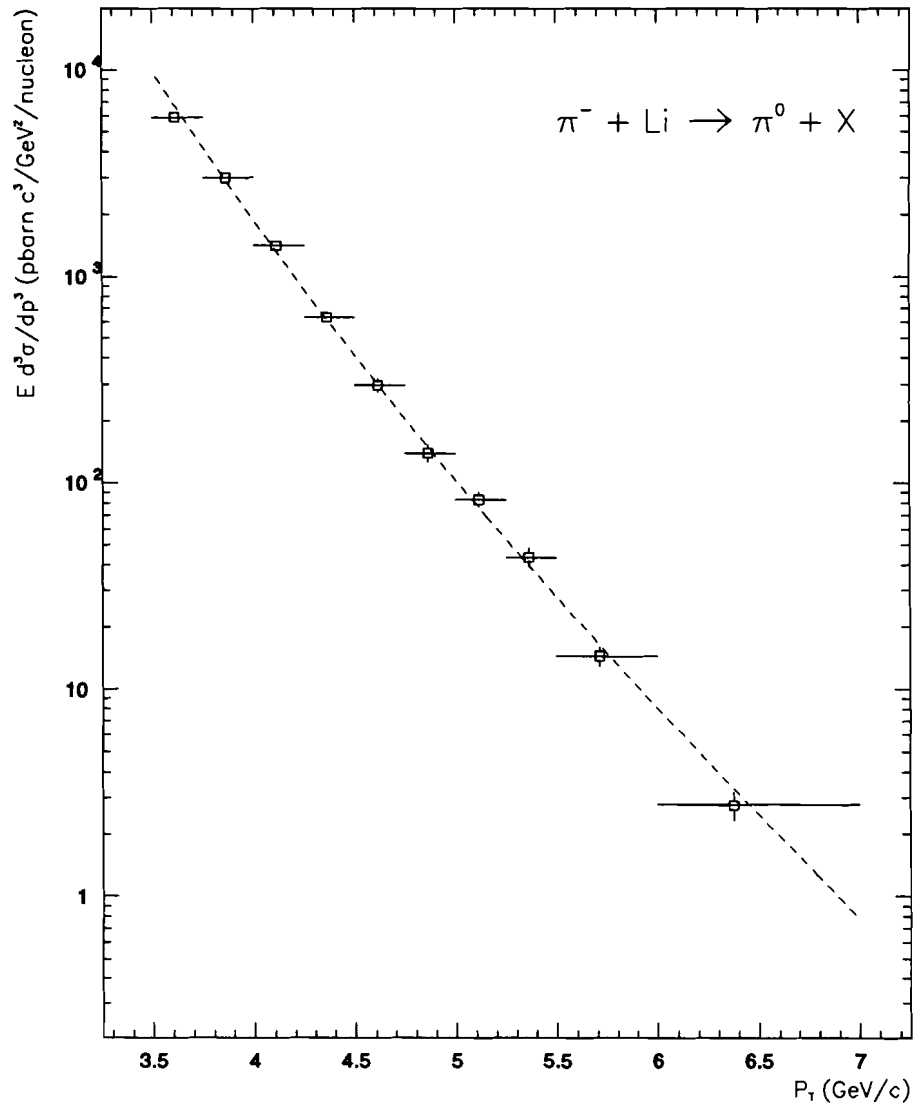


Figure 9.1: Invariant cross section  $\sigma(\pi^- + Li \rightarrow \pi^0 + X)$  as a function of  $p_T$  averaged over the entire  $x_F$  range. The dashed curve represents the fit.

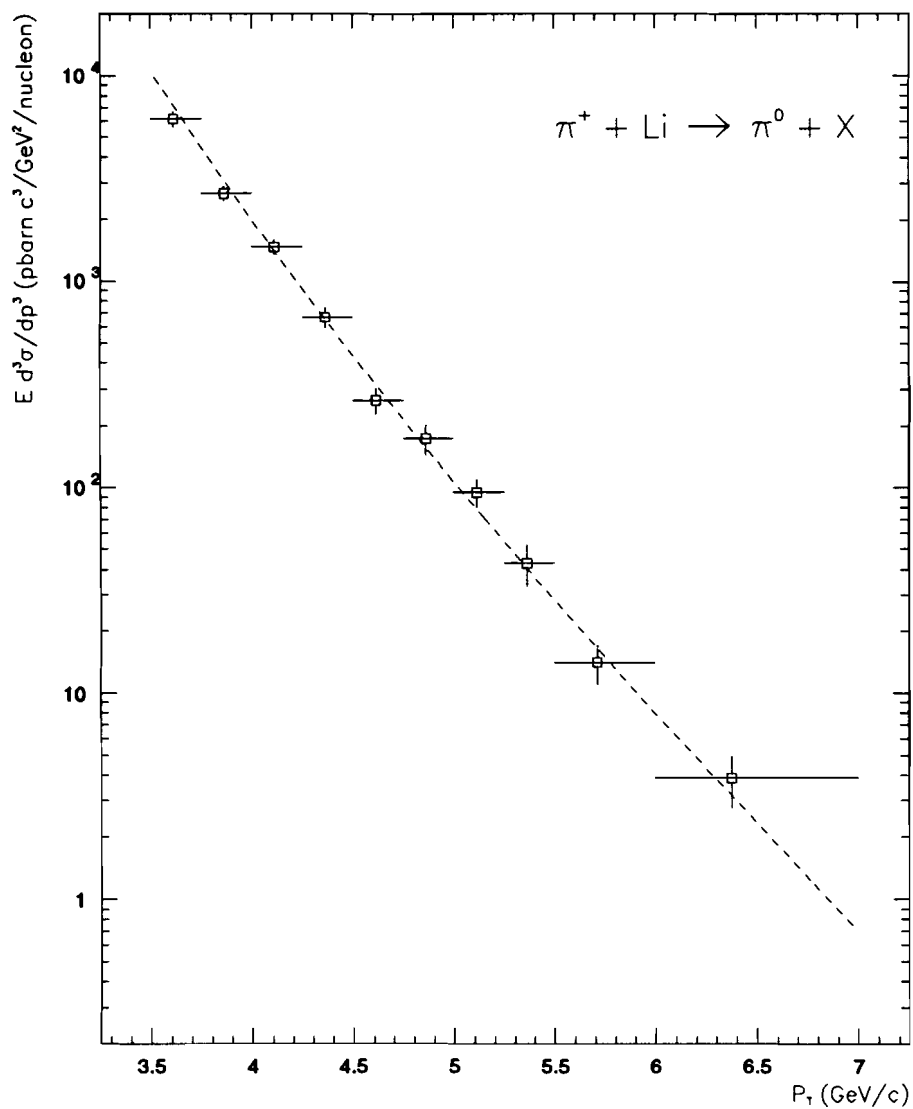


Figure 9.2: Invariant cross section  $\sigma(\pi^+ + \text{Li} \rightarrow \pi^0 + X)$  as a function of  $p_T$  averaged over the entire  $x_F$  range. The dashed curve represents the fit.

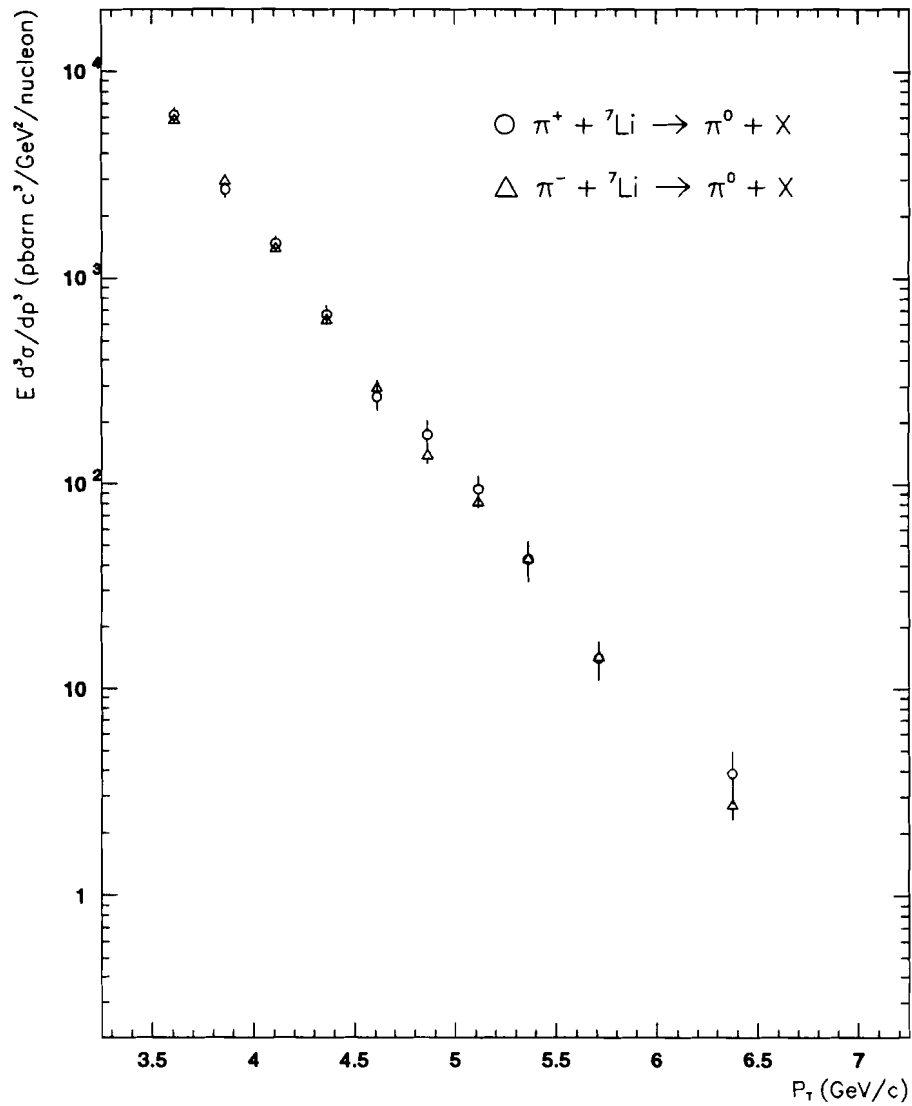


Figure 9.3: Invariant cross section  $\sigma(\pi^\pm + \text{Li} \rightarrow \pi^0 + X)$  as a function of  $p_T$  averaged over the entire  $x_F$  range.

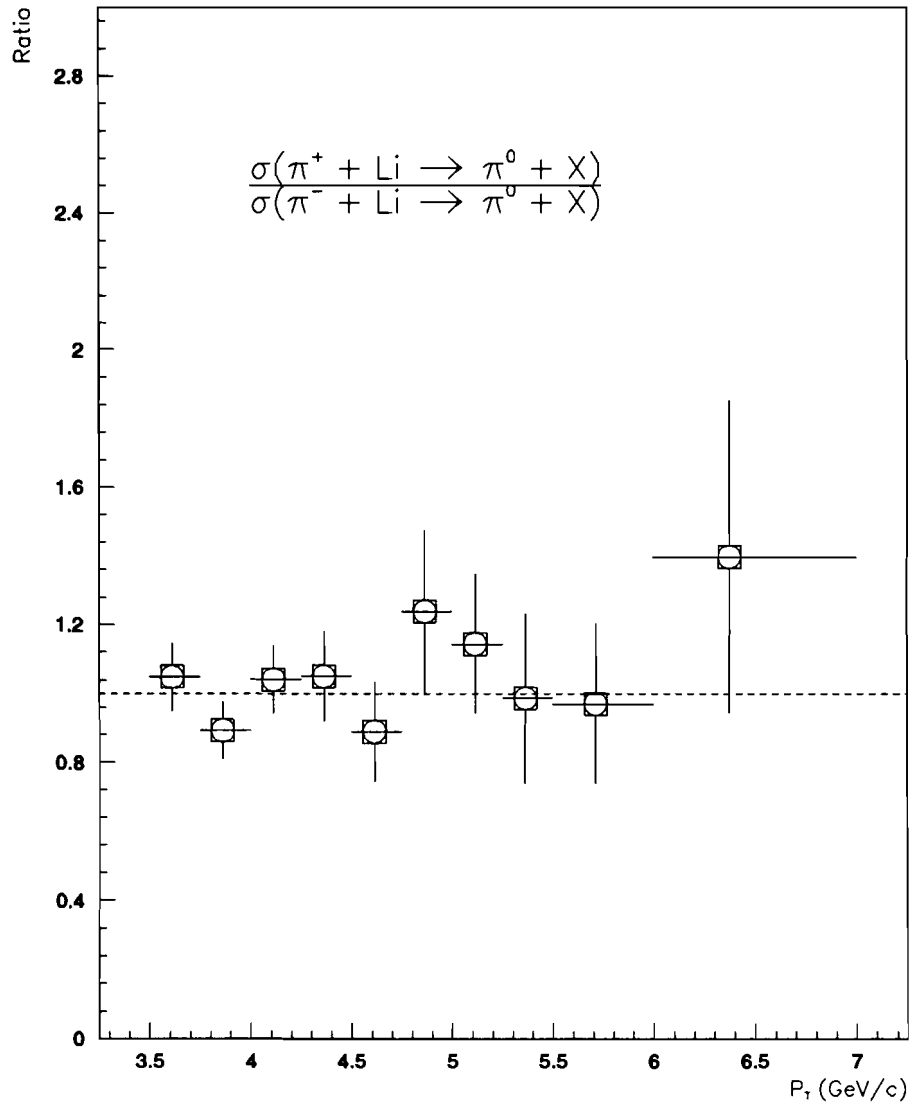


Figure 9.4: Ratio of  $\pi^0$  invariant cross sections  $\sigma(\pi^+ + Li \rightarrow \pi^0 + X)/\sigma(\pi^- + Li \rightarrow \pi^0 + X)$  as a function of  $p_T$ . The dashed curve is a fit to a horizontal line.

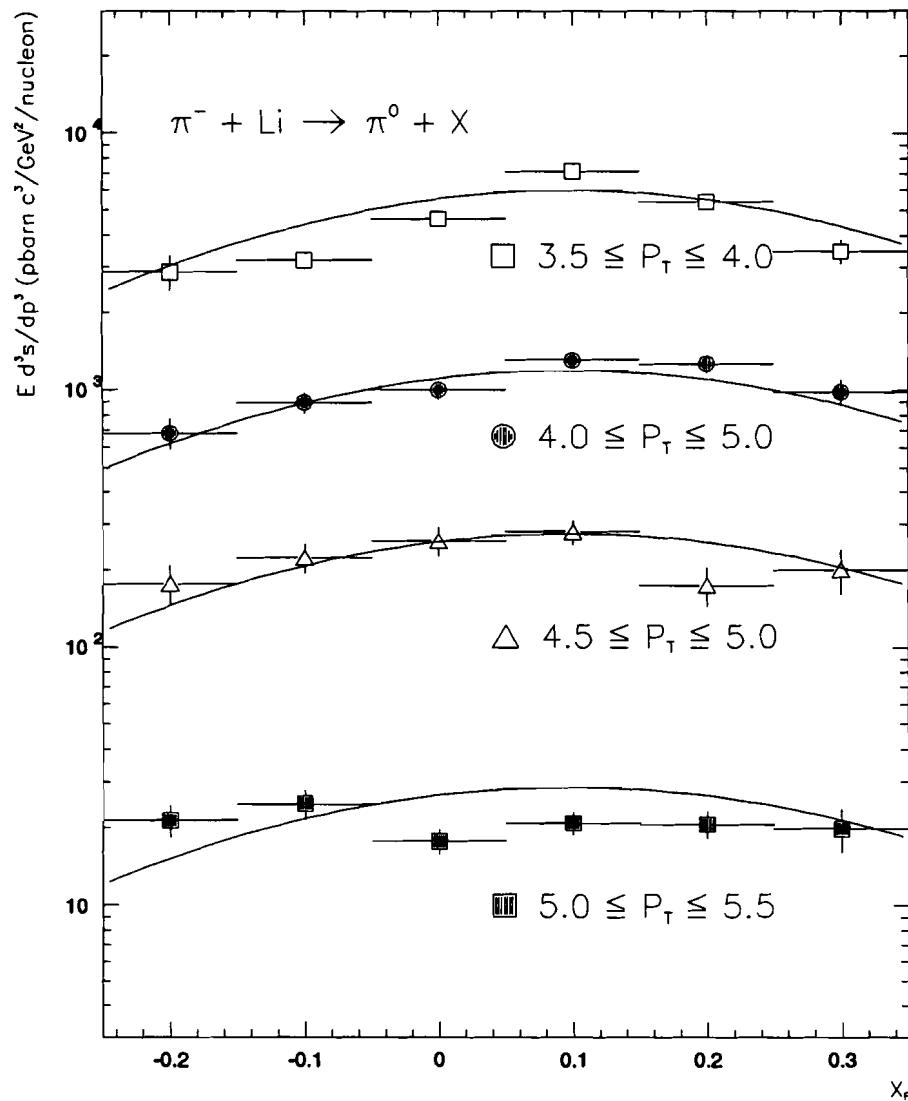


Figure 9.5: Invariant cross section  $\sigma(\pi^- + \text{Li} \rightarrow \pi^0 + X)$  as a function of  $x_F$  in four  $p_T$  ranges. The curves are from the fit.

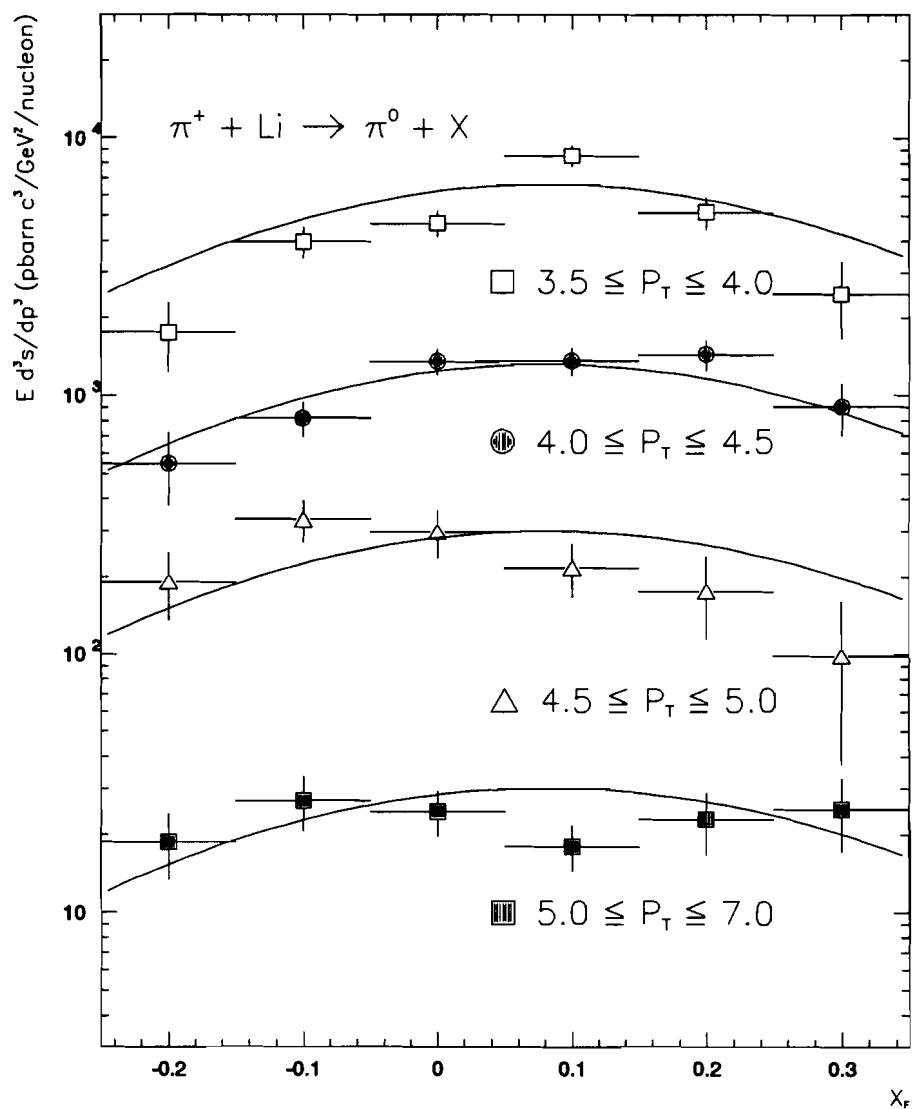


Figure 9.6: Invariant cross section  $\sigma(\pi^+ + \text{Li} \rightarrow \pi^0 + X)$  as a function of  $x_F$  in four  $p_T$  ranges. The curves are from the fit.

to a horizontal line yielded

$$R = \frac{\sigma(\pi^+ + Li \rightarrow \pi^0 + X)}{\sigma(\pi^+ + Li \rightarrow \pi^0 + X)} = 1.001 \pm 0.043.$$

The  $\pi^0$  production angle in the center-of-mass system can be represented by the Feynman  $x_F$ , for a fixed  $p_T$ . Figures 9.5–9.6 show the  $\pi^0$  cross sections as functions of  $x_F$  in different  $p_T$  intervals. It is clear that the distributions from the  $\pi^-$  and  $\pi^+$  beams have the same shape, and their peaks shift towards the positive  $x_F$ . This behavior can be explained as follows.

In the  $\pi N$  center-of-mass system, the pion and nucleon have the same momenta. From the quark model, it is known that pions have two valence quarks, while nucleons have three. On average, a quark in the pion will have higher momentum than a quark in the nucleon (it is also said the pion quark is harder than the nucleon quark). So the  $\pi^0$  is produced more forward in  $\pi N$  interactions, and its  $x_F$  calculated in the  $\pi N$  CMS will shift toward the positive side.

### 9.2.2 Proton Beam

From the same argument, quarks in the nucleons will have less average accessible momentum than those in the pions. So the cross section falls off faster with increasing  $p_T$  in  $pN$  interactions than in  $\pi N$  interactions. Figure 9.7 is the  $\pi^0$  cross section as a function of  $p_T$  for  $pLi$  interactions. A ratio of

$$\frac{\sigma(\pi^+ + Li \rightarrow \pi^0 + X)}{\sigma(p + Li \rightarrow \pi^0 + X)}$$

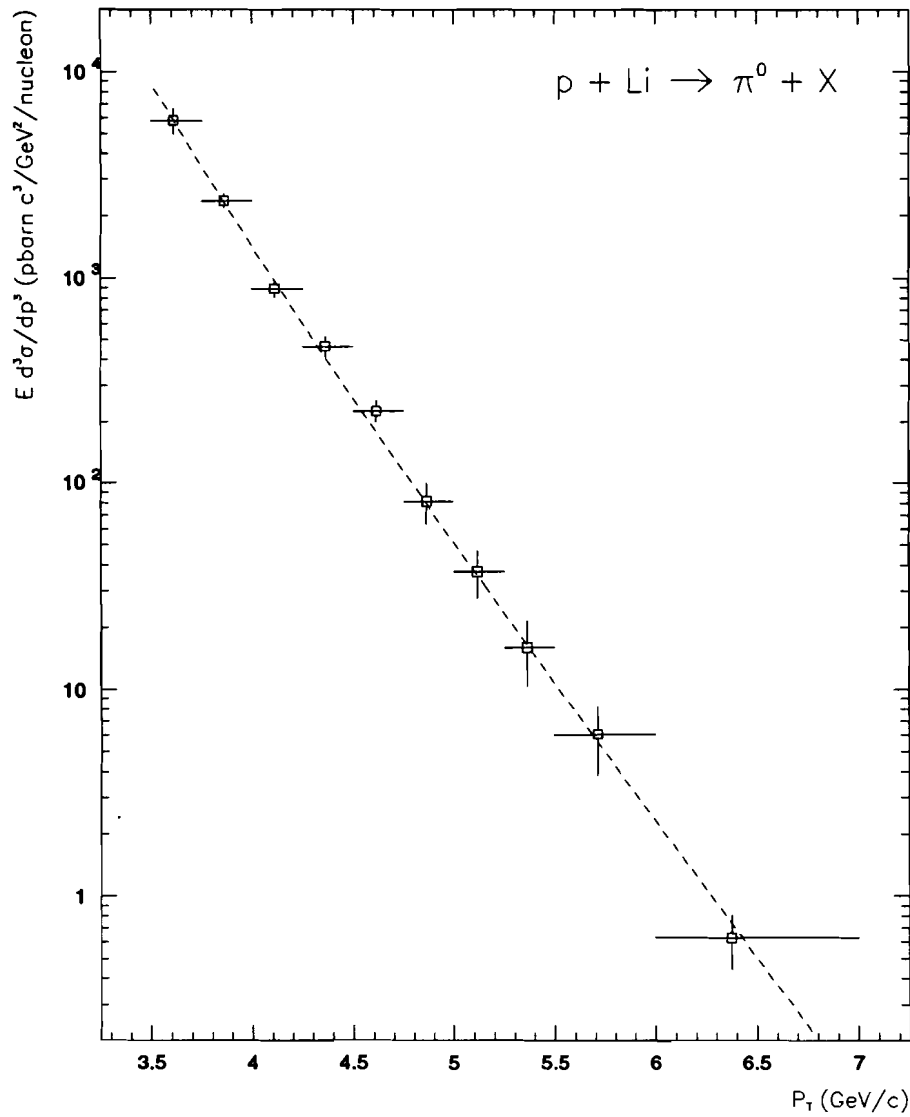


Figure 9.7: Invariant cross section  $\sigma(p + Li \rightarrow \pi^0 + X)$  as a function of  $p_T$  averaged over the entire  $x_F$  range (-0.15-0.35)

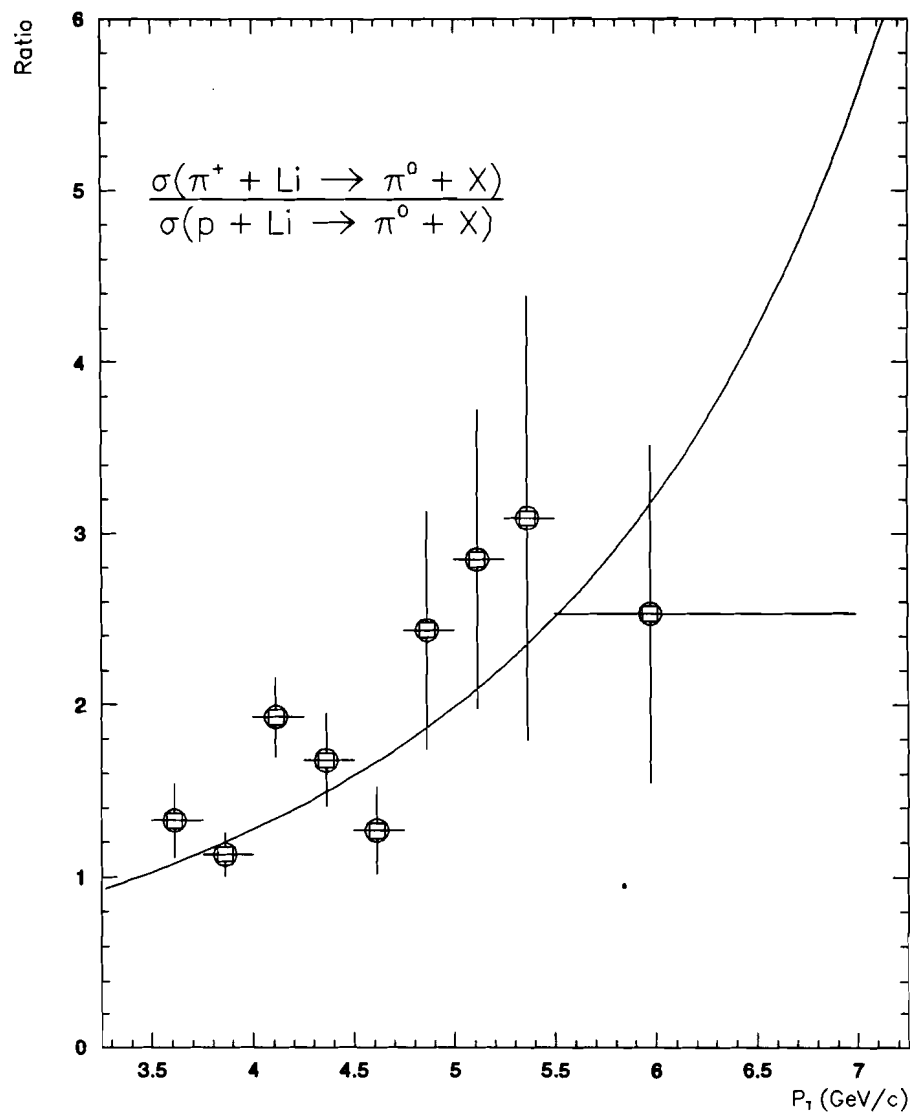


Figure 9.8: Ratio of  $\pi^0$  invariant cross sections  $\sigma(\pi^+ + Li \rightarrow \pi^0 + X)/\sigma(p + Li \rightarrow \pi^0 + X)$  as a function of  $p_T$ . The curve is from the division of the curve shown in Figure 9.2 by the curve shown in Figure 9.7.

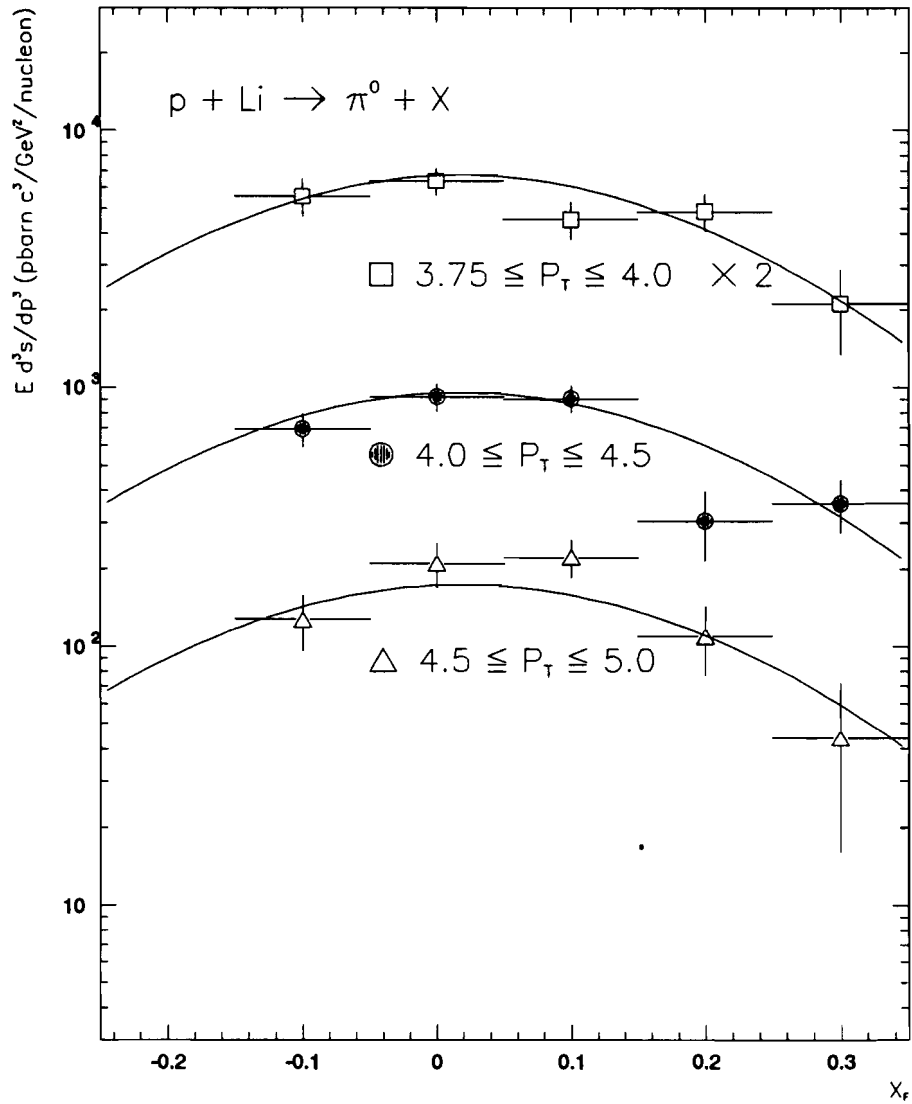


Figure 9.9: Invariant cross section  $\sigma(p + Li \rightarrow \pi^0 + X)$  as a function of  $x_F$  in three  $p_T$  ranges. The curves are from the fit.

is shown in Figure 9.8, the curve represents the division of the fits of the  $\pi^+$  data and the proton data. The general trend is in agreement with the parton model and with other experimental results from CERN NA3[21] and WA70[35].

The  $x_F$  distribution of the  $\pi^0$  cross section by the proton beam is shown in Figure 9.9. In  $pp$  interactions, it is expected that the  $x_F$  distribution will peak at  $x_0 = 0$ . The fitted value from our experiment is  $x_0 = 0.019 \pm 0.017$ . This non-zero value could come from some nuclear effect. The first  $p_T$  bin ( $3.5 \leq p_T < 3.75$  GeV/c) was not used in the fit due the low statistics (ref. Section 8.2.3)

### 9.2.3 Systematic Errors

The systematic errors on the cross sections came from several sources:

1. Beam normalization: 3.7%, 2.6%, and 2.7% for  $\pi^-$ ,  $\pi^+$ , and proton beams, respectively.
2.  $p_T$  scale uncertainty of 1%, resulting in a 12% error in cross section.
3. Uncertainty in background subtraction, contributing 8%.
4. Energy smearing used in the Monte Carlo program to estimate the reconstruction efficiency, giving 10% error.
5. Error in the trigger efficiency due to photo-tube gain shift, making 10% error in the cross section.

Adding these errors in quadrature yields an estimated total systematic error of 20.5% for all beam types.

All of the systematic errors listed above, except number 3, applies to the  $\eta$  production as well. The uncertainty in the background subtraction for  $\eta$  was about 4%.

### 9.3 $\eta$ Cross Sections

As discussed in Chapter 1,  $\pi^0$  and  $\eta$  are both pseudoscalars, but their valence quark components are different. the  $\pi^0$  is made of  $u$  and  $d$  quarks, while the  $\eta$  has  $u$ ,  $d$ , and  $s$  quarks in it. The observed  $\eta$  is the mixture of the octet eigenstate  $\eta_8$  and the singlet eigenstate  $\eta_0$ :

$$\eta = \eta_8 \cos \theta + \eta_0 \sin \theta, \quad (9.6)$$

with mixing angle of about  $11^\circ$ . Both mesons are produced by the same type of nonstrange quarks (in  $\pi N$  interaction), so the same structure functions and matrix elements (ref Section 1.2) are involved in both productions. In the high  $p_T$  region,  $\pi^0$  and  $\eta$  are the leading fragments of the scattering partons and are produced near  $z = 1$ . Thus their ratio should be proportional to the fragmentation functions of  $u$  and  $d$  quarks to  $\pi^0$  and  $\eta$  at large  $z$ , and it should reflect the mixing of  $\eta_8$  and  $\eta_0$ [20].

$$R = \eta/\pi^0 \approx \frac{D_{\eta/q}(z_q)}{D_{\pi^0/q}(z_q)} = \frac{\langle q\bar{q}|\eta \rangle^2}{\langle q\bar{q}|\pi^0 \rangle^2},$$

where  $q$  stands for the available  $u$  and  $d$  quarks. The  $\eta$  to  $\pi^0$  ratio is expected to be around 0.5[42].

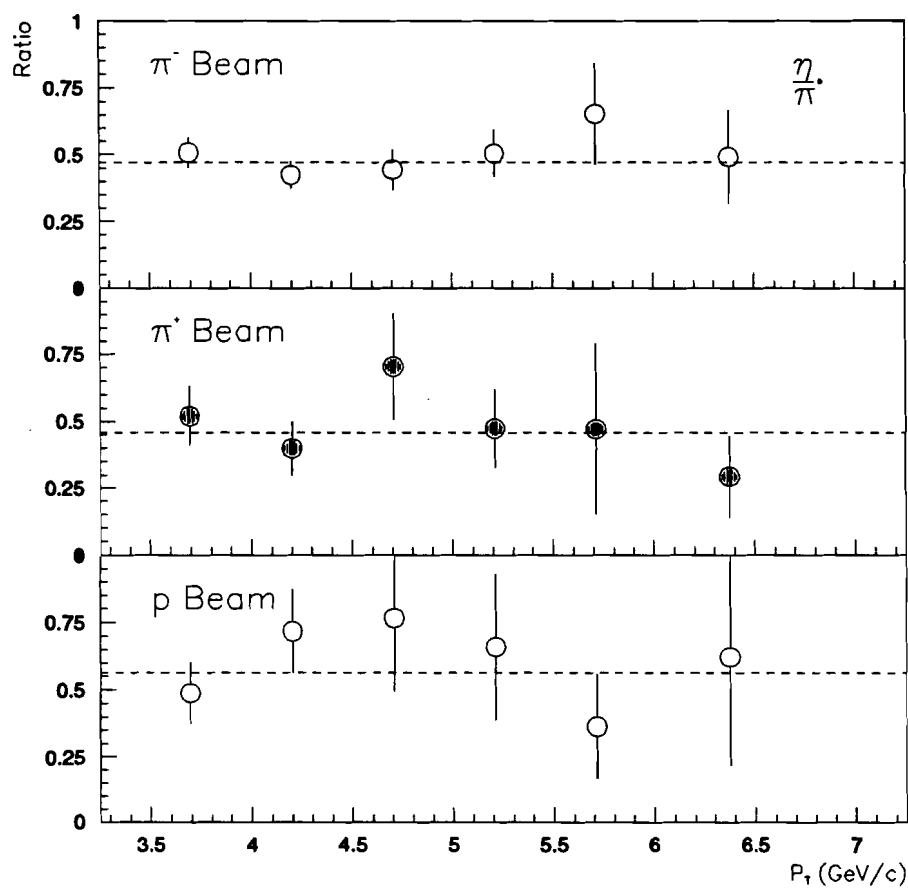


Figure 9.10: Ratio of  $\eta$  and  $\pi^0$  invariant cross sections  $\sigma(\pi^\pm, p + Li \rightarrow \eta + X)/\sigma(\pi^\pm, p + Li \rightarrow \pi^0 + X)$  as a function of  $p_T$ . The top graph is for  $\pi^-$  beam, the middle is for  $\pi^+$  beam, and the bottom plot is for  $p$  beam. Only the statistical errors are shown.

Table 9.5:  $\eta$  Cross Section in pbarn, averaged over  $x_F$  range of  $-0.15-0.35$ .

$p_T$	Beams		
	$\pi^-$	$\pi^+$	p
3.5-4.0	$2426.4 \pm 258.8$	$2518.4 \pm 503.6$	$2077.1 \pm 437.4$
4.0-4.5	$462.2 \pm 53.4$	$464.5 \pm 114.4$	$438.6 \pm 88.6$
4.5-5.0	$100.5 \pm 16.2$	$156.0 \pm 39.7$	$97.5 \pm 32.4$
5.0-5.5	$31.7 \pm 4.9$	$34.4 \pm 9.4$	$16.4 \pm 5.8$
5.5-6.0	$9.7 \pm 2.6$	$5.8 \pm 3.7$	$2.1 \pm 0.8$
6.0-7.0	$1.2 \pm 0.3$	$1.1 \pm 0.5$	$0.4 \pm 0.2$

The differential cross section of  $\eta$  production was measured in our experiment using  $\pi^\pm$  and proton beams. The cross section (averaged over the  $x_F$  range of  $-0.15-0.35$ ) is tabulated in  $p_T$  bins in Table 9.6. The ratio of

$$R = \frac{\sigma(\pi^\pm, p + Li \rightarrow \eta + X)}{\sigma(\pi^\pm, p + Li \rightarrow \pi^0 + X)}$$

is plotted in Figure 9.10 for our  $\pi^\pm$  and  $p$  beams. There is no apparent  $p_T$  dependence in those ratios. A straight line fit to the data points yields:

$$R = 0.471 \pm 0.031, \quad \text{for } \pi^- \text{ beam;}$$

$$R = 0.457 \pm 0.057, \quad \text{for } \pi^+ \text{ beam.}$$

$$R = 0.562 \pm 0.074, \quad \text{for } p \text{ beam.}$$

The errors are statistical. Most of the systematic errors cancel out in these ratios. The largest remaining systematic error came from the uncertainty of the  $\pi^0$  and the  $\eta$  background. This gave the systematic error of 9% on these ratios.

WA70[36] gave comparable results of  $R = 0.48 \pm 0.02 \pm 0.04$ ,  $R = 0.44 \pm 0.02 \pm 0.04$  and  $R = 0.45 \pm 0.04 \pm 0.04$  for  $\pi^-p$ ,  $\pi^+p$  and  $pp$  interactions, respectively. UA6[37] published its results of  $R = 0.482 \pm 0.040$  in  $pp$  interactions of  $\sqrt{s} = 24.3$  GeV. An early Fermilab fixed target experiment[38] reported  $R = 0.44 \pm 0.05$  for pion and proton induced reactions at beam momenta of 100, 200, and 300 GeV/c.

## 9.4 Comparison with Other Experiments

There were several recent experiments, NA3[21], WA70[22], and NA24[39], that have published their results on high  $p_T$   $\pi^0$  production using the same types of beams. Figure 9.11-9.13 plot the  $\pi^0$  cross section as a function of  $p_T$  from those experiments along with that of our experiment. The errors shown are statistical only. All four experiment gave the same trend of the  $p_T$  dependence. NA24 data agrees very well with our data, while the cross sections from NA3 and WA70 are lower. This is, at least partly, because the experiments ran at different energies. NA24 had the same center-of-mass energy of  $\sqrt{s} = 23.75$  GeV as E705, while WA70 ran at  $\sqrt{s} = 22.9$  GeV and NA3 at  $\sqrt{s} = 19.4$  GeV. In order to compare the data taken at different  $\sqrt{s}$ , it is better to use the variable  $x_T$ . Figures 9.14–16 show the  $x_T$  dependence of the cross sections multiplied by  $p_T^m$  ( $m$  came from the fit in Equation 9.4).

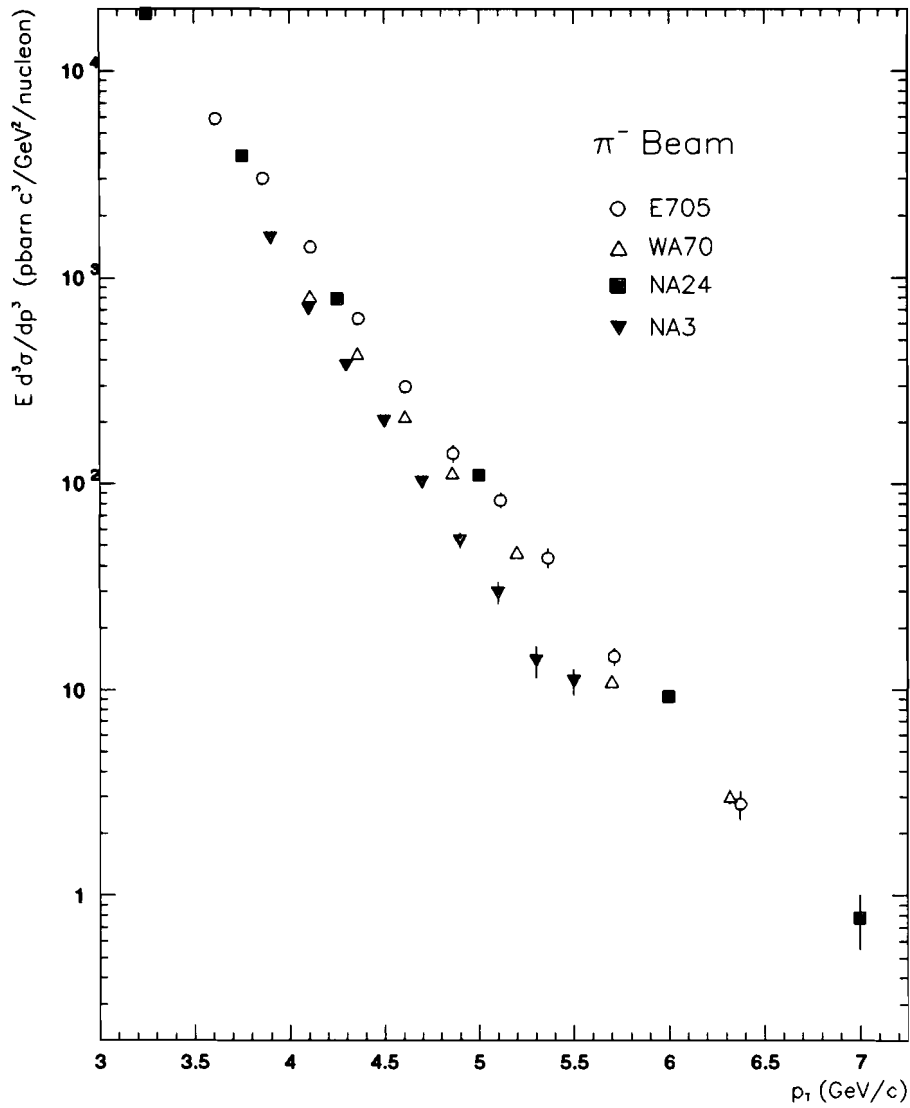


Figure 9.11: Invariant cross section  $\sigma(\pi^- + Li \rightarrow \pi^0 + X)$  as a function of  $p_T$ . Errors are statistical only.

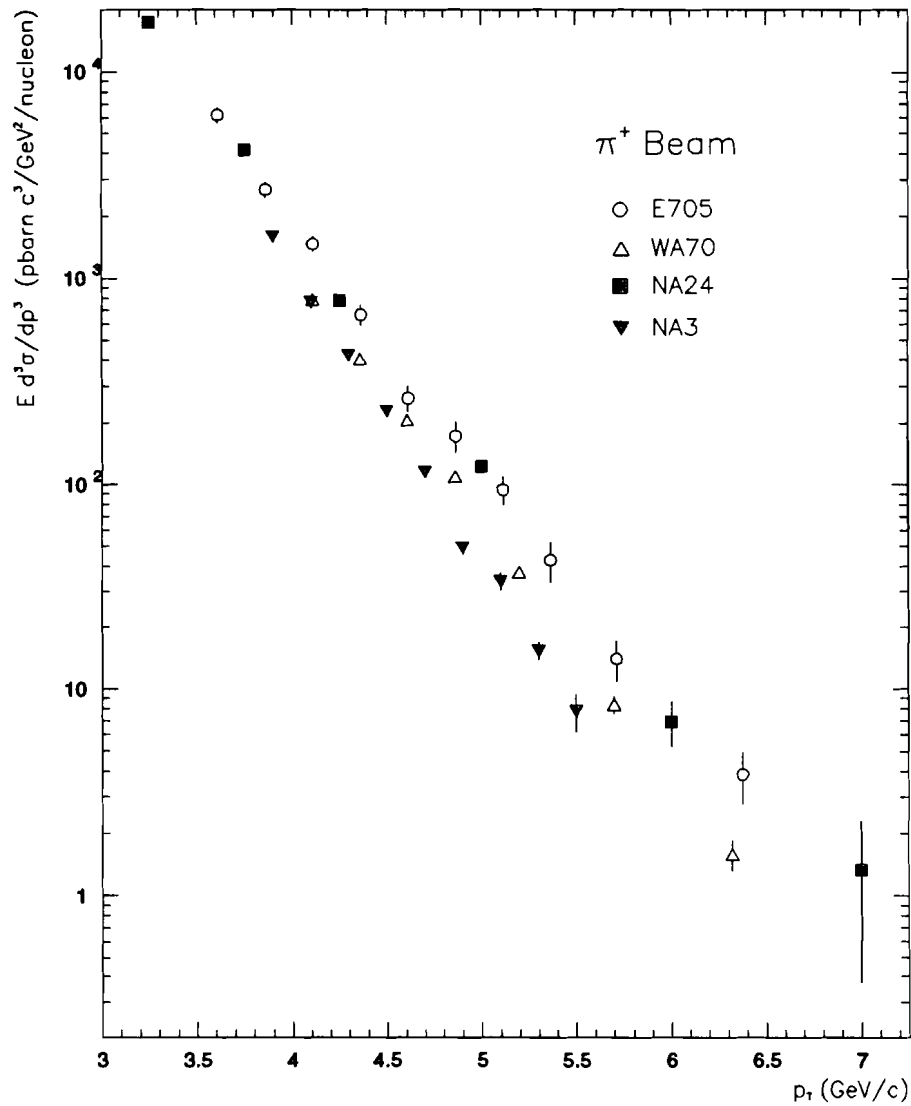


Figure 9.12: Invariant cross section  $\sigma(\pi^+ + Li \rightarrow \pi^0 + X)$  as a function of  $p_T$ . Errors are statistical only.

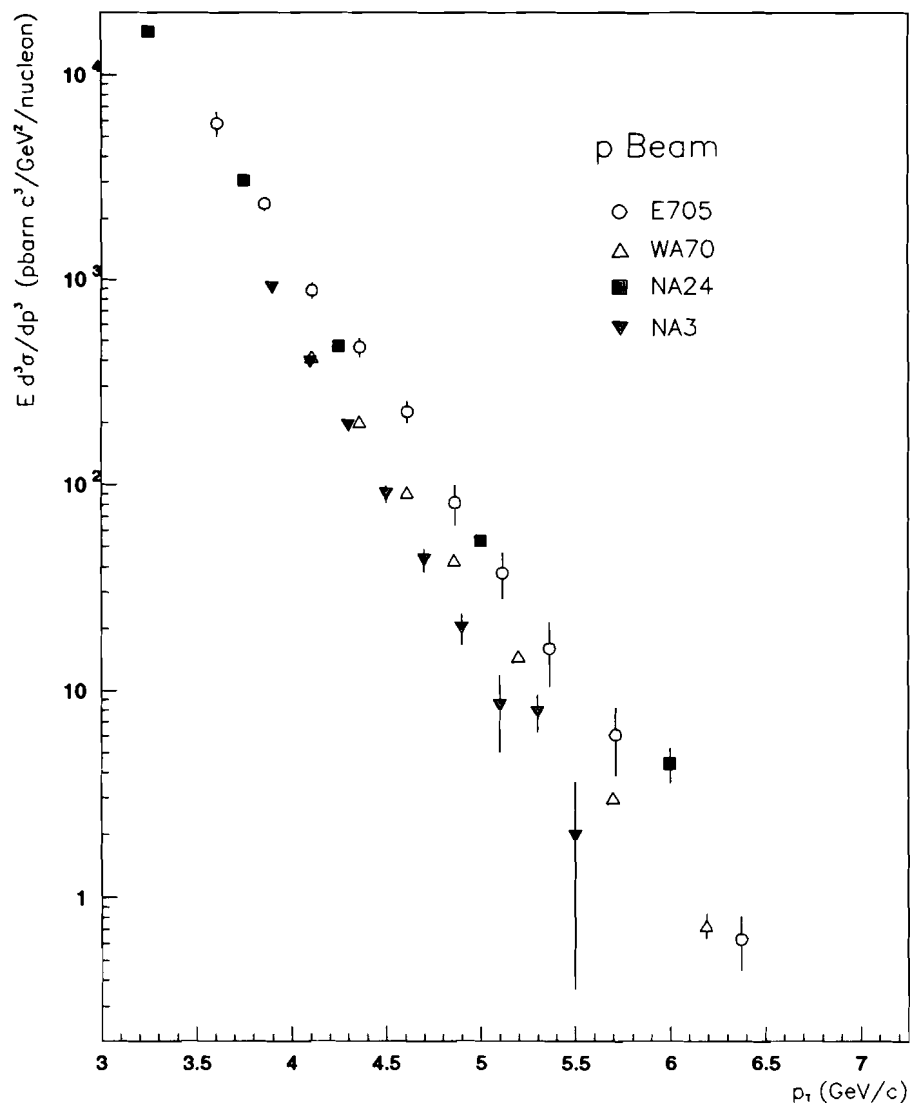


Figure 9.13: Invariant cross section  $\sigma(p+Li \rightarrow \pi^0+X)$  as a function of  $p_T$ . Errors are statistical only.

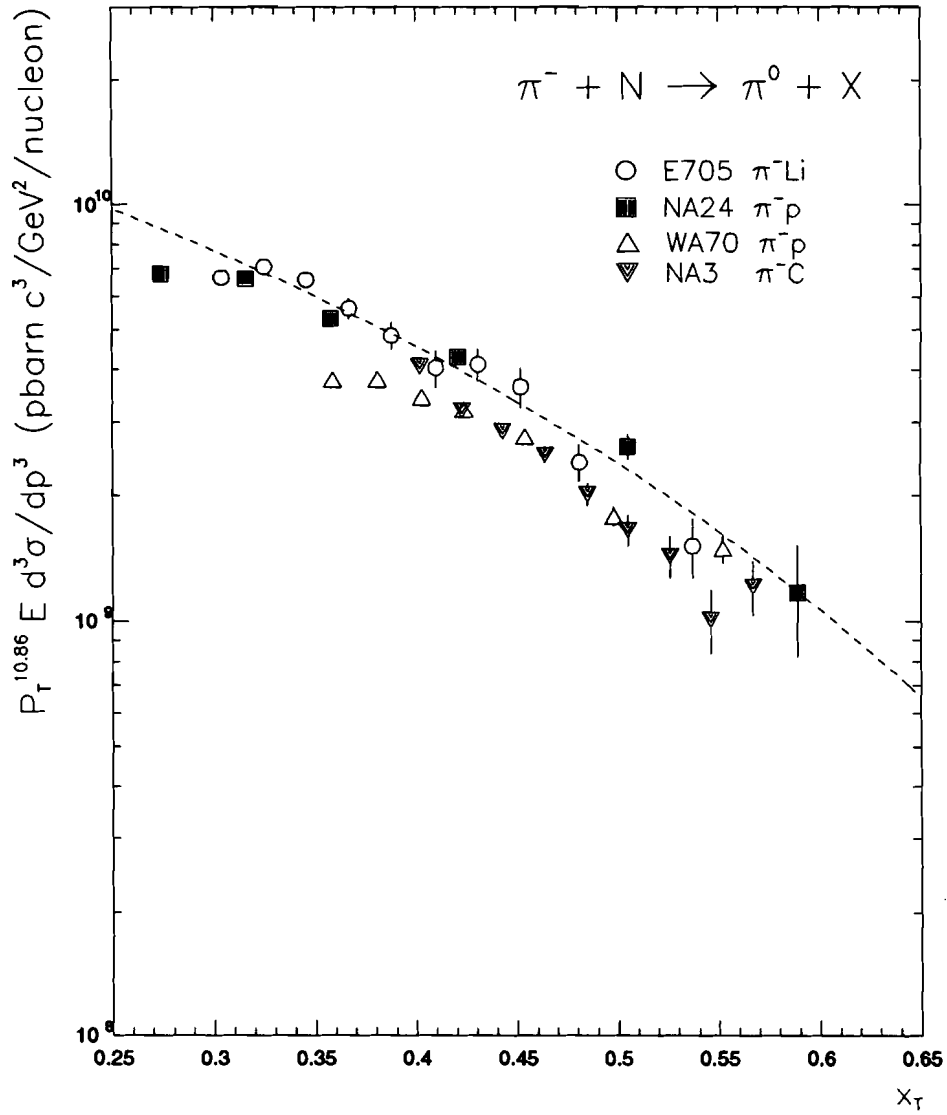


Figure 9.14: Invariant cross section  $\sigma(\pi^- + Li \rightarrow \pi^0 + X)$  as a function of  $x_T$ . Errors are statistical only.

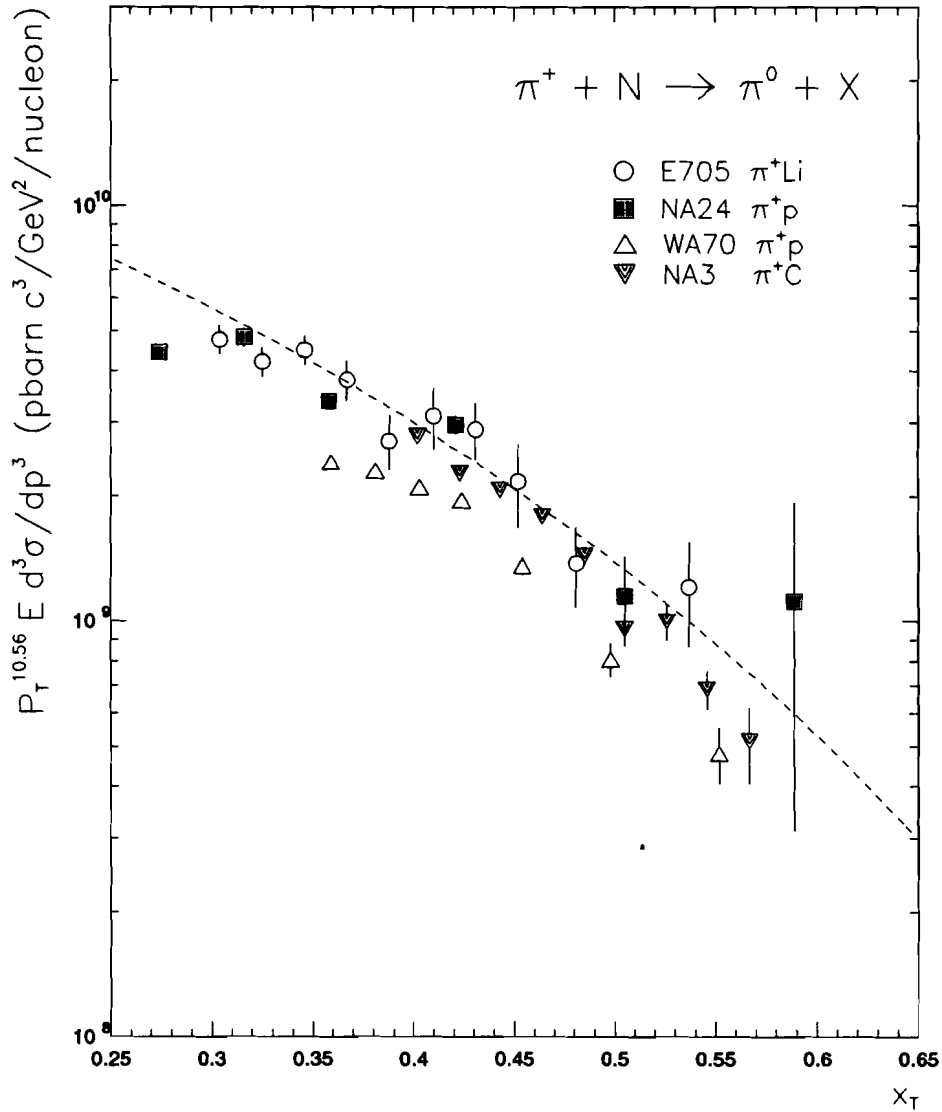


Figure 9.15: Invariant cross section  $\sigma(\pi^+ + Li \rightarrow \pi^0 + X)$  as a function of  $x_T$ . Errors are statistical only.

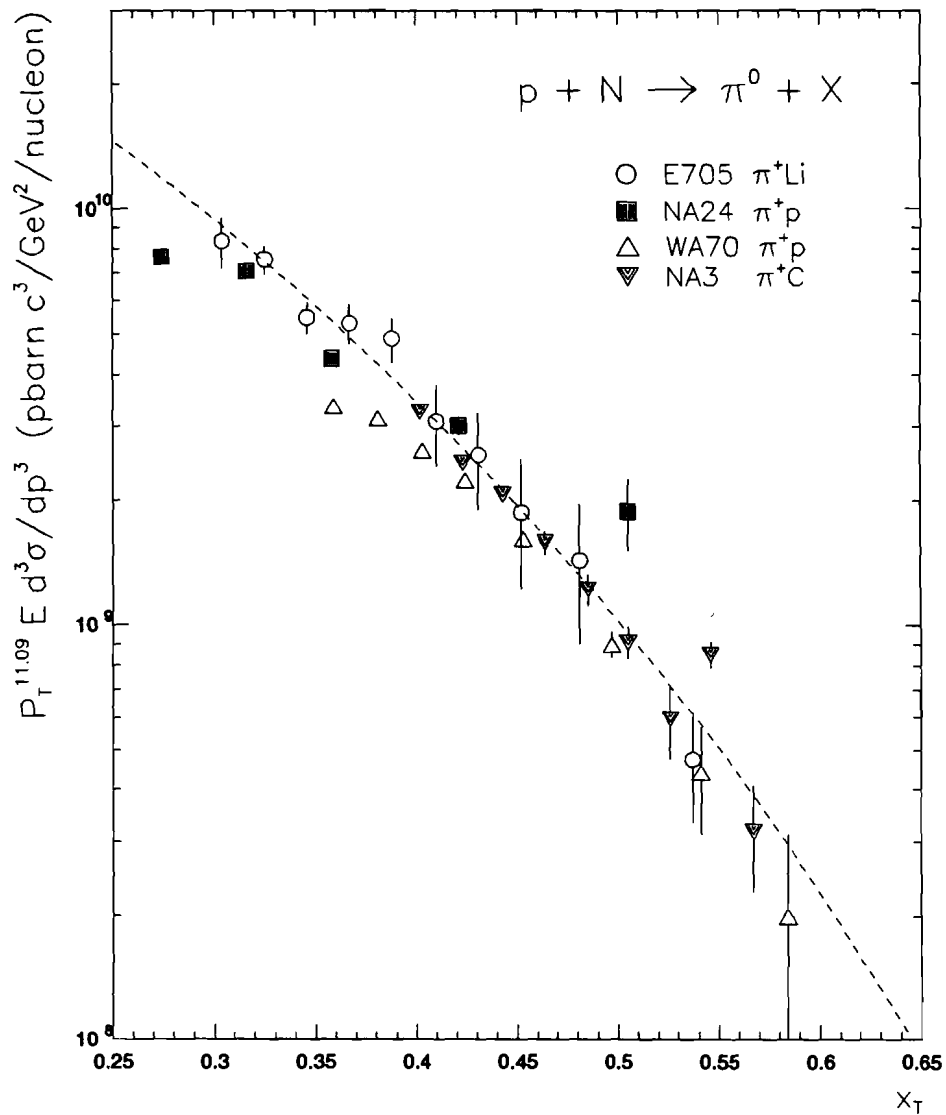


Figure 9.16: Invariant cross section  $\sigma(p+Li \rightarrow \pi^0+X)$  as a function of  $x_T$ . Errors are statistical only.

## 9.5 Conclusions

The invariant cross sections of high  $p_T$   $\pi^0$  and  $\eta$

$$\sigma(\pi^- + Li \rightarrow \pi^0 + X)$$

$$\sigma(\pi^+ + Li \rightarrow \pi^0 + X)$$

$$\sigma(p + Li \rightarrow \pi^0 + X)$$

$$\sigma(\pi^- + Li \rightarrow \eta + X)$$

$$\sigma(\pi^+ + Li \rightarrow \eta + X)$$

$$\sigma(p + Li \rightarrow \eta + X)$$

are measured, and they agree with measurements by other experiments. The ratio of

$$\frac{\sigma(\pi^+ + Li \rightarrow \pi^0 + X)}{\sigma(\pi^- + Li \rightarrow \pi^0 + X)}$$

is independent of  $p_T$  within error, and is equal to one. This result agrees with the theoretical prediction of isospin invariance. The ratio of

$$\frac{\sigma(\pi^+ + Li \rightarrow \pi^0 + X)}{\sigma(p + Li \rightarrow \pi^0 + X)}$$

increases with  $p_T$ , in agreement with the parton model. The measured cross section ratio of  $\eta$  and  $\pi^0$  is  $0.471 \pm 0.031$  for  $\pi^-$  beam,  $0.457 \pm 0.057$  for  $\pi^+$  beam and  $0.562 \pm 0.074$  for proton beam, close to the expected value of 0.5, and in general agreement with other experiments of similar  $\sqrt{s}$ . Those ratios are independent of  $p_T$  in the range of our study.

# References

- [1] Gell-Mann, M., "A Schematic Model of Baryons and Mesons",  
Phys. Lett. 8 (1964) 214.
- [2] Perkins, D., "Introduction to High Energy Physics", Addison-  
Wesley, New York, 1982.
- [3] Halzen, F., and A.D. Martin, "Quarks & Leptons: An Introduc-  
tory Course in Modern Particle Physics", John Wiley & Sons,  
1984.
- [4] Han, M.Y., and Y. Nambu, Phys. Rev. B139 (1965) 1006
- [5] Breidenbach, M., et al., Phys. Rev. Lett. 23, (1969) 935.
- [6] Panofsky, W.K.H., "Proceedings of 14th International Confer-  
ence on High Energy Physics", Vienna, 1969.
- [7] Feynman, R.P., "Photon-Hadron Interactions", Benjamin, Inc.,  
1972.
- [8] Bjorken, J.D., Phys. Rev. 163 (1967) 1767.

- [9] Freidman, J.T., *Ann. Rev. Nucl. Science* 22 (1972) 203.
- [10] Duke, D.W., and J.F. Owens, *Phys. Rev. D* 30 (1984) 49
- [11] Ferbel, T. and W.R. Molzon, *Rev. Mod. Phys.* 56 (1984) 181.
- [12] Owens, J.F., *Rev. Mod. Phys.* 59 (1987) 465.
- [13] Halzen, F., and D.M. Scott, *Phys. Rev. D* 18 (1978) 3378.
- [14] Darriulat, P., et al., *Nucl. Phys. B* 110 (1976) 365.
- [15] Alper, B. et al., *Phys. Lett. B* 44 (1973) 521.
- [16] Banner, M., et al., *Phys. Lett. B* 44 (1973) 537.
- [17] Büsser, F.W., et al. *Phys. Lett. B* 46 (1973) 471.
- [18] Culter, R., and D. Silver, *Phys. Rev. D* 17 (1978) 196.
- [19] Ellis, S.D., and M.B. Kislinger, *Phys. Rev. D* 9 (1974) 2027.
- [20] Geist, W.M., et al., *Phys. Rep.* 197 (1990) 263.
- [21] Badier, J., et al., *Z. Phys. C* 30 (1986) 45
- [22] Bonesini, M., et al., *Z. Phys. C* 37 (1987) 39.
- [23] DeMarzo, C., et al., *Phys. Rev. D* 36 (1987) 8.
- [24] Binkley, M., et al. Fermilab proposal 705, 1981.
- [25] Conetti, S., et al., *IEEE Trans. Nucl. Science* 36 (1989) 112.

- [26] Cox, B., et al., Nucl. Instr. & Meth. 219 (1984) 487; A238 (1985) 321; Wagoner, D.E., et al., A238 (1985) 315.
- [27] Jenkins, C.M., et al., IEEE Trans. Nucl. Science 36 (1989) 117.
- [28] Spiegel, L., et al., IEEE Trans. Nucl. Science 36 (1989) 86.
- [29] Turkington, T.G., "Precise Measurement of Photons from the Interactions of 300 GeV/c Hadrons on a Lithium Target", Ph.D. Dissertation, Duke University, 1989.
- [30] Delchamps, S.W., et al., IEEE Trans. Nucl. Science 36 (1989) 680.
- [31] Zioulas, G., et al., IEEE Trans. Nucl. Science 36 (1989) 375.
- [32] Fortney, L.R., "Principles of Electronics: Analog and Digital", Harcourt Brace Jovanovich, New York, 1987.
- [33] Fortney, L.R., private communication, 1990.
- [34] Zioulas, G., "Pizero and Direct Photon Production at High Transverse Momenta", Ph.D. Dissertation, McGill University, 1991.
- [35] Bonesini, M., et al., Z. Phys. C38 (1988) 371.
- [36] Bonesini, M., et al., Z. Phys. C42 (1989) 527.
- [37] Antille, J., et al., Phys. Lett. 194 (1987) 568.

- [38] Donalson, G.J., et al., Phys. Rev. Lett. 40 (1978) 684.
- [39] DeMarzo, C., et al., Phys. Rev. D36 (1987) 16.
- [40] Carroll, A.S., et al., Phys. Lett. B80 (1979) 319.
- [41] Poslis, J., et al., Phys. Rev. Lett. 51 (1983) 967.
- [42] Field, R.D., and R.P. Feynman, Phys. Rev. D15 (1977) 2590.

# Biography

Qifeng Shen was born in Luxiang, Suzhou, China, on Oct. 20, 1962.

He received a B.S. degree in physics from Shandong University in July, 1982.

He was in his third year of graduate school at Shandong University when he went to Fermilab on an exchange program in Oct., 1984. He worked at Fermilab until he entered the graduate school at Duke University in Aug., 1986.

He was a teaching assistant and a research assistant during 1986–1988, and has been a research assistant ever since.